Master Thesis in Physical Oceanography

Upper-ocean hydrography in the Eurasian Basin and its implication on sound speed

Astrid Stallemo

August 2022

Geophysical Institute
Faculty of Mathematics and Natural Sciences
University of Bergen

Abstract

The Polar Surface Water (PSW) and the Atlantic Water (AW) characteristics and their vertical extent are investigated using data from three moorings deployed in the Nansen Basin, north of Svalbard, under the Coordinated Arctic Acoustic Thermometry Experiment (CAATEX) between September 2019 and July 2020. The data set from the CAATEX moorings provide an updated picture of the hydrography and circulation in the Nansen Basin, north of Svalbard. The main finding at the southernmost mooring, A-N2, was increased temperatures (1.75 °C) and current speeds (> 10 cm s^{-1}) at 50 m at the beginning of March 2020. Further north, at the C-N1 mooring, the temperature profiles between 50 m and 1000 m were quite stable throughout the year, especially between 50 m and 91 m. The calculated mean temperature of the AWL along the CAATEX section in the Eurasian Basin is well represented by the Ocean-Reanalysis Multi-Model-Mean and provides confidence in using the reanalysis to evaluate climate models in the region. The effect of salinity on sound speed was found to be small, but the vertical and horizontal distribution of salinity between regions has to be accounted for if the salinity range is large.

Acknowledgements

First of all, I would like to thank my supervisor Eva Falck for all the time and effort that has been put into improving the structure and writing of this thesis. Thank you for all the valuable input about the hydrography in the Arctic Ocean. I am also very grateful for the opportunity to stay in Svalbard this winter and that you have taken time during the summer vacation to finalize this thesis. A special thanks to my supervisor Hanne Sagen for including me in the work done by the Acoustic and Oceanography group at NERSC and for the possibility of working with the exciting data set from the CAATEX project. I am also very grateful for all the support you have given me during this year. Your engagement and positivity have really made this work fun. Last but not least, thank you for including me on the UAK summer school cruises to Svalbard, the Smart Ocean cruise to fjords around Bergen, and to the One Ocean Expedition between Miami and New York. I have learned incredibly much that I take with me further. I would also like to thank Helene and Espen for always finding the time to help me with everything from data sets to presentations. Also, thanks to Espen for all the knowledge you have shared on the cruises and for making room to try and fail. And to keep special attention when noting down coordinates.

Last but not least, a big thanks to my family and friends. I am so grateful for all the support and good words you have given me throughout the years as a student, especially during this summer.

This master thesis is based on data made available through the Coordinated Arctic Acoustic Thermometry Experiment funded by the Research Council of Norway (Project number 280531) and Office of Naval Research (Grant Number N00014-18-S-B001). The CAATEX project is coordinated by Hanne Sagen, Nansen Environmental and Remote Sensing Center (NERSC), and Matthew Dzieciuch, Scripps Institution of Oceanography (SIO). Oceanographic and sea ice data from the moorings are made available by NERSC, SIO, John Colosi, Naval Post Graduate School, and by Richard Krishfield at the Woods Hole Oceanographic Institution.

Astrid Stallemo
Bergen, 15 August 2022

Contents

1 Introduction

The Arctic has experienced large changes in the atmosphere, sea ice, and ocean over the past decades. The temperature in the Arctic has increased twice as much as the global average over the past 50 years, a phenomenon called the Arctic Amplification (AMAP 2017). This amplification is driven by complex intertwined processes by remote forcings and local positive feedbacks (Screen et al. 2012). Examples of remote forcings are increasing concentrations of greenhouse gases, poleward oceanic and atmospheric heat transport (Bintanja et al. 2011; Stroeve & Notz 2018). This additional heat entering the Arctic is driving widespread changes in this sensitive climate.

The observational record from satellite remote sensing has shown a substantial decline in the sea ice extent since 1979 (Figure 1) and has become one of the most iconic indicators of climate change (Polyakov et al. 2018; Stroeve et al. 2008). The three lowest records in the sea ice extent occurred in the previous decade (2007, 2012, and 2020) showing that this environment continues to rapidly change (Wang et al. 2022; Perovich et al. 2021). The sea ice is very sensitive to the surface air temperature (Zhang et al. 2008). In addition to the declining sea ice extent, the multiyear sea ice has rapidly been replaced by thinner first-year ice in recent years (Wang et al. 2022). This has resulted in an ice cover more sensitive to atmospheric and oceanic forcings, through a more mobile and weaker ice cover, and a strong seasonal cycle in the sea ice extent (Figure 1). The seasonal cycle in the sea ice extent shows a maximum extent in March and a minimum extent in September. When sea ice melts, more of the solar radiation is absorbed by the darker ocean surface, resulting in a positive feedback of further heating.

However, the extensive sea ice cover limits access to the Arctic Ocean throughout much of the year. Oceanographic data in high latitudes are therefore sparse in both space and time. To observe the ocean in ice-covered regions, in situ measurements using shipborne instruments, ice-based observatories including various ice buoys carrying different sensors, seafloor installations, or bottom anchored moorings are needed. There are still a very limited number of ocean observations from the deep basins of the Arctic Ocean, particularly in the Eurasian Basin. Drifting ice observatories are very important but changes in the hydrographic profiles are influenced by time and geographical position. Moorings, however, can provide more information about changes over time at fixed positions.

The role of oceanic heat transported from lower latitudes into the Arctic Ocean was already found by Nansen in the 1890s (Polyakov et al. 2020). He observed warm (temperature > 0 °C) and salty water of Atlantic origin (Atlantic Water, AW) distributed at intermediate depth ($\sim$ 150-900 m) in the Eurasian Basin (Polyakov et al. 2020). Above this, the Halocline Layer separates the Atlantic Water Layer from the Polar Mixed Layer and sea ice. Over the last decades, several studies have shown that the climate change signal is also visi-

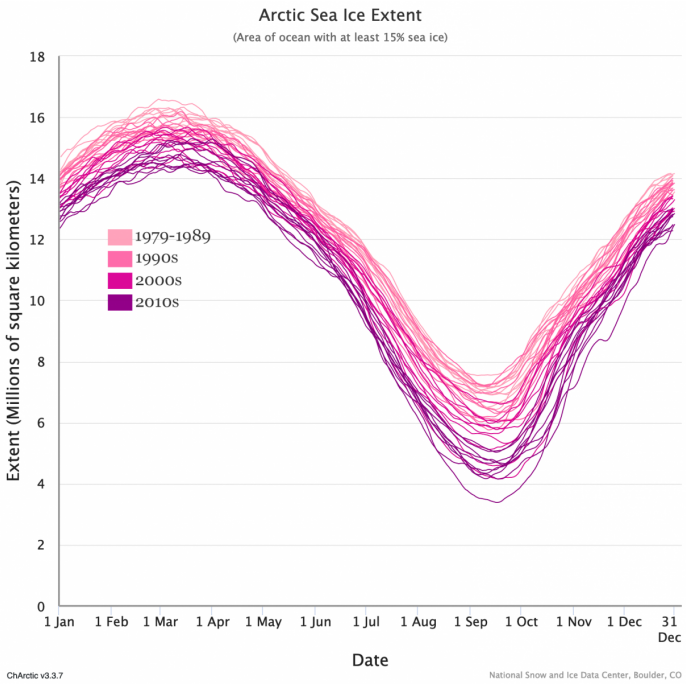

Figure 1: Each year, Arctic sea ice follows the same general trajectory: growth from late September through March or April, and melt from April through mid-September. Although the shape of the yearly trajectory has not changed, recent years have experienced lower extents in all seasons, especially summer and early autumn. The figure is taken from the National Snow and Ice Data Center.

ble in the ocean (e.g. Morison et al. 1998; Karcher et al. 2003; Polyakov et al. 2012, 2017; Hordoir et al. 2022). The increased oceanic heat transported northward of the AW have driven several changes in the Arctic Ocean, a transition called Atlantification. Associated with Atlantification, is the weakening stratification and shoaling of the AW, leading to enhanced upward heat flux, which contributes to ice melt and will further enhance the Arctic Amplification (Polyakov et al. 2010; Hordoir et al. 2022).

Under the Coordinated Arctic Acoustic Thermometry Experiment (CAATEX), six oceanographic and acoustic moorings were operated between July 2019 and August 2020. Three moorings were positioned in the Canadian Basin and three were positioned in the Nansen Basin. The oceanographic point measurements from the moorings are complemented with mean ocean temperature measurements through acoustic thermometry along the CAATEX section (red dotted line in Figure 2). The concept of thermometry is to transmit low frequency sound from a source on one mooring to another mooring equipped with a receiver array several hundreds of kilometers away. The time it takes for the sound to travel is measured with high accuracy and the distance between the source and the receiver array is known. Then by the use of acoustic inversion methods the mean ocean temperature is obtained. In 1994 and 1999 trans-arctic acoustic measurements of the mean ocean temperature were made, and the CAATEX project were designed to repeat this experiment. Due to the complex acoustic analysis, the acoustic thermometry is outside the scope of this thesis. However, knowledge about the vertical structure of the water column affects the propagation of the sound, and studying this is essential to understand and interpret the

experimental observations of acoustic thermometry.

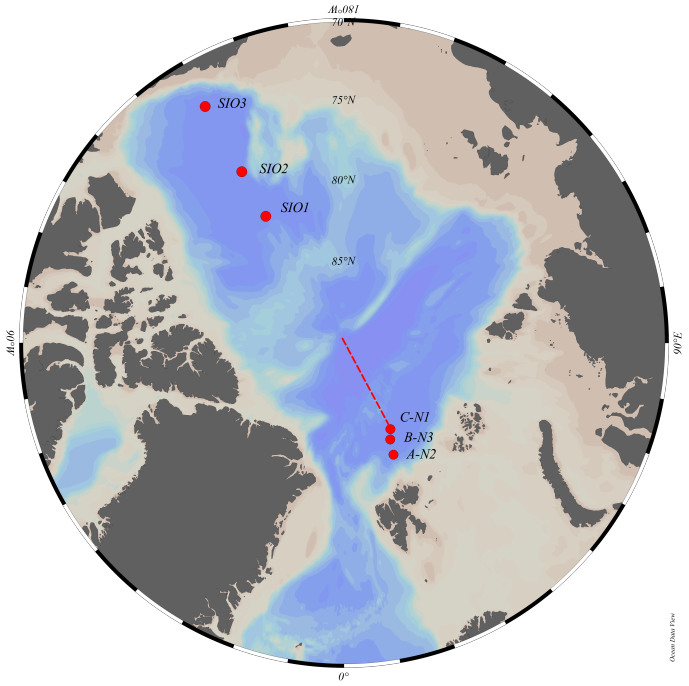

Figure 2: The positions of the moorings operated under the CAATEX project. The A-N2, B-N3, and C-N1 moorings are positioned in the Nansen Basin. Whereas the SIO1, SIO2, and SIO3 moorings are positioned in the Canadian Basin. The red dotted line displays the section in the Eurasian Basin where the acoustic sound signals are sent from the C-N1 mooring towards the SIO1 mooring (hereinafter referred to as the CAATEX section in the Eurasian Basin).

The purpose of this study is to examine the vertical structure of the Polar Mixed Layer (PML) and the Halocline Layer (HL), collectively called the Polar Surface Layer (PSL), and the Atlantic Water Layer (AWL), and their variations at the three CAATEX moorings in the Nansen Basin, north of Svalbard, between September 2019 and July 2020. The oceanographic point measurements of temperature, salinity, and pressure, including current profiles and ice draft measurements from these moorings will be used (Figure 2).

In addition, observations of temperature and salinity from some selected cruises between 1995 and 2021 have been used to calculate the mean temperature of the AWL as near the CAATEX section in the Nansen and Amundsen Basins as possible (red dotted line in Figure 2). These observations will be used to establish a timeline of the mean temperatures of the Atlantic Water Layer (AWL). This timeline of observational mean temperatures of the AWL is currently being used to evaluate the mean AWL temperatures from the Ocean Reanalysis Multi-Model-Mean (Langehaug et al. in progress). The Ocean Reanalysis data is a Multi-Model Mean of 6 different reanalyses, providing monthly gridded data for the period 1993-2010, and provides five different depth layers. The individual Ocean Reanalyses are described in detail in Uotila et al. (2019) and will not be further discussed here. However, a main conclusion from the former study is that the Ocean Reanalysis Multi-Model-Mean is a useful product and the observations analyzed in this thesis could help build further confidence in using the Ocean Reanalysis to evaluate climate models in the

Eurasian Basin. The climate models are presently being used to understand, predict, and project climate changes on a range of time scales. But, there are large biases in these models, particularly for the Arctic Ocean. Thus, assessing climate models against observations and reanalyses is essential to improve the models and understand their predictive capacity. The main focus in this thesis will be on the observational mean AWL temperatures, and a comparison between the observed and the Ocean Reanalysis Multi-Model-Mean mean temperatures of the AWL will briefly be presented.

Moreover, ocean stratification and variability influence how sound propagates in the ocean. The speed of sound is a function of temperature, salinity, and pressure. Spatial and temporal variations of these parameters will change the speed of sound accordingly. Compared to the effect of temperature, the temporal and spatial variations in salinity have a very small effect on the sound speed and can most often be neglected (Dushaw et al. 2016). In the absence of salinity measurements, a commonly used salinity constant of 35 is used to compute the sound speed. However, since the vertical and horizontal distribution of salinity varies between regions, the effect of using the constant salinity of 35 versus observed salinity profiles from the Eurasian Basin will be addressed in this thesis.

2 Background

The oceanic areas north of the Greenland-Scotland Ridge on the Atlantic side and the Bering Strait on the Pacific side are referred to as the Arctic Mediterranean (Figure 3). The Arctic Mediterranean consists of the Nordic Sea (Norwegian, Iceland, and Greenland Seas) and the Arctic Ocean. The Arctic Ocean is a semi-enclosed ocean with an approximately area of 9.4 x 10^6 km^2 (Rudels et al. 2015). About half of this area is occupied by the broad shallow continental shelf seas: the Barents, Kara, Laptev, East Siberian, Chukchi, and Beaufort Seas (Figure 3). The deep central Arctic Ocean can be separated into two major deep basins. The Eurasian Basin on the Atlantic side of the Lomonosov Ridge, which again can be subdivided into the Amundsen Basin and the Nansen Basin by the less prominent Nansen-Gakkel Ridge, and the Canadian Basin on the Pacific side of the Lomonosov Ridge, which can be subdivided by the Alpha-Mendeleev Ridge into the Canada Basin and the Makarov Basin (Figure 3).

The Arctic Ocean Circulation

The surface circulation is strongly impacted by winds. The predominant atmospheric circulation causes the average sea level pressure to be high over the Canadian Basin and low over the Eurasian Basin, the Barents Sea, and the Nordic Seas. The resulting winds draw relatively fresh water over the Canadian Basin and set up the anticyclonic (clockwise) Beaufort Gyre (Figure 3) and a weaker cyclonic (counterclockwise) gyre in the Eurasian Basin. The anticyclonic Beaufort Gyre in the Canadian Basin causes the surface waters and sea ice to converge in the center, resulting in the largest freshwater reservoir (45 000 km^3) in the Arctic Ocean (Aagaard & Carmack 1989). The two circulation cells converge north of Siberia to form the Transpolar Drift (Figure 3). The Transpolar Drift transports sea ice and river-influenced surface waters across the Central Arctic Ocean from the Siberian region towards the Fram Strait. The position of the Transpolar Drift determines the distribution of the Pacific Water between the Canadian and Eurasian Basin, and the amount of Pacific Water exiting through the Canadian Arctic Archipelago and the Fram Strait (Falck et al. 2005).

On the Atlantic side, the main passages are through the Fram Strait and the Barents Sea Opening. The AW originates from the North Atlantic Current, enters the Nordic Seas over the Greenland-Scotland Ridge (Figure 3). The AW is then transported northward in the Norwegian Sea by the Norwegian Atlantic Current. Upon approaching the Barents Sea Opening (depth $\sim$ 200 m), north of Norway, the Norwegian Atlantic Current bifurcates (Figure 3). About one third of the Norwegian Atlantic Current continues east into the Barents Sea as the Barents Sea Branch (BSB) (Polyakov et al. 2005). While the larger portion continues northward towards the Fram Strait as the West Spitsbergen Current. The fate of the ocean heat transported by West Spitsbergen Current and the BSB are substantially different (Smedsrud et al. 2013). The AW entering the Barents Sea Opening has a tem-

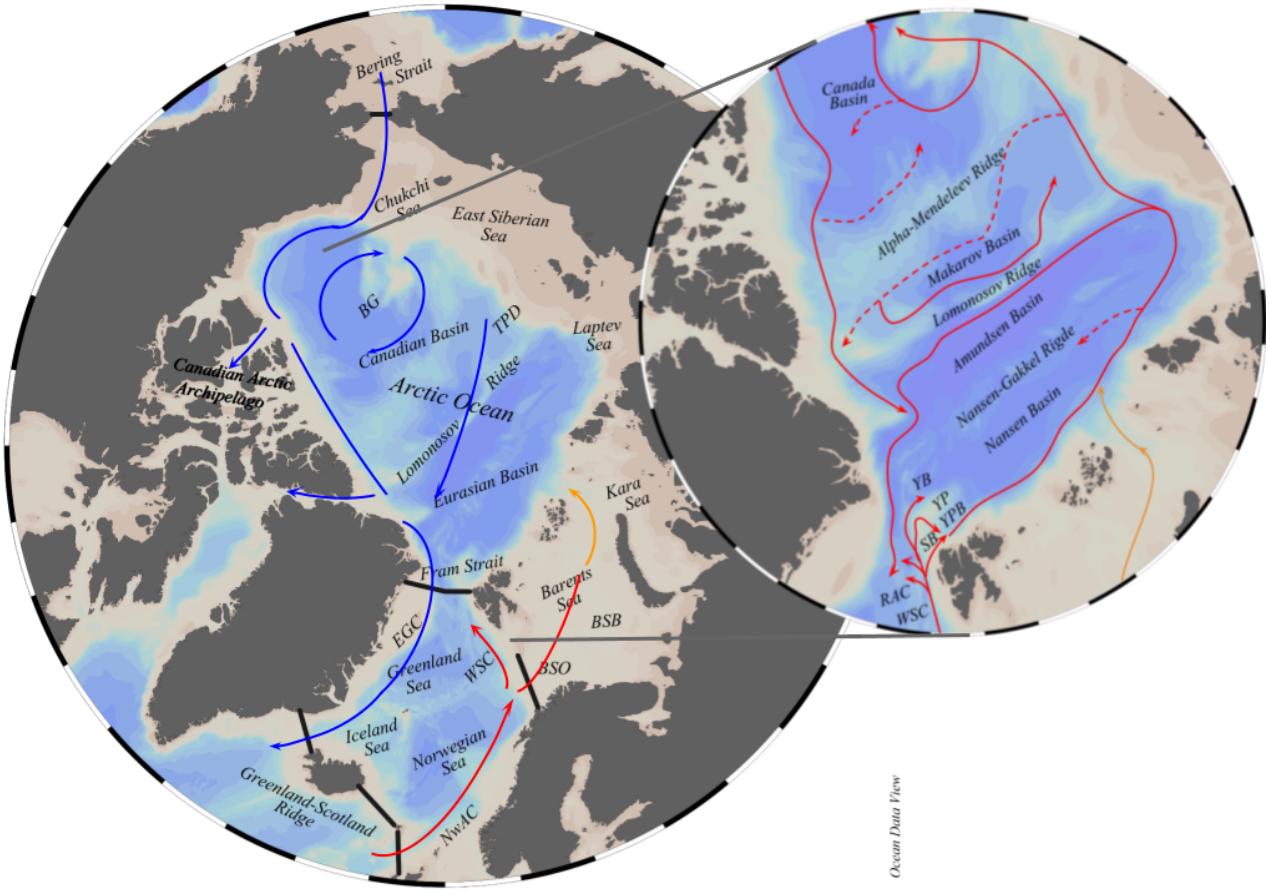

Figure 3: Map of the Arctic Mediterranean and the deep basins of the Arctic Ocean. Blue arrows show the main surface circulation with the Beaufort Gyre (BG), Transpolar Drift (TPD), the fresher inflow through the Bering Strait and the outflow through the Canadian Arctic Archipelago and the Fram Strait in the East Greenland Current (EGC). The red and orange arrows show the main circulation of AW in the Norwegian Atlantic Current, the West Spitsbergen Current, the Barents Sea Branch (BSB), the Svalbard Branch (SB), the Yermak Pass Branch (YPB), the Yermak Branch (YB) and the Return Atlantic Current (RAC). The Yermak Plateau and the Barents Sea Opening are abbreviated as YP and BSO, respectively. The black lines indicate the four gateways to the Arctic Ocean. The map is made in Ocean Data View following Nilsen et al. 2021 and Wang et al. 2018.

perature between $4 - 6$ °C with a mean salinity above 35.06 (Rudels et al. 2015; Skagseth 2008). As the BSB travels through the shallow Barents Sea (mean depth of 230 m), the water masses are heavily modified through mixing, atmospheric cooling, net precipitation, and ice freezing and melting. Smedsrud et al. (2010) showed, using the updated volume and heat budgets, that most of the heat carried by the BSB is already lost to the atmosphere in the southern Barents Sea. Hence the Barents Sea is a heat sink rather than a heat source, with the AW in the BSB entering the Eurasian Basin with temperatures close to 0 °C (Smedsrud et al. 2010).

In contrast, the West Spitsbergen Current plays a significant role in the process of Arctic warming (Piechura & Walczowski 2009. The West Spitsbergen Current is the northernmost extension of the Norwegian Atlantic Current. It flows northwestward towards Spitsbergen, where several branches are deflected westward along the way (Figure 3). Upon enter-

ing the Arctic Ocean through the deep (2600 m) Fram Strait, some of the AW recirculates and are transported southward by the East Greenland Current. In the deep Fram Strait, the upper part of the AW becomes transformed into a less saline surface layer by melting sea ice and mixing with fresher surface water of Arctic origin (Rudels et al. 2004). The fresher surface layer prevents further heat loss of the AW core at depth to the atmosphere. Beszczynska-Möller et al. (2012) found the mean temperature of the AW inflow through the Fram Strait to be 3.1 ± 0.1 °C.

The complicated topography of the Fram Strait results in a complex circulation of the AW. Several branches (adding to the Return Atlantic Current) recirculate westward between 78 °N and 81 °N following the topographic fracture zones across the Fram Strait (Piechura & Walczowski 2009). In addition, the shallow Yermak Plateau, an extension of the Spitsbergen continental shelf toward Greenland, guides the branches to either flow over or around the plateau. The West Spitsbergen Current splits here into three main branches, the Svalbard Branch, the Yermack Pass Branch, and the Yermak Branch (Nilsen et al. 2021). The Svalbard Branch is the easternmost branch and flows over the Svalbard slope. The Yermak Pass Branch flows over the Yermak Plateau, and the Yermak Branch continues northwards around the western slope of the Yermak Plateau. The three branches recombine east of the Yermak Plateau and will hereafter be called the Fram Strait Branch (FSB; Polyakov et al. 2012). The FSB continues eastward at intermediate depth along the Eurasian continental slope. Around the St. Anna Through in the northern Kara Sea, the FSB and the BSB meet again. The two branches continue cyclonically along the continental margins and ridges of the Arctic Ocean as the Arctic Circumpolar Boundary Current (Polyakov et al. 2012).

On the Pacific side, fresher waters from the Pacific enter through the shallow (50 m) Bering Strait into the Beaufort Sea (Figure 3). The Pacific Water is found at and near the surface, and its distribution is therefore influenced by changes in atmospheric forcing (Falck et al. 2005). In earlier studies, colder Pacific waters (Pacific Winter Water) have traditionally renewed the Upper Halocline during winter (Aagaard et al. 1981). However, (Woodgate & Peralta-Ferriz 2021) found that the Pacific Winter Water had become fresher in 2017 compared to in 1990. This implied a shoaling of the Pacific Winter Water and limited the renewal of the Upper Halocline. In summer and autumn, the Pacific inflow (Pacific Summer Water) is fresher and warmer, thus the inflows through the Bering Strait provide an important source of fresh water and heat to the Arctic Ocean.

The main passages of outflow from the Arctic Ocean are in the western part of the Fram Strait and the Canadian Arctic Archipelago (Figure 3). The cold and low-salinity Polar Surface Water is transported southwards in the western part of the Fram Strait by the East Greenland Current (Rudels et al. 2004). The East Greenland Current constitutes of several water masses from the Arctic Ocean. In addition to the the Polar Surface Water, the East Greenland Current transports the Return Atlantic Water, the Modified Atlantic Water, the

Upper Polar Deep Water, the Canadian Basin Deep Water, and the Eurasian Basin Deep Water southwards out of the Arctic Ocean (Langehaug & Falck 2012). The western part of the Fram Strait is also the main exit route for sea ice (Wang et al. 2020). Through the shallow (150 to 230 m) and narrow channels in the Canadian Arctic Archipelago, the Polar Surface Water and Pacific origin waters are transported out of the Arctic Ocean (Rudels 2019; Hu & Myers 2014).

The Arctic Ocean Layers

The Arctic Ocean can be divided into three main layers (Figure 4) based on the temperature and salinity characteristics of the water (Rudels et al. 2015; Talley 2011; Coachman & Barnes 1962). The Arctic Ocean is a β-ocean, meaning salinity is more dominant for the density and stratification compared to temperature (Rudels & Carmack 2022). Thus, the general structure is cold, low-salinity surface water above warmer and higher-salinity waters (Coachman & Barnes 1962). The three main layers are as follows; 1) The Polar Surface Layer which is divided into the Polar Mixed Layer (PML) and the Halocline Layer (HL). 2) The intermediate Atlantic Water Layer (AWL) with water temperatures above 0 °C (Polyakov et al. 2020; Rudels et al. 2013). The AWL's upper and lower boundaries are therefore defined by the zero-degree isotherms. 3) The deep and bottom waters in the Canadian and Eurasian Basins (Figure 4). In the following paragraphs only, the PML, the HL, and the AWL in the Eurasian Basin will be presented since this is the area of interest. The focus will be on their characteristics, importance, and how they interact and effect each other.

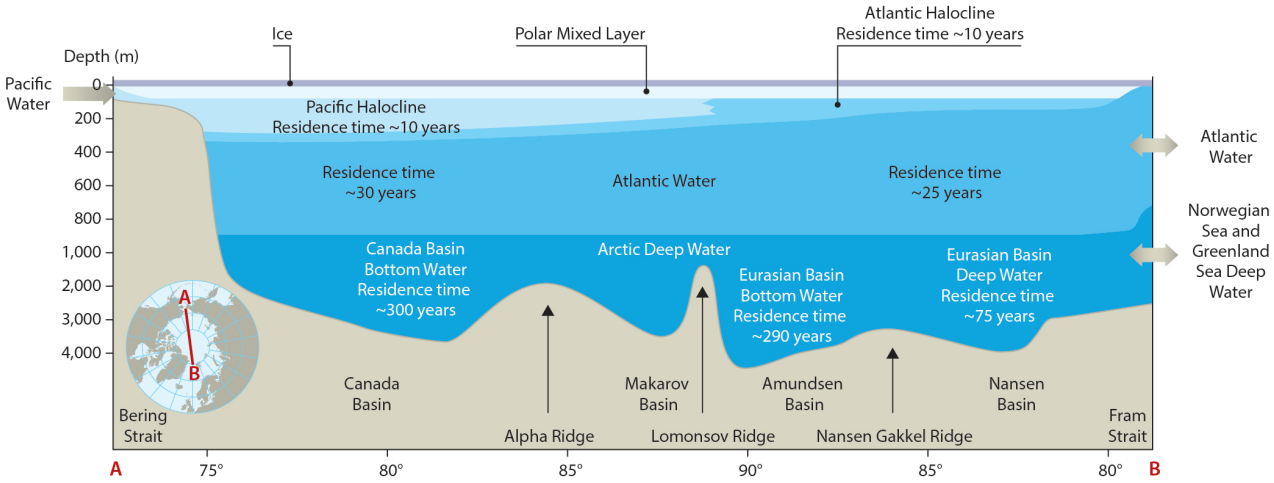

Figure 4: A schematic representation of the three-layer structure of the Arctic Ocean. The arrow on the left shows the Pacific derived water entering through the Bering Strait. The two arrows on the right show the water mass exchange through the Fram Strait. The Polar Mixed Layer (PML) and the Atlantic, and Pacific Halocline Layers (HL), collectively the Polar Surface Layer (PSL). The Atlantic Water and the Deep Water in the different basins. The figure is taken from AMAP (1998).

The Polar Mixed Layer

The PML in the Eurasian Basin is a 20-50 m thick homogeneous layer. The PML lies closest to the surface, thus making it the layer most subject to the ocean-ice-atmosphere interaction. Mixing by wind, density-driven convection, tides, and ice-keels homogenize the PML. The PML experiences some seasonal changes, where its temperature, salinity, and depth vary throughout a year (Peralta-Ferriz & Woodgate 2015; Baumann et al. 2018).

Seasonal cycle

The annual cycle of the PML is strongly connected to the seasonal cycle of the sea ice (Peralta-Ferriz & Woodgate 2015). Following the illustrations in Figure 5, the upper panel shows the evolution of the PML if it was only driven by the thermodynamics of sea ice growth and melt. In this case the PML thins suddenly to $\sim$ zero at the onset of ice melt in spring. In the absence of mixing the PML depth remains equal to the layer of the melt water through summer. In late fall/winter, the PML deepens through density-driven convection due to brine rejection when sea ice forms.

However, in reality mixing through wind stirring acts to deepen the PML. In the two panels in the middle of Figure 5, the effect of wind stirring is illustrated. Starting at the onset melting in late spring, the PML is as thin as the melted ice. As the sea ice melts resulting in more open waters, the wind will mix and deepen the PML during ice free periods (i.e. summer/early autumn). Peralta-Ferriz & Woodgate (2015) emphasized the importance of the underlying stratification regarding the evolving depth of the PML. The underlying stratification determines how effective the wind-induced mixing will be (Brown et al. 2020). Here the evolution during strong and weak underlying stratification are displayed in Figure 5 b.1 and 5 b.2, respectively. The PML depth will be shallower with strong underlying stratification compared to when the stratification is weak, since more energy is needed to break up strong stratification. This will indeed depend on the strength and duration of the wind, as well as ice-free/open water areas since the ice cover prohibits air-ocean interaction. Peralta-Ferriz & Woodgate (2015) found only a significant correlation between the wind and the PML depth under ice-free (ice concentration < 15%) conditions and a less frequent correlation with higher amounts of sea ice.

The underlying stratification will also be important for the evolution of the PML during winter. As stated earlier, the PML deepens during winter due to density-driven convection by brine rejection when sea ice forms. The density of the PML will increase as brine is released and the thickness of the PML will gradually increase through convection. The convection will reach at least down to the depth where the surrounding density is equal to the density of the convective layer, called equilibrium depth. However, one can often find that the convection layer penetrating deeper than the equilibrium depth, thus mixing heavier water upwards and eroding the underlying halocline (Darelius et al. 2021. The

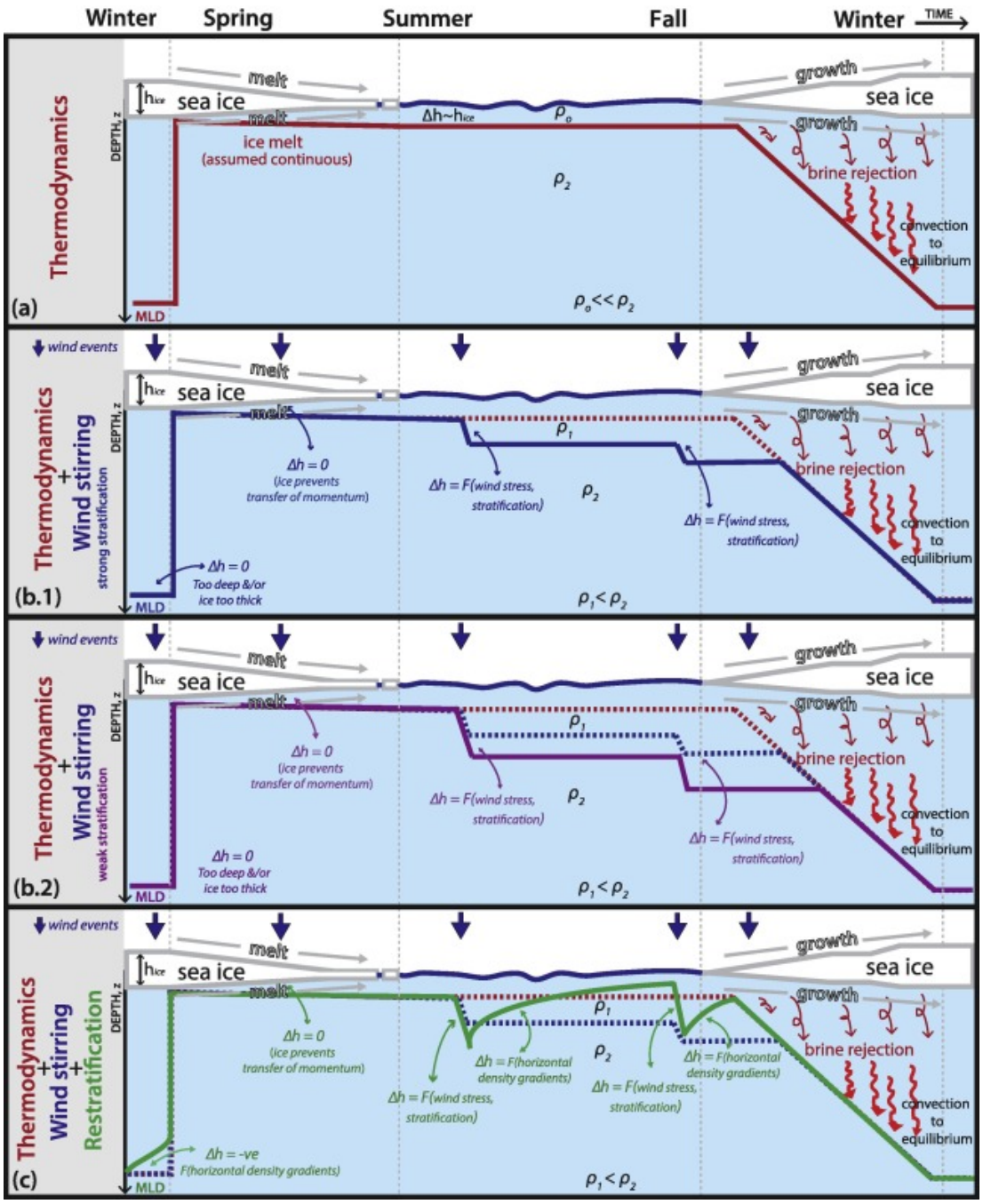

Figure 5: Idealized schematic of the seasonal cycle of the PML in response to (a) thermodynamic forcing (i.e. ice melt and growth) only, (b) combined thermodynamics and wind-driven forcings with relatively strong (b.1) and relatively weak (b.2) underlying stratification; and (c) combined wind-driven and restratification processes.ρ_0, ρ_1, and ρ_2 denote different densities of sea water; D_h denotes change in MLD; H_{ice} is ice thickness; and z is depth. Vertical dashed gray lines separate the seasonal cycle of Arctic sea ice conditions (thick ice in winter, melting ice in spring, ice-free in summer, growing ice in fall). Thick blue arrows represent wind storms. Figure taken from Peralta-Ferriz & Woodgate (2015).

alternation between shoaling of the PML depth due to horizontal density gradients and the deepening effect of wind stress are depicted in Figure 5c.

Recent Changes

In recent decades, a general warming of the upper Arctic Ocean has been widely documented from observations (Carmack et al. 2015; Polyakov et al. 2020; Timmermans & Marshall 2020). The seasonal cycle in the PML makes this layer subject to changes from the atmosphere, sea ice, and the underlying ocean. Polyakov et al. (2020) found, in the eastern (> 70 °E) Eurasian Basin, a warming trend in the PML during the 2010s compared to the 2000s by comparing observations of potential temperature, salinity, and the depth of the PML. This trend was related to the increased summertime solar radiation into the surface ocean that is associated with sea ice loss and decreased albedo (Polyakov et al. 2020; Timmermans & Marshall 2020). Apart from heating found during summertime, there has also been found heating of the PML during winter when there is no solar radiation as well as a higher extent of the protective sea ice cover. In wintertime, Polyakov et al. (2013) found that the PML experienced heating by upward heat transport through winter convection from the underlying layer. These processes of heating the PML are already occurring in the western (< 70 °E) Nansen Basin.

The Halocline Layer

The Arctic Ocean HL is defined as the strong vertical salinity gradient acting as an insulating barrier, separating the sea ice and the cold and fresh PML from the warm and saline AW at depth (Bertosio et al. 2020; Bourgain & Gascard 2011). The HL in the Arctic Ocean can be divided into the Pacific and Atlantic HLs (Figure 4). The Pacific HL is made of fresher Pacific-derived water overlying the denser Atlantic-origin Halocline Waters (hereinafter referred to as Lower Halocline Water, LHW). The Pacific HL is mainly restricted to the Canadian Basin and will not be discussed further.

In the Eurasian Basin, the temperature and salinity of the Lower Halocline Layer (T < 0 °C and S < 34.70) increase with depth until the upper limit of the warm (T > 0 °C) and saline AW (Aksenov et al. 2011). In a TS-diagram, a bend in the LHW can be seen near the salinity of 34.2 and temperatures between − 1.2 °C to − 1.8 °C (Rudels et al. 2004). The bend is known in the literature as the "knee" and is called "knee water". The knee in the TS-diagram indicates that the HL does not form through direct mixing between the PML and the underlying AW (Rudels et al. 2004).

The properties and characteristics of the HL varies between different regions in the Eurasian Basin. The Lower Halocline Layer is formed either by or combined by the advection of cold shelf waters and local winter convection due to ice formation and brine rejection. North of Svalbard in the Nansen Basin, the temperature and salinity are constant with depth (i.e. PML), before the temperature and salinity increase fast down to the AWL. This cause winter convection to reach down to the AWL in most of the western Nansen Basin (Rudels et al. 2004). In summer when a fresher PML is formed through ice melt, the old winter PML

forms a seasonal HL in this area. The "advective mechanism" comes from salinization of shelf waters along the continental shelf sea through brine rejection and is then transported (i.e. advected) from the shelf into the deep basins (Alkire et al. 2017).

Recent changes

There have been several studies on changes of the HL over the past decades (e.g. (Polyakov et al. 2017; 2020; Steele & Boyd 1998). The ocean heat transport have earlier been assumed to play a secondary role for the Arctic surface warming due to the presence of the stable halocline. However, Polyakov et al. (2020) have found a continued weakening of the cold halocline layer (upper part of the halocline with temperatures near the freezing-point) in the eastern Eurasian Basin in the time period between 2015 and 2018. Furthermore, they found a resultant increase in the upward heat flux during winter, showing that the oceanic heat plays a larger role in this area. A weaker or absent halocline layer can result in an increased upward heat flux from the underlying warmer waters (i.e. the AW). Thus making the eastern Eurasian Basin more similar to the upper ocean conditions in the western Nansen Basin (Polyakov et al. 2017).

The Atlantic Layer

The AWL is defined as the layer where the water has a temperature above 0 °C, i.e. between the upper and lower 0 °C isotherms. It is distributed at intermediate depth ($\sim$ 150 - 900 m) in the Eurasian Basin (Polyakov et al. 2020). The vertical temperature profile in the AWL increases down to the core and then decreases down to the deep waters. The AW core is the maximum temperature in the AWL. The corresponding depth of the AW core temperature is called the Atlantic Water core depth. The temperature and depth of the AW core have spatial and temporal variability within the Eurasian Basin. In the Nansen Basin, the AW core temperature is higher ($\sim 2 - 3$ °C) and the AW core depth is found at about 200 m to 300 m. Towards the Nansen-Gakkel Ridge and in the Amundsen Basin, the AW core temperature ($\sim 1 - 2$ °C) decrease and the AW core depth lies deeper between about 300 m and 400 m (Polyakov et al. 2005).

A common feature in the AWL is the presence of inversions in temperature and salinity profiles called interleaving (Rudels et al. 2009). These can be seen as alternating layers of inversions in the temperature and salinity profiles. These structures can be found all over the Arctic Ocean, but are most prominent at frontal zones between different water masses. Since the Arctic Ocean is a low energy environment, such structures can persist over a long time period (Bebieva & Timmermans 2016; Rudels et al. 2015). The weak turbulent activity makes other mixing mechanisms more important (Rudels et al. 2009; Carmack et al. 2015). The difference in molecular diffusion rates of heat and salt drives two processes of double-diffusion, diffusive convection and salt fingers. The coefficient of heat conduction is 100 times larger than the diffusion coefficient of salt which alters the water masses at

the interface between them (Carmack et al. 2015). Rudels et al. (2009) explains the formation area in the Nansen Basin, north of the Kara Sea, where the FSB and the BSB meet and flow parallel in the Arctic Circumpolar Boundary Current. As earlier mentioned, the two branches of AW exhibit different temperature and salinity properties. Thus a strong front between the branches occurs. The interaction between the two branches results in strong inversions, especially in the AW core (Rudels et al. 2009). These structures are then advected with the boundary current and the structures become gradually more organized as they are distributed to the interior basins.

Recent changes

Several papers have shown that the temperature of AWL has increased in recent decades (e.g. Carmack et al. 1995; Polyakov et al. 2004; 2010; 2020; Asbjørnsen et al. 2020). The AW inflow has shown a variable temperature over time, with cooling and warming episodes which complicate the investigation of the long-term variability in the AW (Polyakov et al. 2004). The warming episodes are linked to anomalously warm pulses of AW entering the Nansen Basin in the beginning and end of the 1990s, 2004 and between 2005 and 2007 (Polyakov et al. 2005; 2013; Dmitrenko et al. 2008; Beszczynska-Möller et al. 2012). However, Beszczynska-Möller et al. (2012) reported a warming trend in the inflowing AW through the Fram Strait over the period from 1997 to 2010.

The heat transported with the AW through the Fram Strait keeps the ocean in the western Nansen Basin, north of Svalbard, mainly ice free throughout the year. The halocline here is weaker allowing a vertical ventilation of the AW up to the surface (Athanase et al. 2019; Polyakov et al. 2017; Carmack et al. 2015). The heat entering through the Fram Strait is carried by the Arctic Circumpolar Boundary Current further into the Arctic Ocean (Polyakov et al. 2004) and is driving local changes along its pathway around the Arctic Ocean. For example, the conditions in the eastern Eurasian Basin are in a transition to conditions similar to the western Nansen Basin (Polyakov et al. 2017), where the surface conditions are more influenced by the oceanic heat from the AW, weakening stratification, and declining ice cover. Observations from moorings and Ice Tethered Profilers (ITPs) have shown increased heat and shoaling of the AWL in the eastern Eurasian Basin (Polyakov et al. 2017). This has been shown to play a significant role in the upward heat flux, especially during winter. Making the area more sensitive to winter convection bringing heat upwards. Furthermore, they found the upper boundary of the AWL to be at 85 m during the winter of 2013-2014. This was shallower than the depth of 140 m found during the winter of 2003-2004. This shows that the increased heat entering and extending further into the Arctic Ocean can drive significant changes along its pathway and is termed Atlantification.

The concept of Atlantification is the transition of Arctic waters to a state more similar to the Atlantic waters (Ingvaldsen et al. 2021). Atlantification is driven by a northward transport

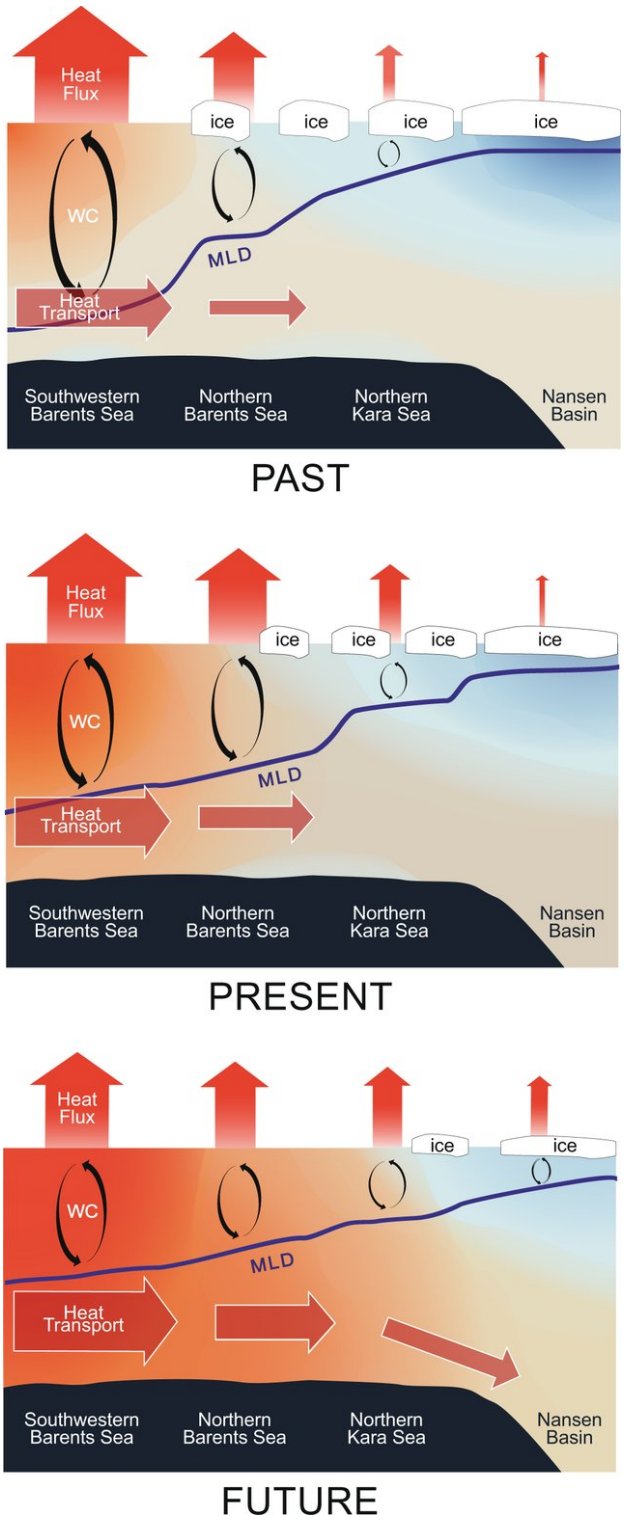

Figure 6: A conceptual schematic of the past, present, and future conditions in the Barents Sea. The related processes to Atlantification with increased oceanic heat transport, increased upward heat flux along the AW pathway, and declining sea ice cover. WC and MLD stand for winter convection and mixed layer depth, respectively. Figure taken from Shu et al. 2021.

of anomalous high temperature and/or transport of AW. The increased heat transported northwards drives several changes in local processes in the Barents Sea (Figure 6) and the Eurasian Basin. The conceptual schematic is an example from the Barents Sea where the

past, present, and future conditions are illustrated. In the southern Barents Sea the atmospheric temperature has increased and less heat is lost from the ocean to the atmosphere. The increased transport of oceanic heat has increased the upward heat flux further north in the northern Barents Sea and the Kara Sea, especially through convection during winter. The latter induces stronger sea ice decline, more intensive ocean surface heat loss, and a deeper mixed layer depth during winter convection.

Acoustic Thermometry

Sound can be used to observe the ocean's temperature structure and its changes, through a technique called acoustic thermometry (Munk et al. 1995). The concept of acoustic thermometry is to transmit low frequency sound from one mooring equipped with a source to another mooring equipped with a receiver array located several hundreds of kilometers away. The distance is large enough so that the sound traveling at different speeds due to the different water masses arrives at different times. The distance between the moorings is known and the travel time of the sound is accurately measured. The mean ocean temperature is obtained by the use of acoustic inversion methods. Mikhalevsky et al. (2001) calculated a sound speed profile based on a temperature and a salinity profile from an ice camp in the eastern Arctic Ocean in 1994 (Figure 7). This is a typical sound speed profile in the Arctic Ocean, with a pronounced acoustic waveguide, also called a channel.

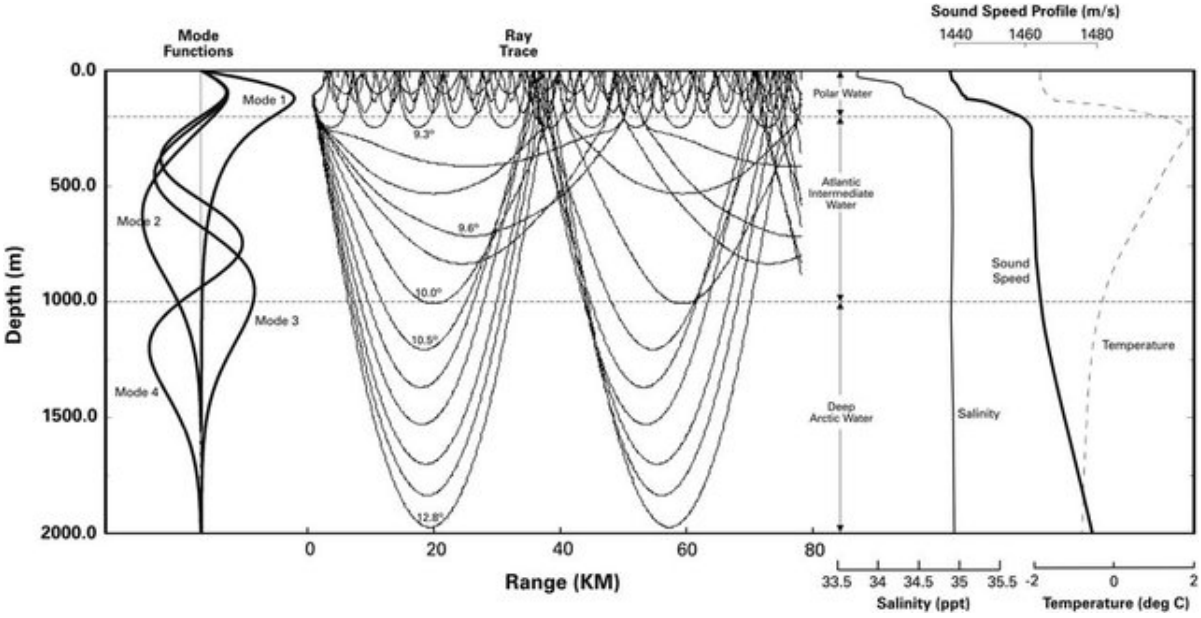

Figure 7: Profiles of measured temperature and salinity, from an ice camp in the eastern Arctic Ocean in April 1994, from which the sound speed profile was calculated. This ray trace is based on the sound speed profile and shows how the sound waves will travel in the different water layers, here divided into the Polar Water, Atlantic Intermediate Water, and the Deep Arctic Water. The mode functions give the main signal of the transmitted sound through different layers. The figure is taken from Gavrilov & Mikhalevsky 2017

They used this sound speed profile to see how the sound would propagate (ray trace) through this vertically stratified ocean. The sound rays are bent toward regions of lower

sound speed, thus will the minimum in the sound speed profile act as a channel. As seen from the sound speed profile in Figure 7, the sound rays will travel in two different channels. One channel is close to the surface underneath the sea ice where the sound speed is about 1440 m s^{-1} near freezing point temperatures. This causes some of the sound energy to be trapped in the channel near the surface, traveling mainly in the Polar Surface Layer, continuously interacting with the sea ice. The rays trapped in the surface channel correspond to mode 1 in Figure 7. A second channel is found at the sound speed minimum at a depth of around 700 m. This is roughly where the pressure becomes dominating parameter for the speed of sound. While the trapped sound near the surface travels at about 1440 m s^{-1}, the sound travels at about 1460 m s^{-1} in the deeper channel, dominated by the AWL. These deeper going rays correspond to mode 2 and mode 3 in the figure. Therefore, will mode 1 arrive later than mode 2 and mode 3, and sound speeds for the two different layers can be calculated.

The ongoing climate change is expected to change the ocean stratification and the mean ocean temperature (heat content). This will influence how sound propagates through the ocean. The CAATEX project is designed to measure these changes by comparing them to measurements made in 1994 and 1997 (Worcester et al. 2020).

3 Data and Method

3.1 Mooring data

Measurements of temperature, salinity, and pressure from different instruments mounted on three moorings in the Eurasian Basin from September 2019 to July 2020 are used. The three moorings NERSC 1, NERSC 2, and NERSC 3 were deployed under the Coordinated Arctic Acoustic Thermometry Experiment (CAATEX). The positions of the moorings are shown in Figure 8 with the exact coordinates given in Table 1. The two columns to the right in Table 1 are the start and end date of the record, respectively. The moorings will hereafter be called A-N2 (NERSC 2), B-N3 (NERSC 3), and C-N1 (NERSC 1), ordered by latitude from south to north (Figure 8).

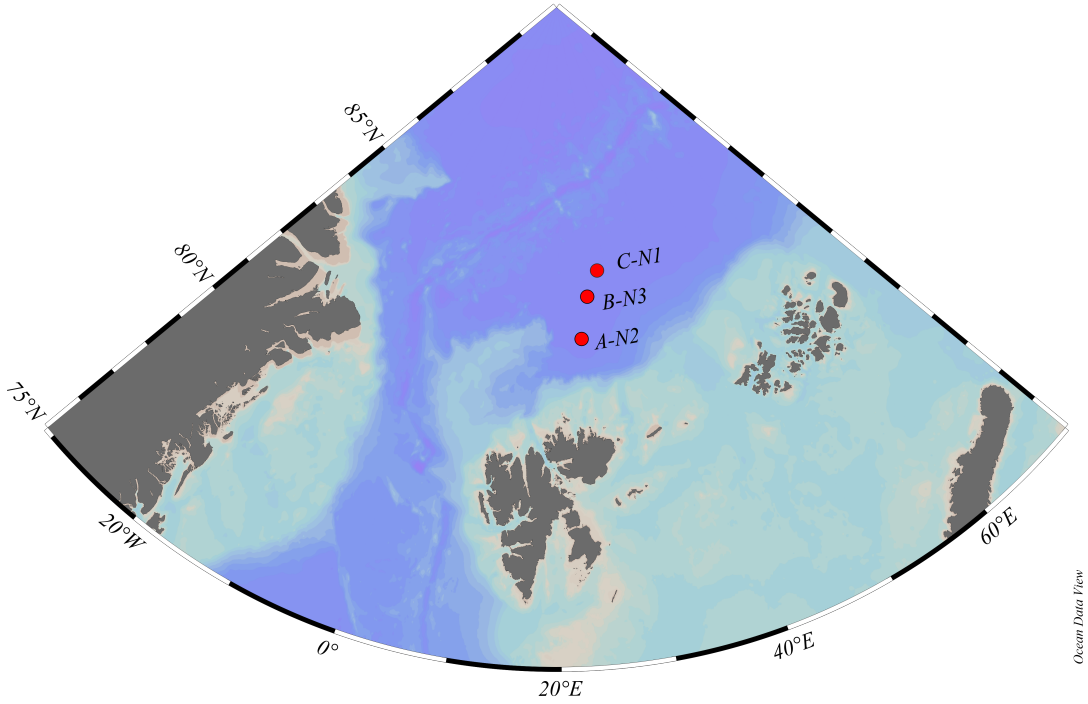

Figure 8: Map of the A-N2, B-N3, and C-N1 mooring positions in the Nansen Basin.

Table 1: The positions of the moorings and the respective start and end date.

Mooring	Latitude [N]	Longitude [E]	Start Date	End Date
A-N2	82.5035	23.9251	03.09.2019	26.07.2020
B-N3	83.4431	25.6639	29.08.2019	30.07.2020
C-N1	84.0025	28.3667	31.08.2019	02.08.2020

Temperature and salinity were measured by Sea-Bird Scientific SBE37-SMP/SM at six depths between 50 m and about 150 m to 171 m. The accuracies of the temperature and salinity measurements from the SBE37-SMP/SM are $\pm$ 0.0002 °C and $\pm$ 0.0003 S m^{-1}, respectively. Temperature was measured every 20 m to 40 m down to about 1000 m by Sea-Bird Scientific SBE56 and SBE39 between about 175 m and 1000 m, with the accuracies of $\pm$ 0.002 °C. Twenty-five hydrophone modules measured temperature every 40 m between about 60 m and 1000 m. The hydrophone modules are designed and made by Scripps Institution of Oceanography. They consist of a hydrophone, battery, memory, clock, and a temperature sensor with the accuracy of $\pm$ 0.005 °C. An overview of the instrumentation on mooring A-N2, B-N3, C-N1 are given in Table 2.

Additionally, there was one Acoustic Doppler current profiler (ADCP) mounted on each mooring at 47 m. The ADCP provided a current speed and magnitude profile above each mooring between about 10 m to 45 m. The current data were processed and made available by Daniel Torres at the Woods Hole Oceanographic Institution. An Upward Looking Sonar (ULS) was mounted on each mooring at 46 m measuring the ice draft. The daily mean ice draft data sets were processed and made available by the Woods Hole Oceanographic Institution. Details on the data processing procedure can be found at `https://www2.whoi.edu/site/beaufortgyre/wp-content/uploads/sites/108/2020/04/BGOS_ULS_Data_Processing_Procedure_85684.pdf`.

Spikes in the time series associated with deployment and recovery were excluded. Data from August 2019 and August 2020 were excluded due to few measurements (less than 2 days with data) when considering monthly mean values. After this, daily, monthly, and 1-month running means of temperature, salinity, and pressure were calculated. The 1-month running means were calculated following Ivanov et al. (2009) with a sliding window of length 31 days. The maps presented here were made in Ocean Data View (Schlitzer, R., Ocean Data View, `https://odv.awi.de`, 2018).

Calculation of sound speed

The sound speed profiles were calculated using the temperature, salinity, and pressure measured by the Sea-Bird Scientific models SBE 37-SMP and SBE 37-SM located on the three moorings between 50 m to about 170 m. Below this depth there were no salinity measurements on the moorings (apart from at 1000 m on the B-N3 mooring). In the absence of salinity measurements at depth, it has commonly been used a constant salinity value of 35. To evaluate this assumed salinity constant, one observational salinity profile, and corresponding temperature profile, from the Ice-Tethered Profile 95 (hereinafter ITP95, downloaded from `https://www2.whoi.edu/site/itp/`) have been used. The position of the profile from ITP95 was at 84.40 °N, 28.49 °E, near the C-N1 mooring. Additionally, to compare the use of a salinity profile versus a constant salinity value, the mean salinity of the ITP95 salinity profile was calculated between 200 m and 750 m. The depth

Table 2: Instrumentation on the A-N2, B-N3, and C-N1 moorings

A-N2			B-N3			C-N1		
Instrument	**Depth**	**Parameters**	**Instrument**	**Depth**	**Parameters**	**Instrument**	**Depth**	**Parameters**
ULS	46	Ice draft	ULS	46	Ice draft	ULS	46	Ice draft
ADCP	47	U,V	ADCP	47	U,V	ADCP	47	U,V
SBE37-SMP	50	T,S,P	SBE37-SMP	50	T,S,P	SBE37-SMP	50	T,S,P
Hydrophone	59	T	Hydrophone	62	T	Hydrophone	83	T
SBE37-SMP	67	T,S,P	SBE37-SMP	70	T,S,P	SBE37-SMP	91	T,S,P
SBE37-SMP	87	T,S,P	SBE37-SMP	90	T,S,P	SBE37-SMP	111	T,S,P
Hydrophone	99	T	Hydrophone	102	T	Hydrophone	122	T
SBE37-SMP	107	T,S,P	SBE37-SMP	110	T,S,P	SBE37-SMP	131	T,S,P
SBE37-SMP	127	T,S,P	SBE37-SMP	130	T,S,P	SBE37-SMP	151	T,S,P
Hydrophone	139	T	Hydrophone	142	T	Hydrophone	163	T
SBE37-SMP	147	T,S,P	SBE37-SM	150	T,S,P	SBE37-SM	171	T,S,P
SBE39-Plus	172	T,P	SBE39-T/P	175	T,P	SBE39-Plus	196	T,P
Hydrophone	179	T	Hydrophone	182	T	Hydrophone	203	T
SBE39-Plus	197	T,P	SBE39-T/P	200	T,P	SBE39-Plus	221	T,P
Hydrophone	219	T	Hydrophone*	222	T	Hydrophone	243	T
SBE39 T/P	222	T,P	SBE39-T/P	225	T,P	SBE39-T/P	246	T,P
SBE39 T/P	247	T,P	SBE39	250	T	SBE39-T/P	271	T,P
Hydrophone	259	T	Hydrophone	262	T	Hydrophone	283	T
SBE39	272	T,P	SBE39	275	T	SBE39-T/P	296	T
SBE39	297	T	SBE39	300	T	SBE39	321	T
Hydrophone	299	T	Hydrophone	302	T	Hydrophone	323	T
Hydrophone	339	T	Hydrophone	342	T	Hydrophone	363	T
SBE39	347	T	SBE39	350	T	SBE39	371	T
Hydrophone	379	T	Hydrophone	382	T	Hydrophone	403	T
SBE39	397	T	SBE39	400	T	SBE39	421	T
Hydrophone	419	T	Hydrophone	422	T	Hydrophone	443	T
SBE39	447	T	SBE56	450	T	SBE56	471	T
Hydrophone	459	T	Hydrophone	462	T	Hydrophone	483	T
SBE56	497	T	SBE56	500	T	SBE56	521	T
Hydrophone	499	T	Hydrophone	502	T	Hydrophone	523	T
Hydrophone	539	T	Hydrophone	542	T	Hydrophone	563	T
Hydrophone	579	T	Hydrophone	582	T	Hydrophone	603	T
SBE56	597	T	SBE56	600	T	SBE56	621	T
Hydrophone	619	T	Hydrophone	622	T	Hydrophone	643	T
Hydrophone	659	T	Hydrophone	662	T	Hydrophone	683	T
SBE56	697	T	SBE56	700	T	SBE56	721	T
Hydrophone	699	T	Hydrophone	702	T	Hydrophone	723	T
Hydrophone	739	T	Hydrophone	742	T	Hydrophone	763	T
Hydrophone	779	T	Hydrophone	782	T	Hydrophone	803	T
SBE56	797	T	SBE56	800	T	SBE56	821	T
Hydrophone	819	T	Hydrophone	822	T	Hydrophone	843	T
Hydrophone	859	T	Hydrophone*	862	T	Hydrophone	883	T
SBE56	897	T	SBE56	900	T	SBE39	921	T,P
Hydrophone	899	T	Hydrophone	902	T	Hydrophone	923	T
Hydrophone	939	T	Hydrophone	942	T	Hydrophone	963	T
Hydrophone	979	T	Hydrophone	982	T	Hydrophone	1003	T
SBE39	997	T,P	SBE37-SM	1000	T,S,P	SBE56	1021	T
Hydrophone	1019	T	Hydrophone	1022	T	Hydrophone	1043	T

An overview of all the instruments mounted on the moorings A-N2, B-N3 and C-N1 with depth and measured parameters. The hydrophone modules are listed as hydrophone. Asterisk indicate instruments that were excluded due to a malfunction.

interval starts at about the depth of the lacking salinity measurements, and the depth of the ITPs reach down to about 750 m.

The sound speed in a liquid is given by the following expression

$$C = \sqrt{\frac{1}{\rho K}} \tag{1}$$

where ρ is the density and K is the adiabatic compressibility of the medium (e.g. seawater). For seawater, both these quantities have a complicated dependence on temperature, pressure, and salinity. Ideally would theoretical expressions based on fundamental physical mechanisms be used to compute ρ and K, and hence the sound speed from Eq. 1, but since no such expressions exist, an alternative approach has been developed. Several empirical formulas with a polynomial in the temperature, the salinity, and the pressure have been formulated. The two most accepted empirical formulas are the Del Grosso equation (1974), also known as the NRL II equation, and the Chen and Millero equation. The Del Grosso equation is found to be more accurate with the long-range acoustic measurements, at low temperatures (0 °C to 15 °C), and high pressures (> 200 dbar) than the Chen and Millero equation (Dushaw et al., 1993b). The Del Grosso equation will therefore be used to calculate the sound speed, and it can be written as follows:

$$\begin{aligned} C = {} & c_0 + a_1 T + a_2 T^2 + a_3 T^3 + a_4 T^4 + a_5 (S-35) + a_6 P^2 \\ & + a_7 P^3 + a_8 T (S-35) + a_9 T (S-35)^3 + a_{10} (S-35) \\ & + a_{11} TP + a_{12} TP^2 + a_{13} TP^3 + a_{14} T^2 P^2 + a_{15} T^3 P \\ & + a_{16} (S-35) P + a_{17} (S-35) P^2 + a_{18} (S-35) P^3 + \\ & + a_{19} (S-35)^2 P + a_{20} (S-35)^2 P^2 + a_{21} (S-35)^3 \\ & + a_{22} T (S-35) P + a_{23} T^2 (S-35) P, \end{aligned} \tag{2}$$

where C is the sound speed (m s^{-1}), the T is temperature (°C), the S is salinity, and the P is pressure converted to kg cm^{-2} using the acceleration of gravity, g = 9.80665 m s^{-2}. The coefficients in Eq. 2 are:

$$
\begin{aligned}
c_0 &= 0.140194964197 \times 10^{4} & a_{12} &= -0.131201344149 \times 10^{-5} \\
a_1 &= 0.500642920686 \times 10^{1} & a_{13} &= 0.402773046625 \times 10^{-9} \\
a_2 &= -0.583540720391 \times 10^{4} & a_{14} &= 0.144431845812 \times 10^{-7} \\
a_3 &= 0.349631461597 \times 10^{-3} & a_{15} &= 0.1012322803918 \times 10^{-5} \\
a_4 &= -0.164875703289 \times 10^{-5} & a_{16} &= 0.157450572397 \times 10^{-1} \\
a_5 &= 0.134606695473 \times 10^{-1} & a_{17} &= 0.533284097890 \times 10^{-5} \\
a_6 &= -0.593403057954 \times 10^{-4} & a_{18} &= 0.353545616177 \times 10^{-9} \\
a_7 &= -0.209170685764 \times 10^{-7} & a_{19} &= -0.522655412446 \times 10^{-3} \\
a_8 &= -0.112689485296 \times 10^{-1} & a_{20} &= -0.858535445194 \times 10^{-7} \\
a_9 &= -0.583732276240 \times 10^{-6} & a_{21} &= 0.572274443678 \times 10^{-5} \\
a_{10} &= 0.103658662691 \times 10^{-3} & a_{22} &= -0.117388164634 \times 10^{-4} \\
a_{11} &= 0.595900933419 \times 10^{-5} & a_{23} &= 0.597262459578 \times 10^{-6}
\end{aligned}
$$

3.2 Supplementary hydrographic data

Supplementary hydrographic data have been used to calculate the mean temperature of the AWL along the CAATEX section in the Eurasian Basin. The expendable conductivity-temperature-depth (XCTD), the conductivity-temperature-depth (CTD), and the expendable bathythermograph (XBT) stations have been selected based on their closeness to the CAATEX section. The cruise data between 1995 and 2015 have been downloaded from the Unified Database for Arctic and Subarctic Hydrography (UDASH). Data made publicly available after 2015 have not been included in UDASH yet. The UDASH offers a high-quality data collection of temperature and salinity in the period from 1980 to 2015 from the Arctic Mediterranean. The XBT data was collected during the Le Commandant Charcot cruise in 2021 (courtesy of the Nansen Environmental and Remote Sensing Centre, Bergen, Norway).

Table 3: The supplementary cruises

Cruise (year)	Date	Latitude [N]	Longitude [E]	Instrument type
SCICEX (1995)	27.04 - 04.05	85.33 - 88.29	51.36 - 119.07	XCTD
SCICEX (1997)	04.09 - 05.09	84.25 - 89.52	- 29.92 - 26.30	XCTD
SCICEX (1998)	10.08 - 12.08	85.04 - 88.59	47.10 - 139.68	XCTD
SCICEX (2000)	17.10 - 18.10	85.00 - 88.55	46.00 - 137.35	XCTD
SCICEX (2001)	03.06 - 04.06	85.00 - 88.55	45.98 - 139.76	XCTD
ODEN (2001)	17.07 - 23.07	83.78 - 88.43	31.95 - 109.84	CTD
SCICEX (2003)	06.10 - 10.10	85.29 - 88.53	47.15 - 126.61	XCTD
ODEN (2005)	13.09 - 23.09	85.95 - 89.99	48.52 - 89.05	CTD
Polarstern (2011)	11.08 - 23.08	84.09 - 89.97	55.03 - 146.63	CTD
Polarstern (2012)	22.09 - 27.09	84.80 - 88.81	50.00 - 57.26	CTD
Polarstern (2015)	29.08 - 07.09	85.28 - 89.65	58.29 - 61.36	CTD
Le Commandant Charcot (2021)	08.09 - 11.09	82.75 - 88.36	30.29 - 58.10	XBT

Overview of the selected cruises to the Eurasian Basin between 1995 and 2021, and the ITP95 profile. It provides the cruise name and year, date range, longitude and latitude range, and instrument type.

The mean temperature of the AWL has been calculated in two ways. The first procedure in calculating the mean temperature of the AWL was using the definition of the AWL with temperatures above 0 °C. The second procedure calculated the mean temperature of the AWL between 300 m and 700 m, since this layer is the AWL in the Ocean Reanalysis Multi-Model-Mean (ORA MMM). The overview of the date, the latitude, and longitude range, and the instrument type from the selected cruises are given in Table 3.

4 Results

4.1 The hydrographic conditions at the CAATEX moorings in the Nansen Basin

Temperature and salinity diagrams

Temperature and salinity diagrams of daily mean values are presented in Figure 9. Salinity was only measured at six discrete depths between 50 m and about 175 m on the three moorings (see Table 2). The colors in the figure are coordinated to show the observations from the instruments deployed at about the same depths at each mooring (see legend).

The temperature and salinity diagram from the A-N2 mooring location (Figure 9a) displays a relatively wide range in temperature and salinity characteristics measured between 50 m and 147 m. The PSW was mostly found between 50 m and 87 m, but some daily mean temperatures lower than 0 °C were also found at 107 m. Temperatures close to the freezing point were only found at 50 m, with salinities between 34.08 and 34.17. The salinity of the PSW ranged between 33.95 and 34.53, and the bend was seen at about 34.25. The shape of the bend was relatively smooth between the PSW and the AW. The AW was present at all depths during the measurement period. Temperatures of AW higher than 3 °C were found between 67 m and 147 m, with salinities greater than 34.84. The salinity of the AW ranged between 34.41 and 35.00. The AW measured at 50 m and 67 m was generally less saline than the AW measured at 127 m and 147 m.

At the B-N3 mooring location (Figure 9b), the PSW was found mainly between 50 m and 90 m, but also down to 130 m during the measurement period. The temperature of the PSW at 50 m had near freezing-point temperatures with salinities down to 34.19. Near freezing-point temperatures were also present at 70 m. However there were higher temperatures present at 50 m and 70 m, up to - 1.62 °C and - 1.25 °C, respectively. The salinity range of the PSW was between 34.19 and 34.58, and a relatively sharp bend was found near the salinity of 34.35. Both PSW and AW were present at 110 m and 130 m during the year. The highest AW temperature of 2.23 °C was found at 150 m. The salinity range of the AW was between 34.56 and 34.89.

At the C-N1 mooring location (Figure 9c), the PSW was mainly found between 50 m and 131 m. The temperature at 50 m lied along the freezing-point line between the salinities of 34.06 to 34.35. At 91 m, the temperature was near the freezing-point, but showed also higher temperatures, up to - 1.44 °C. At 111 m, the temperature was near the freezing-point, but had mostly temperatures higher than this, up to - 0.69 °C. The bend in the lower halocline water was found around the salinity of 34.35, and the shape of the bend was sharp. The PSW and AW were both present at 131 m during the measurement period. Whereas only AW was found at 151 m and 171 m. The highest temperature of the AW was 2.01 °C at 171 m. The salinity range of the AW was between 34.56 and 34.88.

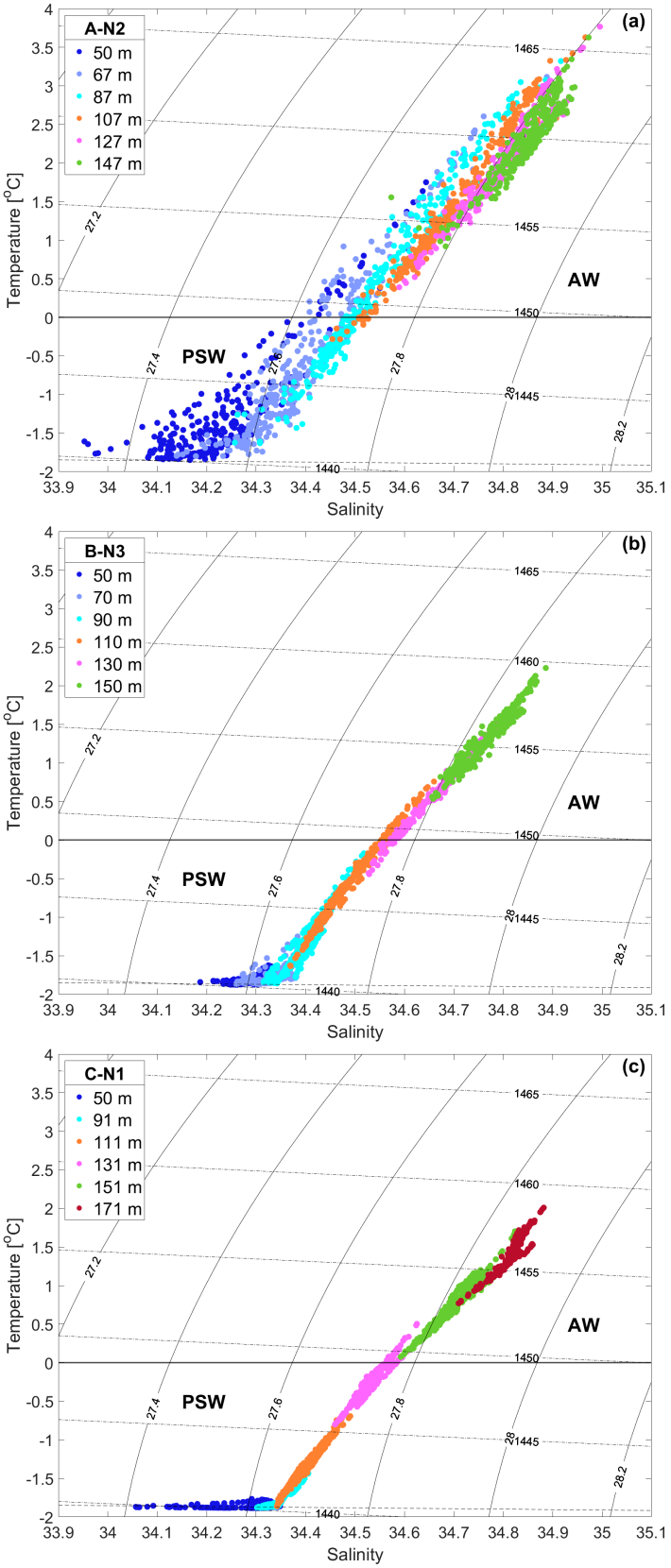

Figure 9: Temperature and salinity diagrams of daily mean temperatures and salinities from mooring A-N2 (a), B-N3 (b), and C-N1 (c). Colors display the depths. The black line (T = 0 °C) indicates the boundary between the Polar Surface Water (PSW) and the Atlantic Water (AW). The dotted line is the freezing point line. The sound speed isolines are shown by the dashed and dotted lines and the density isolines are the thin solid lines.

When comparing the temperature and salinity diagrams from the three moorings, the main differences to take note of are: (1) The depth of the boundary between the PSW and AW varied between the depths of 50 m and 107 m at the A-N2 mooring. Whereas the boundary varied between 110 m and 130 m at the B-N3 mooring, and was found around 131 m at the C-N1 mooring. (2) The range in temperature measured at 50 m at the A-N2 mooring was large, whereas it was especially stable at the C-N1 mooring. (3) The bend in the lower halocline water was more smooth at the A-N2 mooring compared to at the B-N3 and C-N1 moorings. (3) The AW at the A-N2 mooring had a maximum temperature of 3.77 °C (at 127 m) and this decreased northward to 2.23 °C (at 150 m) at the B-N3 mooring and to 2.01 °C (at 171 m) at the C-N1 mooring.

Time series

The following section will present the time evolution of temperature and salinity between September 2019 and July 2020 at selected depths from the three moorings. To investigate possible causes of the variability seen in the temperature and salinity time series, daily mean current data from each mooring are also presented. The time series from mooring A-N2 shows only the temperature and salinity from 50 m and 87 m, to compare the measurements from 50 m and the upper boundary of the AWL around 87 m (Figure 10). The shaded thin lines in the figures are daily mean values and the solid thick lines are 1-month running mean values.

The daily mean temperature time series (thin lines) shows that PSW was present at 50 m most of the year at the A-N2 mooring location (Figure 10a.1). However, there were several occasions where AW was present at this depth. The two most pronounced episodes of AW at 50 m occurred at the end of November 2019 and at the beginning of March 2020 (upward arrows). During these two episodes, the maximum daily mean temperatures were 1.4 °C and 1.75 °C, respectively. The salinity time series at 50 m corresponded well with the temperature time series, with increasing salinity during the episodes of AW. Note the salinity drop (down to 33.95) in February 2020 (downward arrow). At 87 m, AW was present most of the year. However, the daily mean temperature time series showed large variability in frequency and amplitude. The minimum and maximum daily mean temperatures at 87 m are − 1.63 °C (31.05.2020) and 3.32 °C (24.06.2020), respectively. The maximum temperature occurred in the end of June, but it was not a long lasting episode. The two most pronounced episodes of higher AW temperatures seen at 50 m, were also visible at 87 m. During these episodes, the maximum daily mean temperatures were 2.53 ° C and 3.05 ° C, respectively. In between these episodes, PSW was mainly present at 87 m.

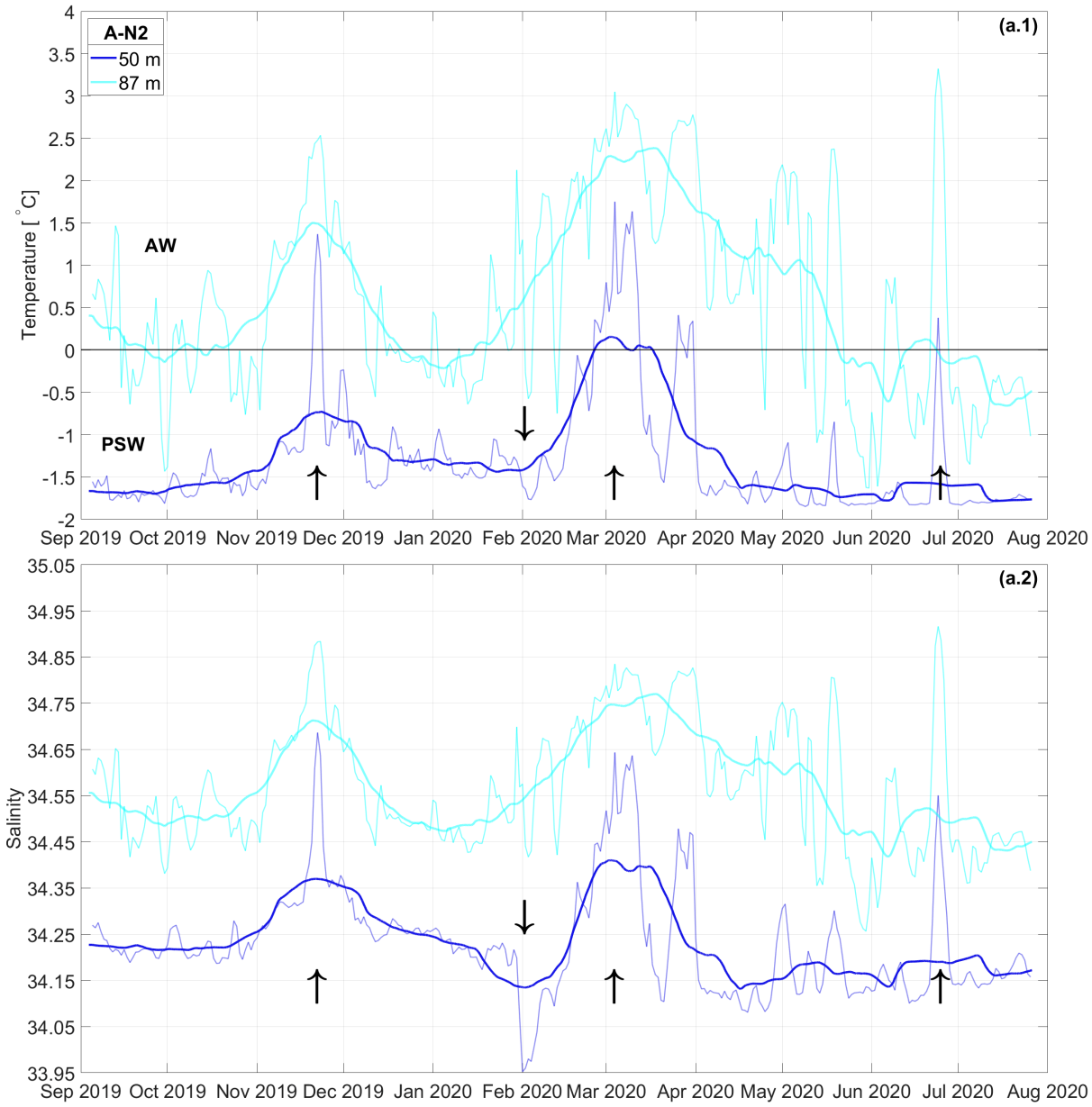

Figure 10: Time series of a.1) temperature and a.2) salinity at selected depths near the surface and upper boundary of the AWL at the A-N2 mooring. The colors represent time series measured at approximately the same depth at each mooring. The black arrows show special episodes described in the text. The black line (T = 0 °C) indicates the lower temperature limit of AW.

The daily mean current speed and current direction profiles cover the water column from the instrument depth at about 50 m and up to about 10 m (Figure 11). The current profiles showed a variable current speed and direction at different depths throughout the year. The current direction was especially variable when the current speed was low. The current speed was generally lower than 5 cm s^{-1} during the year, but there were frequent occasions of higher current speed (> 10 cm s^{-1}) between about 10 m and 20 m. Further down in the water column, the current speed was generally low, except for the pronounced current speed increases (> 10 cm s^{-1}) at the end of November, the beginning of March, and at the end of June. Additionally, pressure increases can be seen associated with the increasing

current speed at the end of November and at the end of June (Figure 12).

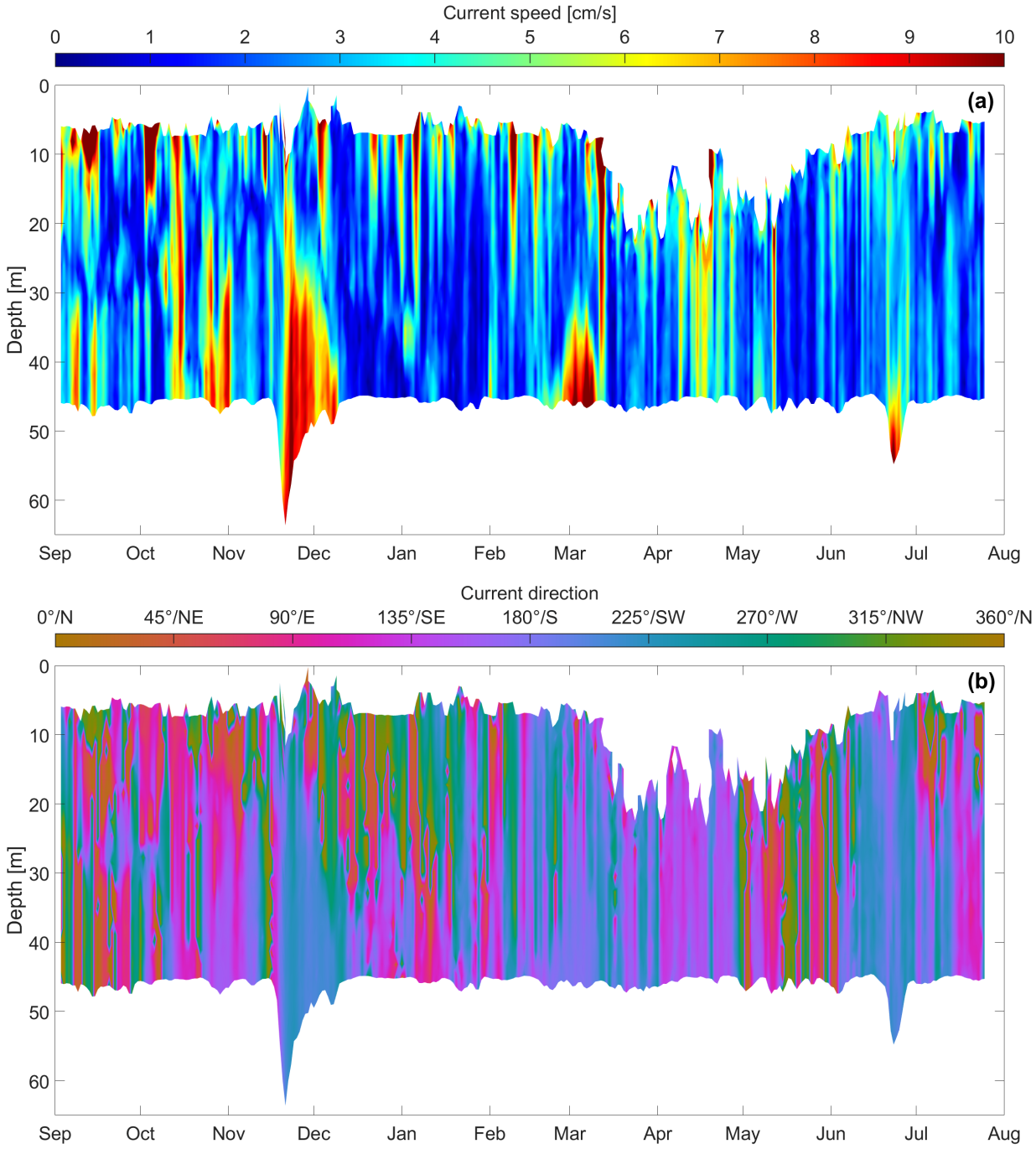

Figure 11: Time series of a) daily mean current speed and b) current direction profiles from the ADCP deployed at 47 m on the A-N2 mooring.

A closer look at temperature and pressure and the nearest current speed at the A-N2 mooring are presented in Figure 12. The pressure data showed a generally steady mooring with little vertical movement, apart from an increase in pressure to about 70 dbar at the end of November and to about 62 dbar at the end of June. A correlation between temperature and pressure gives a correlation coefficient of 0.35 which is weak, but the peaks at the end

of November and at the end of June fit well. Whereas the current speed varied frequently mainly between 0 cm s^{-1} and 7 cm s^{-1}. The correlation coefficient between the current speed and the temperature was 0.50 which is moderate, with current speeds of about 10 cm s^{-1} during the episodes at the end of November, the beginning of March, and at the end of June.

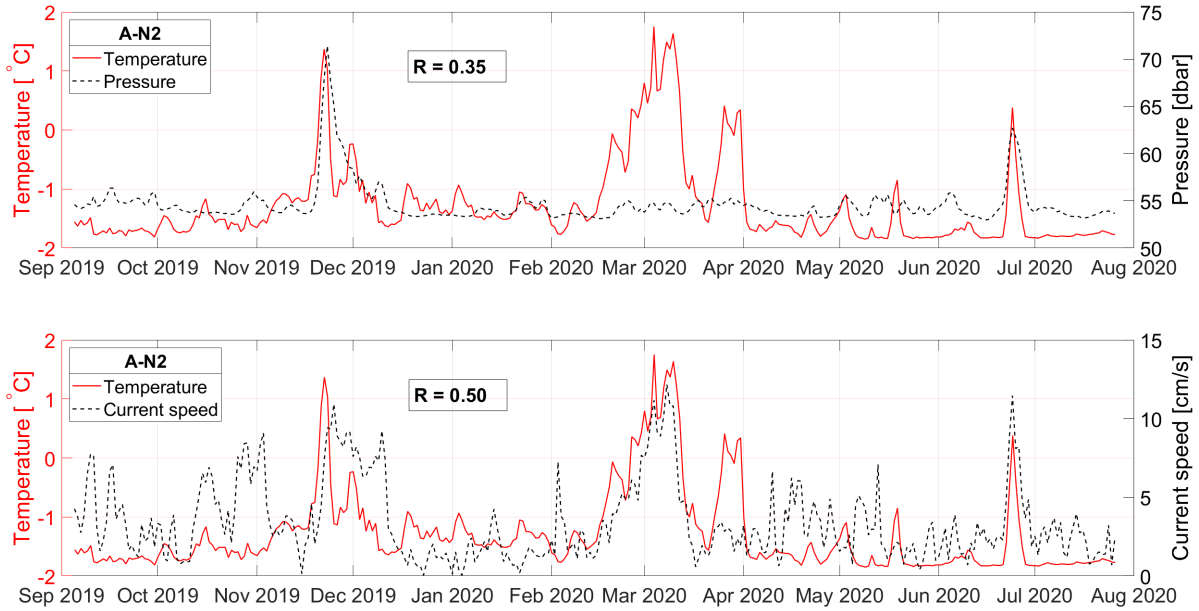

Figure 12: Time series of daily mean temperature and pressure (upper panel) and daily mean temperature measured by the SBE37-SMP deployed at 50 m and the nearest current speed (lower panel) from the ADCP on the A-N2 mooring. The correlation coefficients are shown in the text boxes.

At mooring B-N3, the daily mean temperature at 50 m was relatively stable throughout the time series (Figure 13b.1). Note the salinity drop at 50 m in January (Figure 13b.2), occurring at the same time as a temperature and salinity decrease at depths between 90 m and 130 m. The 1-month running mean temperatures at 50 m and 70 m were stable and close to equal during the year. Greater variability occurred at 90 m, 110 m, and 130 m. In January 2020, temperature and salinity decreased at these depths (downward arrow), and the upper boundary of the AWL was found at 130 m. In April and May, the temperature and salinity increased again (upward arrow), and the upper boundary of the AWL was found at 110 m. From May to July the temperature decreased at 90 and 110 m.

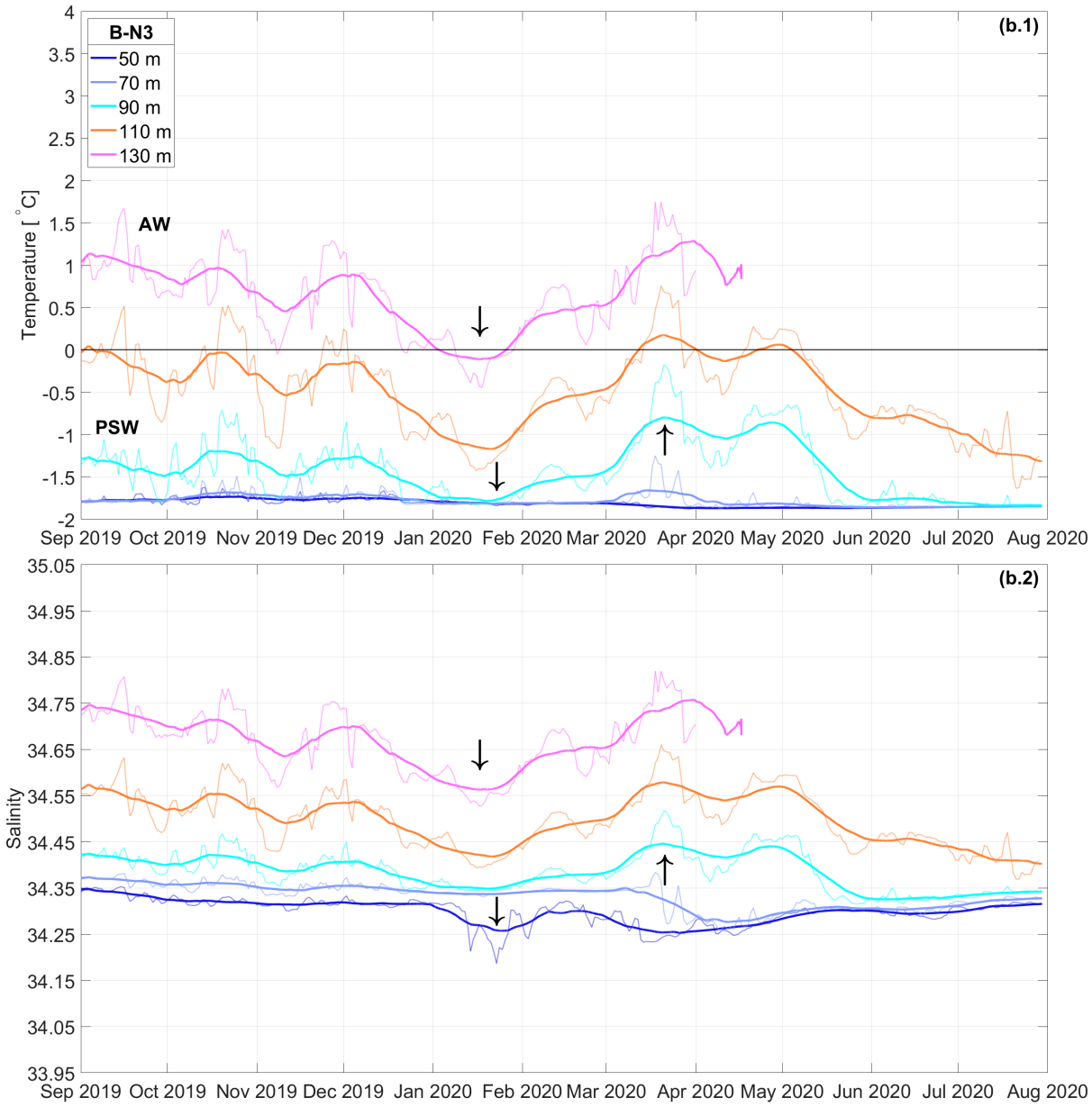

Figure 13: Time series of a) temperature and b) salinity at selected depths at the B-N3 mooring. These depths are chosen to investigate the surface and the upper boundary of the AWL. The colors represent time series measured at approximately the same depth at each mooring. The black arrows show special episodes described in the text. The black line (T = 0 °C) indicates the lower temperature limit of AW.

The current speed profile measured at the B-N3 mooring (Figure 14a) showed generally stronger current speeds during autumn and in late July. The strongest current speeds (> 10 cm s^{-1}) were found during short time periods between 10 m and 20 m. Deeper down between 40 m and 50 m, the current speeds were about 4 cm s^{-1} and 6 cm s^{-1} during autumn and in late July. The current speed was generally lower than 3 cm s^{-1} during the rest of the year, especially in winter and spring. The current direction was highly variable throughout the year with no prevailing direction.

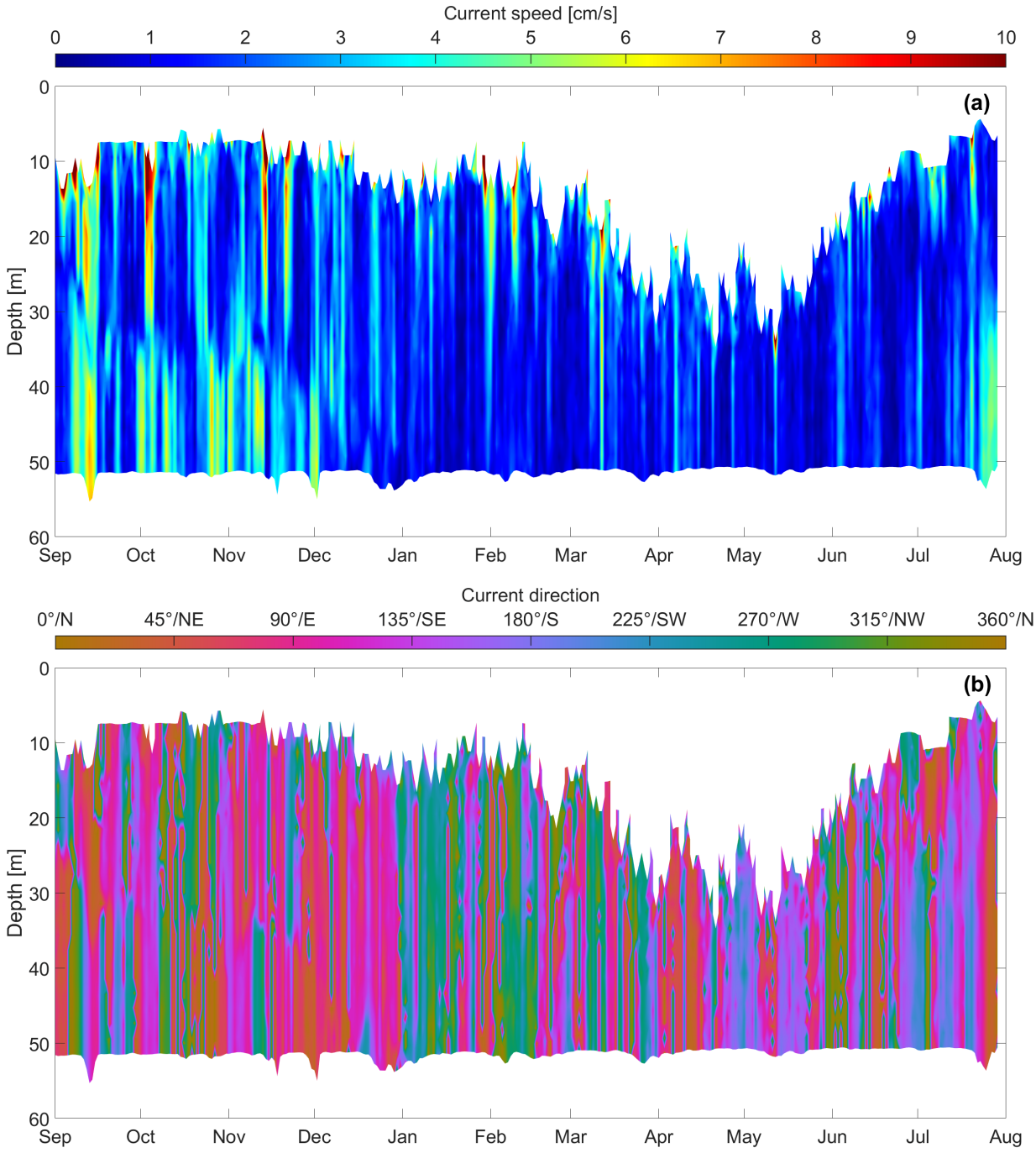

Figure 14: Time series of daily a) mean current speed and b) current direction from the ADCP deployed at 47 m on the B-N3 mooring.

A closer look at temperature and pressure and the nearest current speed at the B-N3 mooring are presented in Figure 15. The pressure data showed that the vertical movement was low, less than about 2 m, throughout the year (Figure 15). A correlation between temperature and pressure gives a correlation coefficient of 0.36 which is weak, but the temperature and pressure showed generally slightly more variability during autumn than in winter and spring. During winter and spring, the temperature at 50 m was cold, and decreased gradually from -1.8 °C to -1.88 °C from January to May. Whereas the current speed varied

frequently between 0 cm s^{-1} and 6 cm s^{-1}. A correlation between temperature and current speed gives a correlation coefficient of 0.35 which is weak, but the higher temperature and current speed variability occurred mainly during autumn.

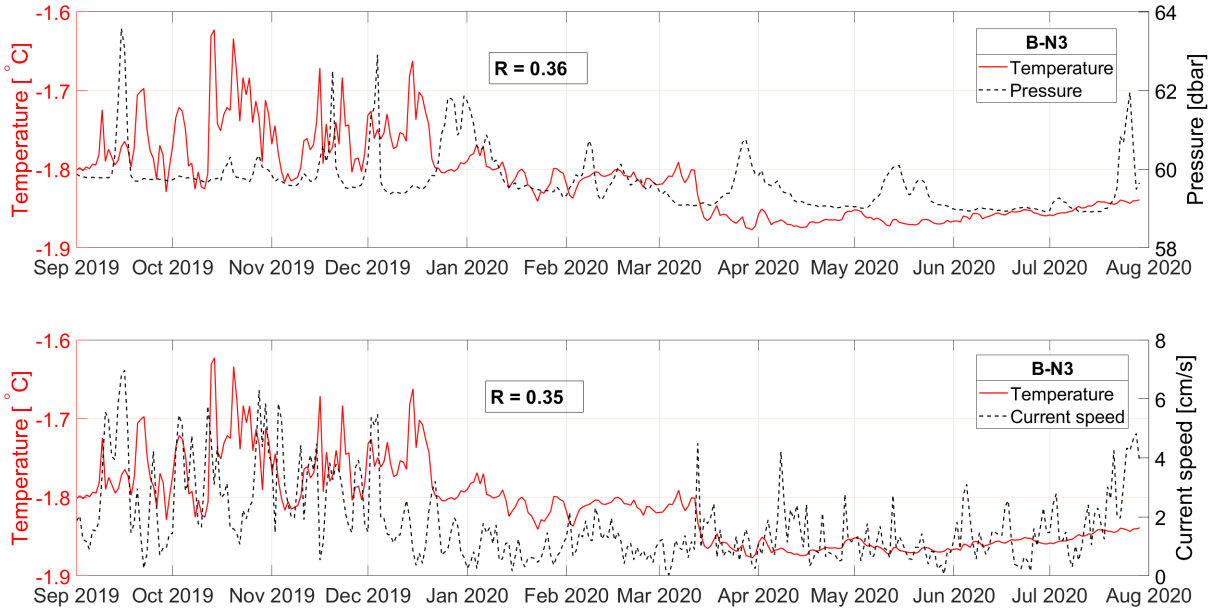

Figure 15: Time series of daily mean temperature and pressure (upper panel) and daily mean temperature measured by the SBE37-SMP deployed at 50 m and the nearest current speed (lower panel) from the ADCP on the B-N3 mooring. The correlation coefficients are shown in the text boxes.

The temperature time series from the C-N1 mooring (Figure 16c.1) showed that the PSW was mainly present in the upper 131 m of the water column throughout the year. The temperature at 50 m was mainly below − 1.80 °C throughout the year. The salinity at 50 m was stable between 34.3 and 34.35, except for the salinity drop of about 0.24 down to 34.06 in February (downward arrow, Figure 16c.2). Greater variability occurred at 111 m, 131 m, and 151 m. At the end of November, temperature and salinity increased at these depths (upward arrow), and the upper boundary of the AWL was found at around 130 m depth.

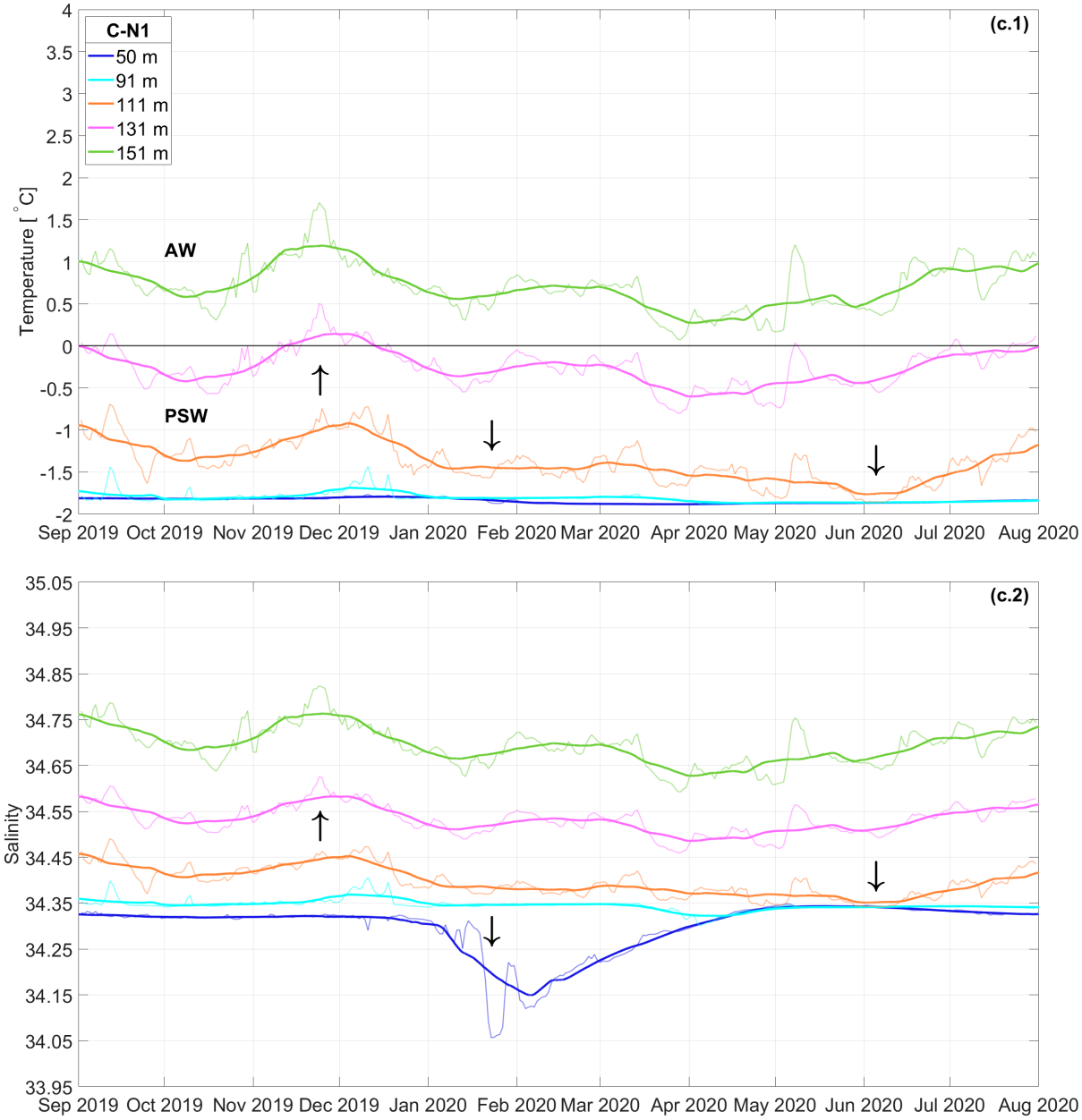

Figure 16: Time series of a) temperature and b) salinity at selected depths at the C-N1 mooring. These depths are chosen to investigate the surface and the upper boundary of the AWL. The colors represent time series measured at approximately the same depth at each mooring. The black arrows show special episodes described in the text. The black line (T = 0 °C) indicates the lower temperature limit of AW.

The current speed above the C-N1 mooring (Figure 17a) was generally lower than 4 cm s^{-1} between September 2019 and July 2020. The current direction was highly variable throughout the year, with no prevailing direction (Figure 17b). There were some higher current speeds (> 6 cm s^{-1}) in short periods between 10 m and 30 m during autumn. Whereas the current speed was mainly lower than 4 cm s^{-1} below 30 m throughout the year.

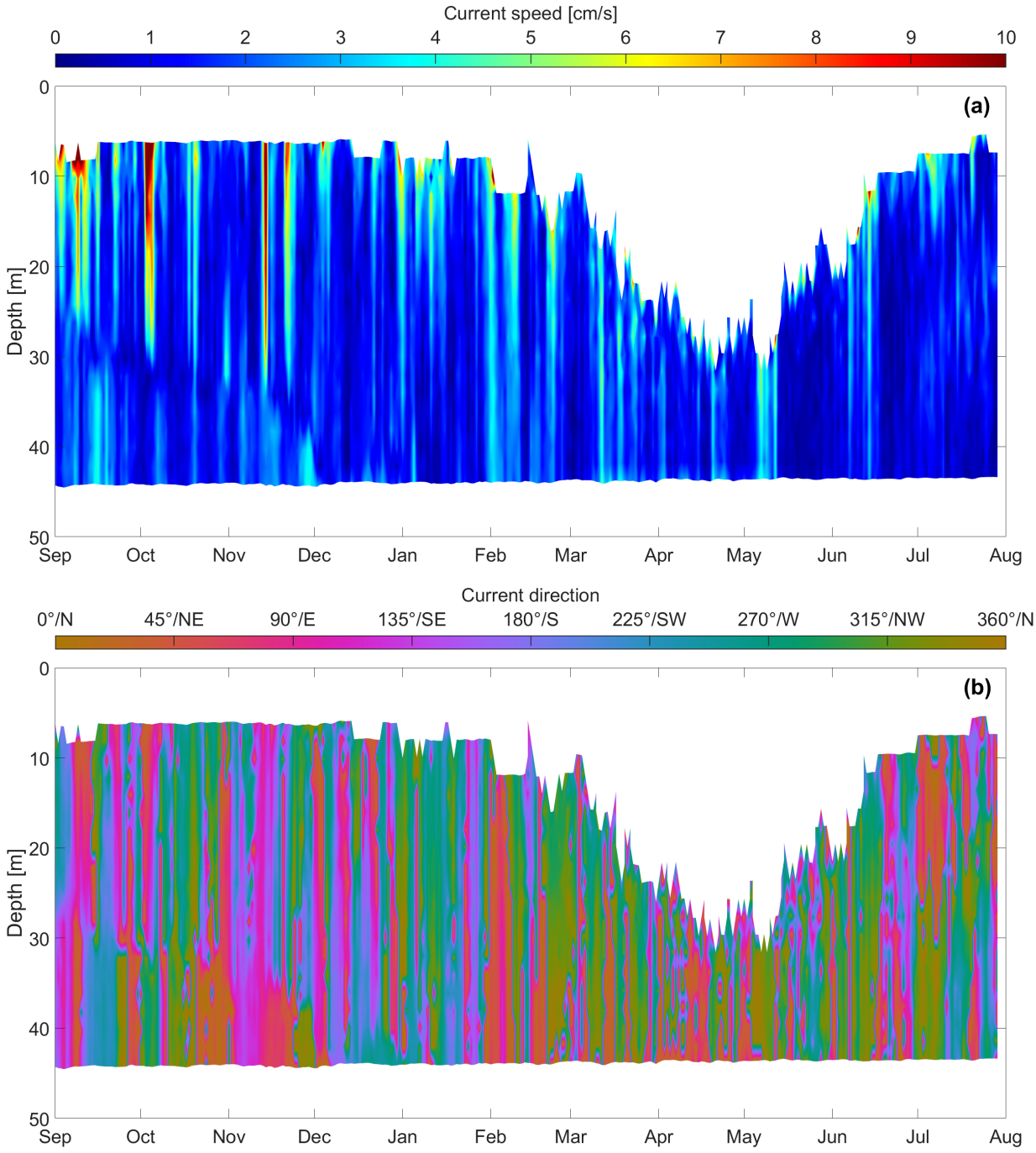

Figure 17: Time series of daily mean current speed and direction from ADCP deployed at 47 m on the C-N1 mooring.

The temperature and pressure from the SBE37-SMP deployed at 50 m (Figure 18) showed that the temperature varied little during the year. Looking at the small variations, the temperature was slightly higher, at about - 1.82 °C during autumn, and dropped at the end of January down to about − 1.87 ° C for a short period. From February till mid-April it decreased gradually to - 1.88 ° C, before increasing slowly to − 1.84 ° C by the end of summer. The pressure showed a very stable mooring throughout the year, only moving gradually up about 1 m after December. The correlation coefficient between the pressure

and temperature was 0.75 which is strong. The current speed measurement nearest the temperature measurement varied frequently between small speeds ($\sim$ 0 cm s^{-1} and $\sim$ 4 cm s^{-1}) during the year (Figure 18) and there was no correlation between the current speed and the temperature (R = -0.01).

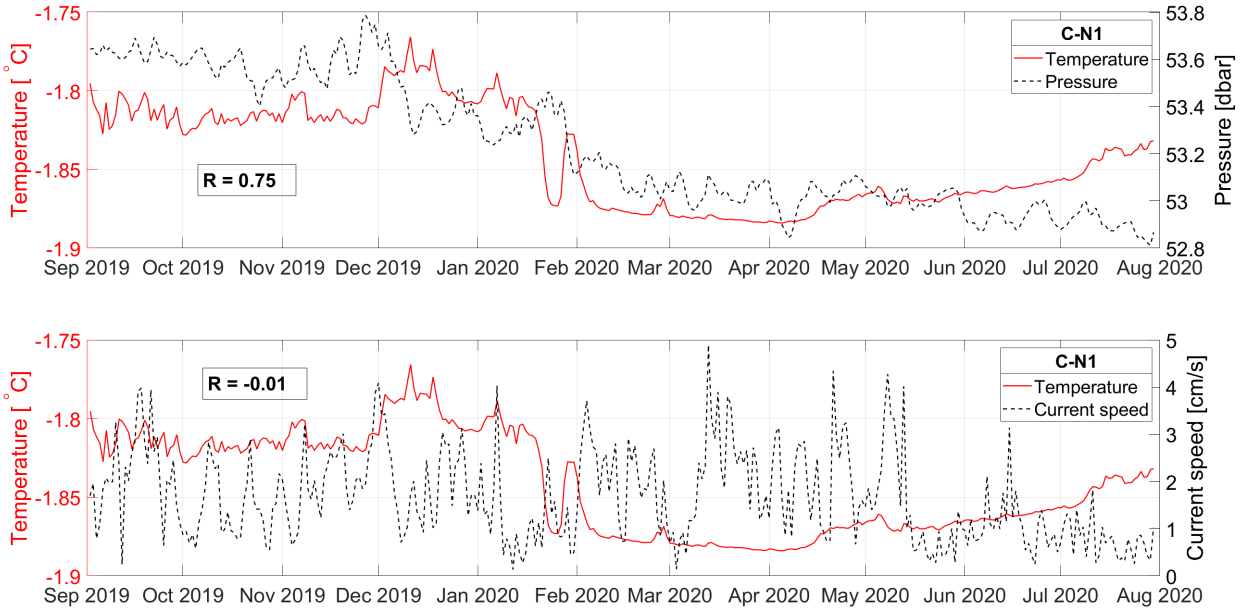

Figure 18: Time series of daily mean temperature and pressure (upper panel) and daily mean temperature measured by the SBE37-SMP deployed at 50 m and the nearest current speed (lower panel) from the ADCP on the C-N1 mooring. The correlation coefficients are shown in the text boxes.

When comparing the time series from the moorings, larger and more high-frequency variability in temperature and salinity were seen at the A-N2 mooring, whereas it was more stable throughout the whole year at the B-N3 and C-N1 moorings. Higher AW temperatures were measured at the A-N2 mooring, compared to at the B-N3 and C-N1 moorings. In addition, the upper boundary of the AW was shallower at A-N2 mooring compared to at the B-N3 and C-N1 moorings. A salinity drop at the end of January and beginning of February occured at all three mooring locations, where the most pronounced drops were at the A-N2 and C-N1 moorings.

Ice draft

The presence of sea ice above the A-N2, B-N3, and C-N1 moorings are presented by the daily mean ice draft measured by the upward looking sonars mounted at about 46 m on each mooring (Figure 19). The white bands in the ice draft time series from the A-N2 and B-N3 moorings are missing data.

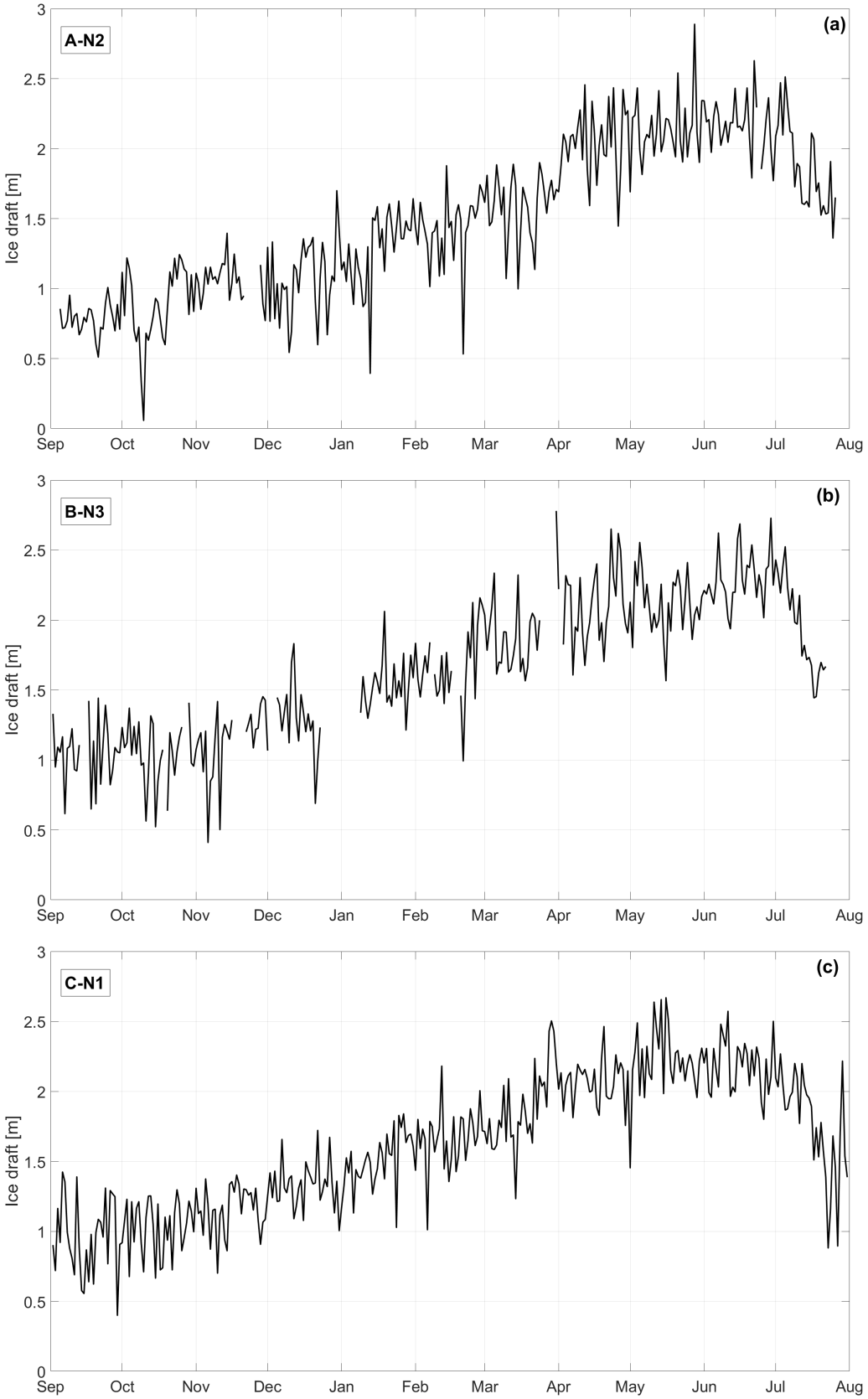

Figure 19: Time series of daily mean ice draft above the (a) A-N2 mooring, (b) N-N3 mooring, and (c) C-N1 mooring between September 2019 and July 2020.

The ice draft above the A-N2 mooring was thinnest during October, where the thickness was close to zero for a short period. Generally during autumn, the thickness was about 1 m or less. From January it gradually increased to about 2 m in April, but some "jumps" of thinner ice were seen in January and February. During summer the thickness was relatively stable above 2 m before it started to decrease in July.

The ice draft above the B-N3 mooring was generally about 0.5 m to 1 m during autumn. From January it gradually increased to about 2 m to 2.5 m in April. During summer the thickness was relatively stable above 2 m before it started to decrease in July.

The ice draft above the C-N1 mooring was at the thinnest during autumn, generally with a thickness of around 1 m. The ice draft thickness increased gradually from December to about 2 m to 2.5 m in April. During summer the thickness was relatively stable above 2 m before it started to decrease in July.

Temperature profiles from the moorings

The monthly mean temperature profiles at the three moorings A-N2, B-N3, and C-N1 between September 2019 and July 2020 are shown in Figure 20. Each mooring were equipped with 46 temperature loggers between 50 m and about 1000 m.

The monthly mean temperature profiles from the southernmost mooring, A-N2, showed large variation between the months, especially in the upper 50 to 300 m. There were no temperature measurements above 50 m. The PSW is left of the black vertical zero-degree isotherm, indicating the boundary between the PSL and the AWL. The PSW was present down to 59 m throughout the whole year, except March which had a mean temperature of 1.11 ° C at 59 m. The maximum and minimum monthly mean temperatures at 67 m were 1.60 °C and − 1.56 ° C in March and July, respectively, this was the depth of the most pronounced mean temperature variation (3.16 ° C). At the next depth level (87 m) AW (right of the black vertical zero-degree isotherm) was mainly present throughout the year, except in July when the monthly mean temperature was − 0.65 ° C (i.e PSW). The maximum monthly mean temperature at 87 m was 2.39 ° C in March and the minimum was − 0.65 ° C in July, a difference of 3.04 ° C. Further down, the temperature in the AW core varied between the months and also the depth of the AW core. March was the month with the highest mean temperature (2.90 ° C) and the shallowest depth (147 m), while July was the month with the lowest mean temperature of 2.34 ° C, and the deepest depth of 219 m. Below the AW core, the mean temperatures and the monthly variations decreased gradually. The depth of the upper boundary of the AWL varied between less than 50 m (shallower than the uppermost instrument) in March and about 100 m in July. The depth of the lower boundary of the AWL varied between 850 m in April and 920 m in November.

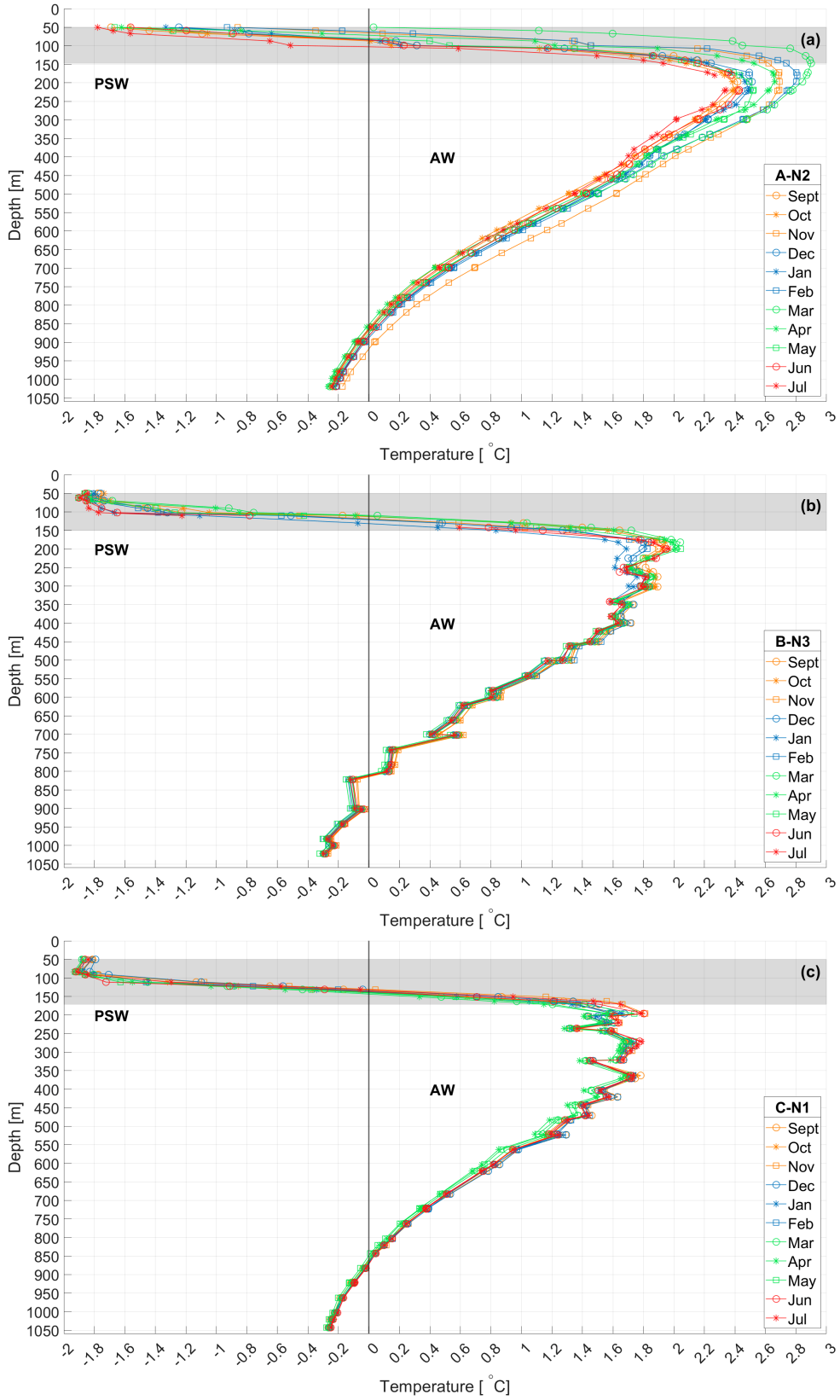

Figure 20: Vertical profiles of monthly mean temperatures measured by all instruments mounted on mooring a) A-N2, b) B-N3 and c) C-N1 between September 2019 and July 2020. The colors display the seasons of the year. The markers show the instrument depth and separate the different months within one season (see legend). Shaded area shows the depth interval of instruments measuring salinity. The black line is the zero-degree isotherm, the lower temperature limit of the AW.

The monthly mean temperature profiles from the B-N3 mooring showed less variation between the months in the upper 50 m to 70 m compared to further down between 90 m and 225 m. At 50 m, the monthly mean temperature was relatively low throughout the year, with the maximum and minimum mean temperatures of − 1.74 °C in November and − 1.87 in April and May, respectively. The monthly mean temperature decreased slightly between 50 m and 62 m for all months except March. The monthly mean temperature of the PSW between 50 m and 70 m were low, where the monthly mean temperature maximum of − 1.68 °C at 70 m was in March. Below this at 90 m, the monthly mean temperature of the PSW increased and the variation between the months were larger. March was the month with the highest monthly mean temperature of − 0.92 °C compared to the minimum of − 1.84 °C in July. Further down, at 110 m, the PSW was present throughout most of the year, except in March where the mean temperature was 0.06 °C. The 110 m depth level was the depth of the most pronounced variation between the months, where the maximum and minimum monthly mean temperatures were 0.06 °C and − 1.23 °C in March and July, respectively. Below this, at 130 m, AW was mainly present throughout the year, except in January with the mean temperature of − 0.07 °C (i.e. PSW). Further down the monthly mean temperatures increased with depth down to 182 m, however, the AW core was not so distinct due to temperature inversions between 142 m and 400 m. By definition, the maximum monthly mean AW core temperature was 2.04 °C in May with a depth of 200 m. While the minimum monthly mean AW core temperature was 1.76 °C at the mean depth of 275 m in January. Below 400 m, the monthly mean temperatures gradually decreased. However, note the presence of temperature inversions between 700 m and 1000 m. The mean depth of the upper boundary of the AWL varied between 110 m in March and about 130 m in January. The mean depth of the lower boundary of the AWL varied between 805 m in May and 815 m in November.

The monthly mean temperature profiles from the C-N1 mooring showed less variation in the upper 50 m to 91 m compared to the depths between 111 m and 171 m. From 50 m down to 83 m, the monthly mean temperatures decreased with depth in all months. The PSW was present down to 131 m throughout most of the year, except in November with the mean temperature of 0.04 °C. At the next depth level (151 m) AW was present throughout the whole year, with the maximum and minimum monthly mean temperatures of 1.16 °C and 0.33 °C in November and April, respectively. Further down the monthly mean temperatures increased down to 196 m. Below this there were temperature inversions present between 196 m and 523 m, showing no distinct AW core. The maximum AW temperature of 1.81 °C was in November at the mean depth of 196 m. Below the temperature inversions reaching down to 523 m, the mean temperatures decreased gradually with depth down to 1043 m. The mean depth of the upper boundary of the AWL varied between 130 m in November and 145 m in April. The mean depth of the lower boundary of the AWL varied between 850 m in May and 870 m in July.

Comparison of the monthly mean temperature profiles measured at the three moorings

show similarities and differences. The largest variations in monthly mean temperatures were found at depths around the upper boundary of the AWL. The AW core was most pronounced at mooring A-N2, and exhibited the highest mean AW core temperature (2.90 °C) and the shallowest AW core depth (147 m), whereas the structure in the monthly mean temperature profiles at B-N3 and C-N1 did not display a distinct AW core. However, the maximum AW temperature decreased northwards and the corresponding depth increased. The variability in the monthly mean temperature measured at the uppermost instrument (50 m) was smaller at B-N3 (0.13 °C) and C-N1 (0.09 °C) moorings than at the A-N2 (1.81 °C) mooring. Note that the shallower upper boundaries of the AWL were associated with the higher AW temperatures at the depths around the core. Additionally, the monthly mean temperature profiles from the moorings display different shapes. The monthly profiles from mooring C-N1, the northernmost mooring, displayed a clear "zigzag" structure between 163 m to 402 m. This "zigzag" structure was also present in the profiles from mooring B-N3. However, at the B-N3 mooring location it was present in two different layers, between 142 m to 400 m, and between 700 m to 1000 m.

The main findings of the temperature variability at the three moorings in the Nansen Basin are presented in Figure 21. The mean temperature profile from September 2019 to July 2020 at each mooring are displayed by the black solid line. The blue shaded area shows the variability with the minimum and maximum daily mean temperatures as the edges.

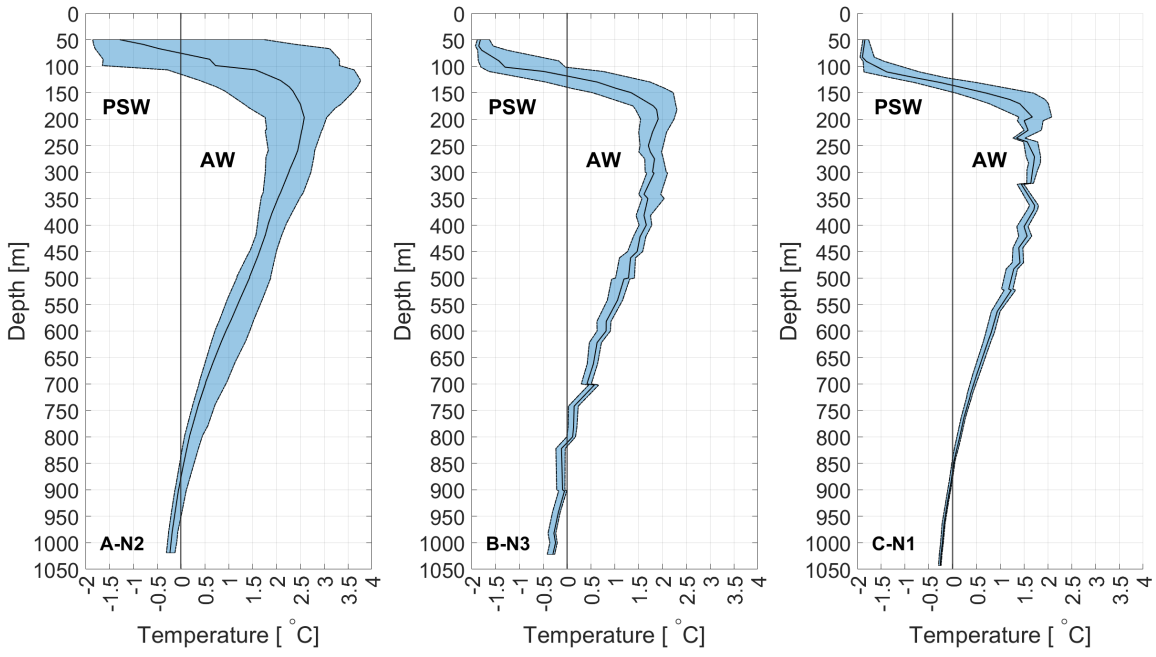

Figure 21: Temperature profile showing the mean profile (black line) throughout the measuring period from the A-N2 mooring (left), the B-N2 mooring (middle), and the C-N1 mooring (right). The blue shaded area shows the variability with the minimum and maximum daily mean temperatures as the edges.

The mean temperature of the AWL defined by temperatures above 0 °C and the mean temperature of the AWL between 300 and 700 m from the three moorings are given in Table 4.

The mean temperature of the AWL defined by temperatures above 0 °C was highest (1.54 °C) at the A-N2 mooring and lowest (1.13 °C) at the C-N1 mooring. Whereas the mean temperature of the AWL between 300 m and 700 m differed from the mean temperatures calculated from the AWL defined by temperatures above 0 °C. For the mean temperatures of the AWL between 300 m and 700 m, the mean temperature was also highest (1.46 °C) at the A-N2 mooring. Whereas the mean temperature was lowest (1.26 °C) at the B-N3 mooring, but very similar to the mean temperature at the C-N1 mooring (1.27 °C). The mean temperature of the AWL defined as temperatures above zero was at the A-N2 higher (by 0.08 °C) than of the AWL between 300 m and 700 m. At both the B-N3 and C-N1 moorings the mean temperatures of the AWL were higher between 300 m and 700 m, 1.26 °C and 1.27 °C compared to the AWL with temperatures above zero, 1.23 °C and 1.13 °C, respectively.

Table 4: Mean temperature of the AW defined by temperature above 0 °C, and the AW between 300 and 700 m at each mooring.

	Mean temperature of AW (T > 0 °C)	**Mean temperature of AW (300 - 700 m)**
A-N2	1.54	1.46
B-N3	1.23	1.26
C-N1	1.13	1.27

4.2 Observations from the Amundsen and Nansen Basins

Six profiles of temperature, salinity, and calculated sound speed near the CAATEX section (Figure 22) from the SCICEX 1995 and Polarstern 2015 cruises are presented in Figure 23. These six profiles are two profiles from each of the Amundsen Basin, the Nansen-Gakkel Ridge, and the Nansen Basin, and are among the observations that have been used to calculate the mean temperatures of the AWL presented in Table 5.

The temperature and salinity profiles from the SCICEX 1995 are presented in the upper panel of Figure 23. The temperatures were constant below $-$ 1.80 ° C between 30 m and about 100 m in the profiles from both the Amundsen and Nansen Basins, whereas the temperature was constant down to 120 m around the Nansen-Gakkel Ridge. The upper boundary of the AWL was shallowest at about 150 m in the Amundsen Basin and the deepest of about 185 m near the Nansen-Gakkel Ridge. The AW core temperature was highest in the Nansen Basin with the maximum temperature of 2.10 ° C at 250 m. At the Nansen-Gakkel Ridge, the AW core temperature was slightly less at about 1.85 ° C. The AW core temperature was lowest in the Amundsen Basin at 1.40 ° C. All the profiles showed temperature inversions around the AW core, with the most distinguished inversions in the Amundsen Basin. The vertical extensions of the two inversions in the Amundsen Basin were about

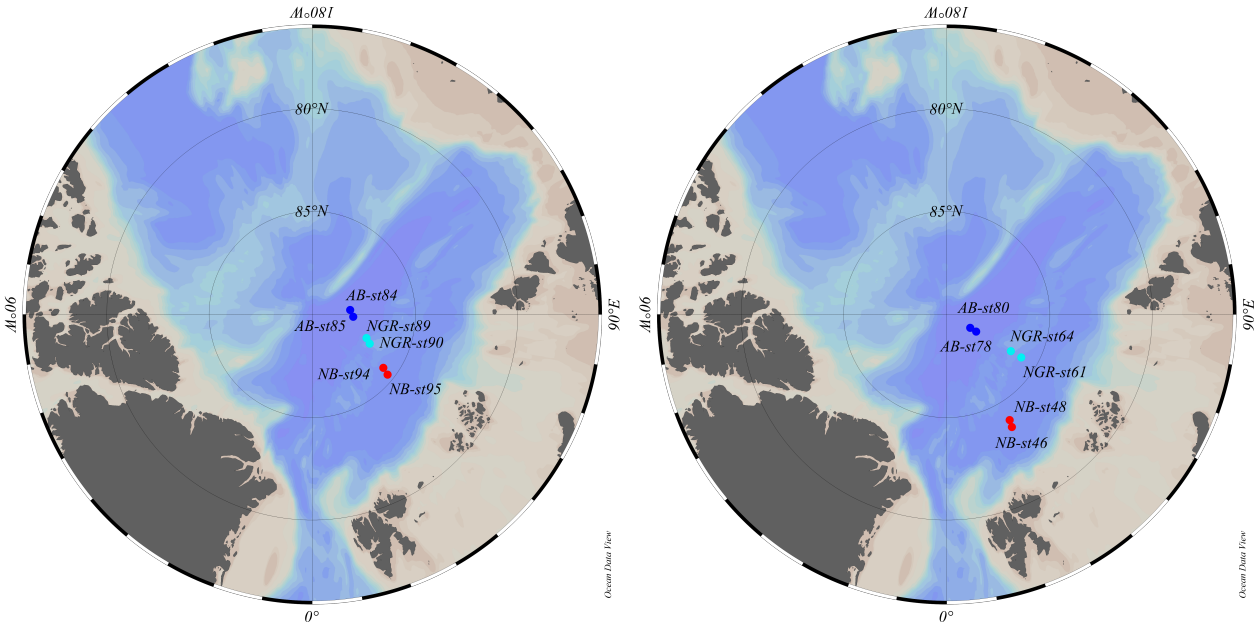

Figure 22: Position of the observations from the Amundsen Basin (blue), the Nansen-Gakkel Ridge (cyan), and the Nansen Basin (red) from the SCICEX 1995 (left) and the Polarstern 2015 (right) cruises. The labels show the corresponding profiles presented in Figure 23.

15 m and 60 m lying between 200 and 300 m. The temperature decreased about 0.20 ° C between 195 m and 210 m, and about 0.40 ° C between 220 m and 280 m. The lower boundary of the AWL was around 670 m in the Amundsen Basin, whereas the profiles did not cover the lower AWL boundary in the Nansen Basin and around the Nansen-Gakkel Ridge, indicating a lower AWL boundary deeper than 780 m.

The salinity profiles from the SCICEX 1995 cruise (Figure 23b) start also at about 30 m. The salinities between the areas at 30 m showed a relatively small range, 33.97 to 34.36. The profiles from the Amundsen Basin and the NB-st95 station in the Nansen Basin showed lower salinities in the upper 70 m of the profiles than the profiles from the Nansen-Gakkel Ridge. The salinity increased with depth from about 90 m in the Amundsen and Nansen Basins, but to about 140 m at the Nansen-Gakkel Ridge.

The sound speed between 30 m and 100 m were very similar between the areas (Figure 23c). The sound speed was about 1439.9 m s^{-1} at 30 m and 1440.8 m s^{-1} at 100 m. Below this, the sound speed increased down to about 200 m, whereas the sound speed in the Amundsen Basin was relatively stable at about 1559.5 m s^{-1} and in the Nansen Basin it was 1662.5 m s^{-1}. Two jumps in the sound speed of about 1 m s^{-1} can be seen at the corresponding depths of the temperature inversions seen in the profiles from Amundsen Basin.

The profiles from Polarstern 2015 covered the water column from the surface down to 800 m (lower panel Figure 23). Close to the surface, the temperature was variable between the

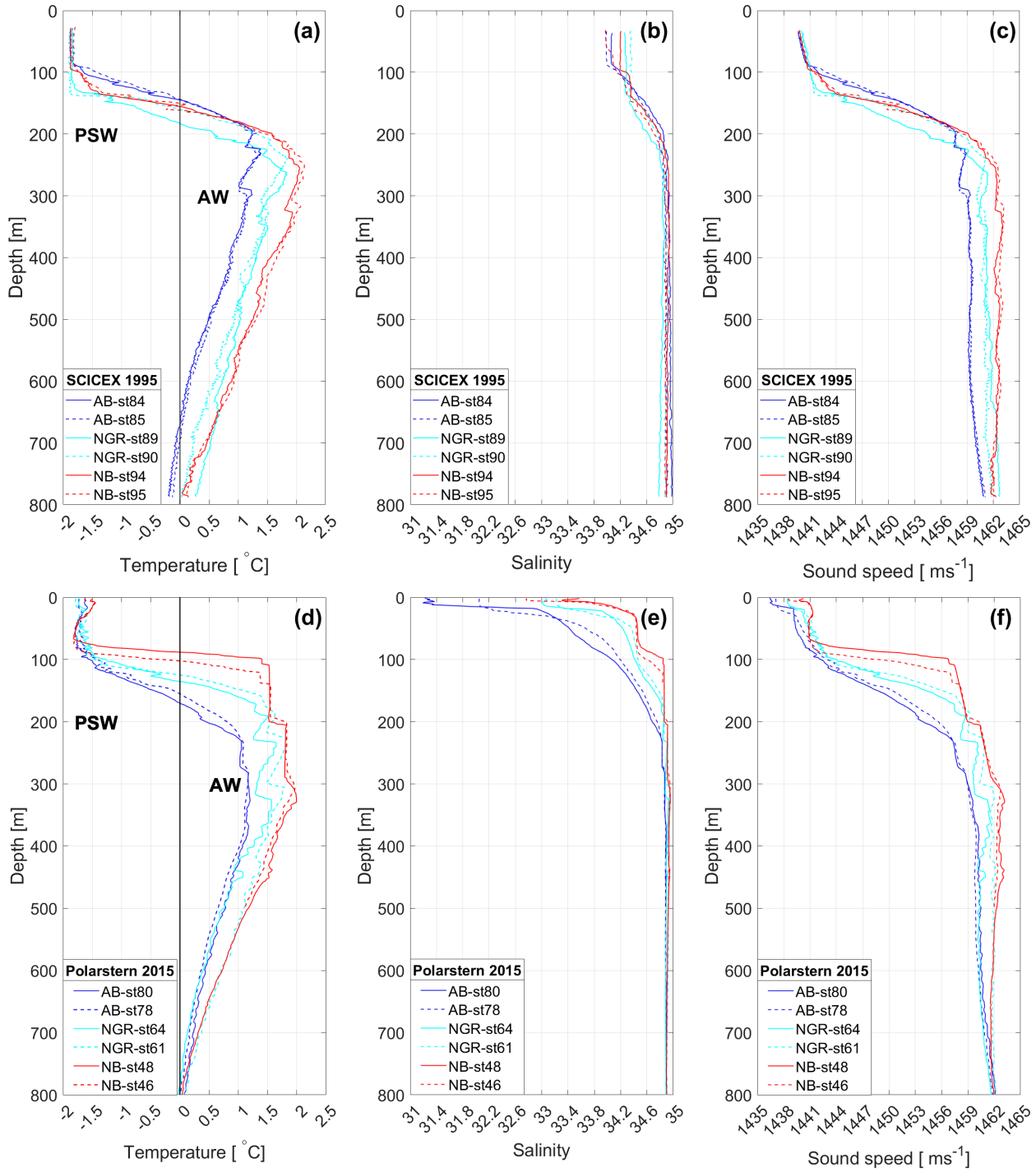

Figure 23: Temperature, salinity, and sound speed profiles from the Nansen Basin (red), the Nansen-Gakkel Ridge (cyan), and the Amundsen Basin (blue) from the SCICEX 1995 cruise in the upper panel and the Polarstern 2015 cruise in the lower panel.

locations, but they exhibit all near-surface temperature maximums (Figure 23d). At the stations from the Nansen Basin, the temperature was about − 1.5 °C close to the surface and decreased to − 1.82 °C at 65 m. The lowest temperature (− 1.78 °C) at the surface was around the Nansen-Gakkel Ridge. The upper boundary of the AWL differed clearly between the areas, where the boundary was between 90 m and 100 m in the Nansen Basin and between 160 m and 170 m in the Amundsen Basin. The temperature profiles from the Nansen Basin exhibit two thick ($\sim$ 100 m) layers with constant temperature of 1.53 °around 110 m to 200 m and 1.80 °C about 210 m to 290 m. Around the Nansen-Gakkel Ridge, layers of temperature inversions are more present and were in the same depth order of the layers as seen in the Nansen Basin. The most pronounced inversions were between 190 m to 220 m, where the temperature decreased by 0.26 °C, and between 240 m and 320 m with a decrease of 0.36 °C. In the Amundsen Basin, no strong temperature inversions were present. Two layers with a relatively constant temperature of 1.00 °C and 1.20 °C were present from 220 m to 275 m and from 280 m to 330 m, respectively.

The salinity between the surface and about 300 m showed a wide range between the basins (Figure 23e). The salinity profiles from the Amundsen Basin were freshest, especially close to the surface with salinities around 31.30 at the AB-at80 station and 32.05 at the AB-st78 station. At around 20 m depth, the salinity increased fast to 33.00 and continued to increase more steadily to about 34.80 at about 250 m.

A shallow layer (upper 20 m) of a sound speed minimum was seen near the surface in all regions, especially in the Amundsen Basin (Figure 23f). Below this, was a relatively stable layer of nearly constant sound speed of about 1441.0 m s^{-1} in the Nansen Basin and slightly lower of about 1440.0 m s^{-1} in the Amundsen Basin. The sound speed increased more rapidly in the Nansen Basin at about 80 m and 90 m. The sound speed near the Nansen-Gakkel Ridge increased more gradually between about 90 m and 200 m, and even more gradually in the Amundsen Basin.

Temperature inversions were also present in the profiles from the Le Commandant Charcot 2021 cruise. The transect covered by this cruise extended from the positions of where the CATEEX moorings were during the previous year (2019-2020) to the middle of the Amundsen Basin (Figure 24). The temperature profiles exhibited a spatial difference in the inversions seen in the depths around the AW core. The southernmost temperature profiles showed small inversions in both temperature (smaller than 0.1 °C) and vertical extent (less than 10 m). Moving northwards in the Nansen Basin the inversions and layers of constant temperature between the inversions increased in vertical extent. At the C-st5 station near the Nansen-Gakkel Ridge, the temperature was the highest among the profiles from this cruise. The profile exhibited a layer of higher temperature between 180 m and 350 m of about 2.4 °C, 0.35 °C higher than what was seen in the other profiles. Apart from the C-st5, the temperature around the depths of the AW core decreased gradually from

the Nansen Basin towards the Nansen-Gakkel Ridge into the Amundsen Basin. Where the temperatures around the AW core were about 2.05 °C, 1.70 °C, 1.35 °C in the Nansen Basin, the Nansen-Gakkel Ridge, and the Amundsen Basin, respectively. At the C-st3 and C-st4 stations at the Nansen-Gakkel Ridge, the temperature inversions had a vertical extent of about 50 m to 70 m, with a temperature difference of about 0.3 °C. The vertical extent of the inversions in the Amundsen Basin were comparable to the extent seen at the Nansen-Gakkel Ridge, but with a slightly smaller temperature difference of about 0.2 °C.

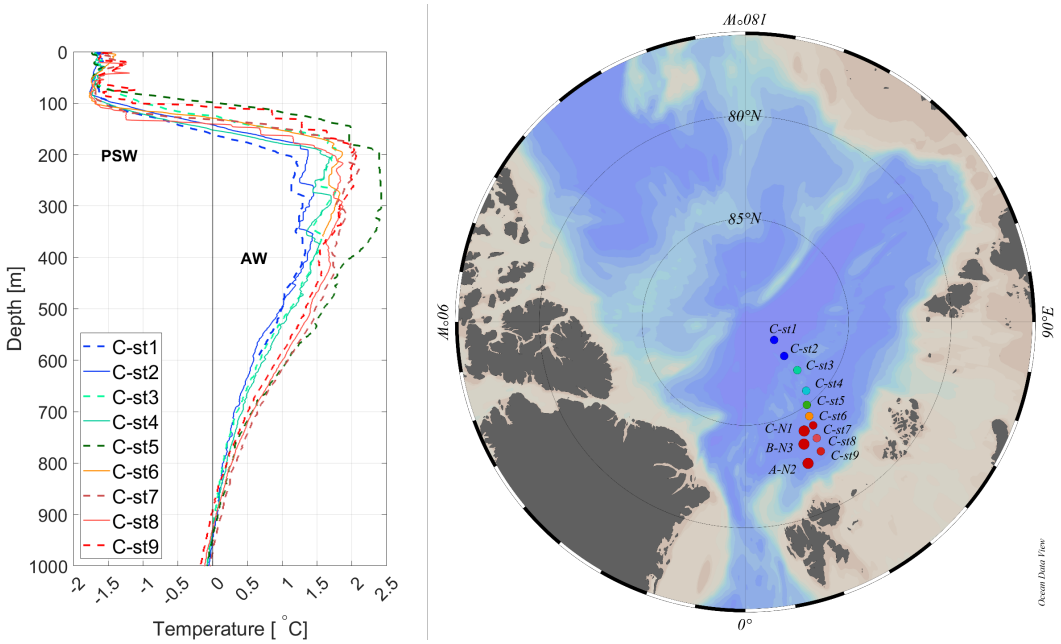

Figure 24: Left: temperature profiles from XBT casts conducted during the Le Commandant Charcot cruise in 2021, one year after the operating CAATEX moorings in the Nansen Basin. Right: map of the positions of the XBT profiles with labels, and positions of the CAATEX moorings.

4.3 Mean temperatures of the AWL near the CAATEX section in the Eurasian Basin

The mean temperatures of the AWL have been calculated from the supplementary cruise observations, including the presented profiles from the SCICEX 1995, Polarstern 2015, and Le Commandant Charcot 2021 cruises (Table 5). The cruise name and year are given in the left column, the mean temperatures of the AWL defined by temperatures above 0 °C are given in the middle column, and the mean temperatures of the AWL between 300 m and 700 m are given in the right column.

The mean temperatures of the AWL defined by temperatures above zero °C ranged between 0.77 °C and 1.00 °C. The mean temperature was 0.79 °C in 1995 and 1997. After this, the mean temperatures were slightly higher in 1998, 2000, and 2001. The mean temperatures from the SCICEX 2001 and ODEN 2001 cruises were 0.94 °C and 0.92 °C, respectively. In 2003 and 2005 the mean temperatures were somewhat lower compared to in the late 90s

Table 5: Mean temperature of the AW defined by temperature above 0 °C and the mean temperature of AW between 300 and 700 m from each cruise.

	AWL (T > 0 °C)	AWL (300 - 700 m)
SCICEX (1995)	0.79	0.87
SCICEX (1997)	0.79	0.76
SCICEX (1998)	0.90	0.88
SCICEX (2000)	0.93	1.00
SCICEX (2001)	0.94	1.00
ODEN (2001)	0.92	0.92
SCICEX (2003)	0.84	0.92
ODEN (2005)	0.77	0.75
Polarstern (2011)	0.96	0.97
Polarstern (2012)	0.94	0.97
Polarstern (2015)	0.79	0.84
Le Commandant Charcot (2021)	1.00	1.19

and early 00s. In 2011 the mean temperature increased to 0.96 °C, before decreasing to 0.79 °C in 2015. The highest mean temperature of 1.00 °C was in 2021.

The mean temperature of the AWL between 300 and 700 m ranged between 0.75 °C and 1.19 °C. The mean temperature was 0.87 °C in 1995 and decreased to 0.76 °C in 1997. After this, it increased to 1.00 °C in 2000. The SCICEX 2001 and ODEN 2001 had the mean temperatures of 1.00 °C and 0.92 °C, respectively. The mean temperature decreased to 0.75 °C in 2005. In 2011 and 2012, the mean temperatures were 0.97 °C, and decreased to 0.84 °C in 2015. The highest mean temperature of the AWL between 300 m and 700 m was 1.19 °C in 2021.

The two ways of calculating the mean temperature of the AWL from the selected cruises resulted in slightly different estimates. The difference between the two methods was mainly lower than 0.1 °C for most cruises. Moreover, the two methods do not consistently over- or underestimate the mean temperatures compared to each other. But the tendencies of increasing and decreasing mean temperatures throughout the timeline are quite consistent in both methods. The largest difference between the two methods was 0.19 °C from the Le Commandant Charcot 2021 observations. And the mean temperature of 0.92 °C from the two methods was equal in 2001.

4.4 Sound speed

Sound speed profiles in the upper 200 m

This section will give a brief and novel analysis of the depth of the sound speed channel near the surface at the three moorings. The sound speed has been calculated using the Del Grosso equation (Eq. 2) with the temperature and salinity measurements from six depths between 50 m and about 175 m at the A-N2, B-N3, and C-N1 mooring. The monthly mean sound speed profiles at these depths and the corresponding monthly mean temperature and salinity profiles are presented in Figure 25. The associated temperature and salinity profiles will only be briefly commented on as these observations have been presented earlier.

The vertical structure of the monthly mean sound speed profiles varied between the months at the A-N2 mooring (Figure 25a.1). All profiles showed an increasing sound speed between 50 m and the next depth level at 67 m, indicating a sound speed gradient between 50 m to 60 m, thus a shallow channel. The deepest channel was in July where the monthly mean sound speed at 50 m was 1440.5 m s^{-1} and only increased to 1442 m s^{-1} at 67 m. The monthly mean profiles from September, October, April, May, and June showed also a sound speed near 1440 m s^{-1} at 50 m, but the sound speed increased more down to the next depth level of 67 m compared to in July. The remaining months, November, December, January, February, and March had sound speeds ranging between 1443 m s^{-1} to 1449 m s^{-1} at 50 m. Below this, all sound speed profiles increase with depth. The greatest difference was between the profiles from July and March, especially at 67 m and 87 m where the difference was about 15 m s^{-1} between these two months.

The monthly mean temperature profiles between September 2019 and July 2020 showed increasing temperature with depth (Figure 25a.2). There is a clear maximum and minimum monthly mean temperature profiles at the A-N2 mooring occurring in March and July, respectively. The maximum monthly mean temperature profile in March lies within the AWL between 50 m and 147 m (right of the black zero-degree isotherm line). Whereas the minimum monthly mean temperature profile in July lies in the PSL from $-$ 1.78 °C at 50 m and crosses the zero-degree isotherm at about 95 m into the AWL. The temperature continues to increase to 1.93 °C at 147 m. All other monthly mean temperature profiles lies between the profiles in March and July. The monthly mean salinity profiles showed increasing salinities with depth (Figure 25a.3). The maximum monthly mean salinity profile was also in March at all depths, except at 147 m where the monthly mean salinity in March was slightly less (by 0.01) than in November. The minimum monthly mean salinity profile was also in July at all depths, except at 50 m where the monthly mean salinity was slightly higher (by 0.03) than in April.

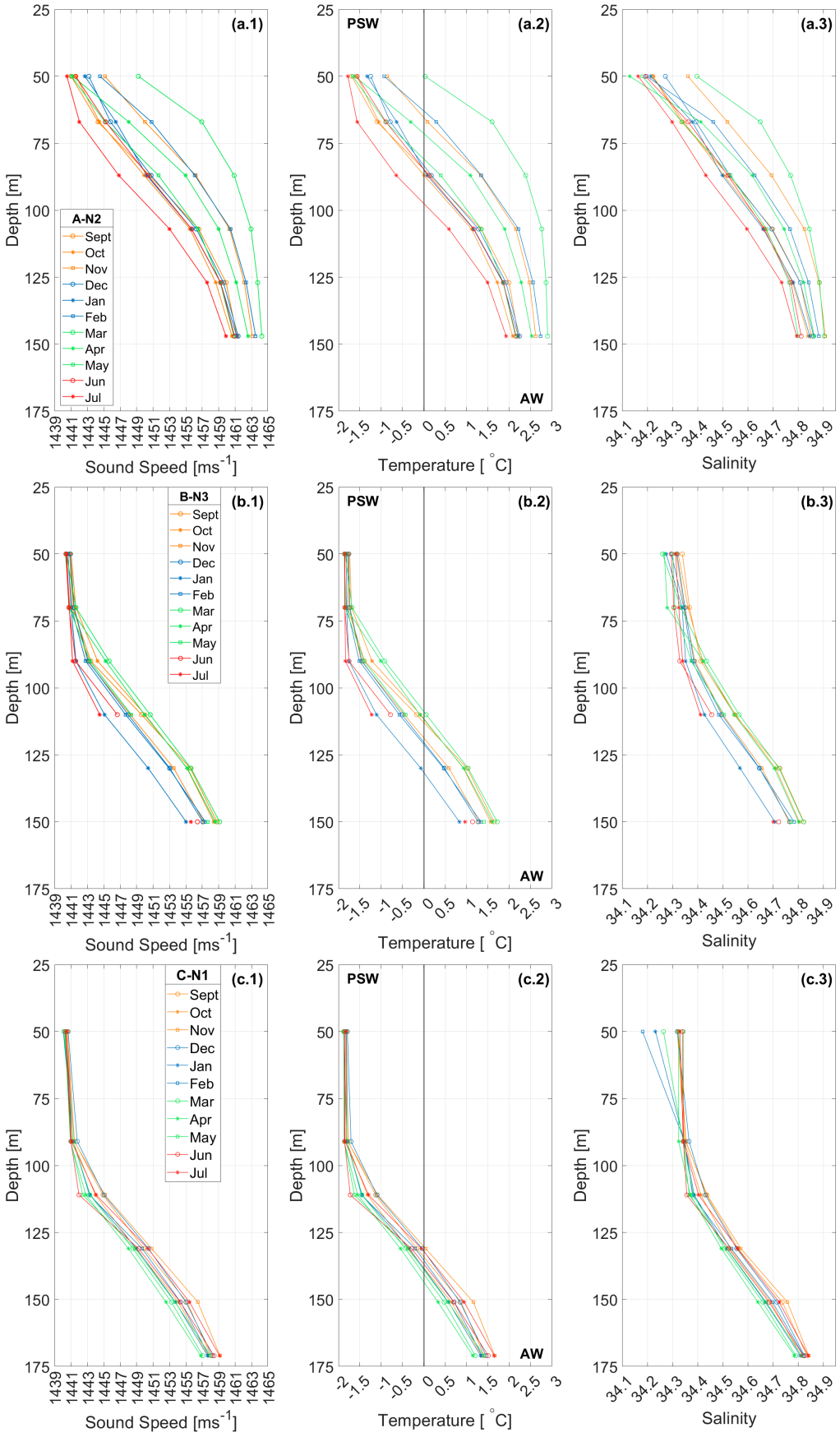

Figure 25: Profiles of calculated sound speed (left panels), temperature (middle panels), and salinity (right panels) at mooring A-N2 (a), B-N3 (b), and C-N1 (c).

At the B-N3 mooring, the monthly mean sound speed profiles from all months showed a very even channel between 50 m and 70 m (Figure 25b.1). Below 70 m, the monthly mean sound speed profiles varied more between the months. In January, June, and July, the sound speed profiles showed the least increase with depth, and the surface channel extends down to 90 m. For the other months, the sound speed increased faster. Especially during spring when the sound speed increased by about 5 m s^{-1} between 70 m and 90 m. Between 110 m and 130 m, the sound speed increased about 5 m s^{-1} for all months, but the sound speed was generally lower in winter and summer compared to autumn and spring. Between 130 m and 150 m, the sound speed increased about 4 m s^{-1} for all months, except in January where it increased by 5 m s^{-1}(data missing between April and July at 130 m).

The monthly mean temperature profiles showed small temperature variations between the depths of 50 m and 70 m through the months (Figure 25b.2). The only monthly mean profile showing increasing temperature from 50 m down to 70 m was in March, where the monthly mean temperature increased from $-$ 1.84 °C at 50 m to $-$ 1.68 °C at 70 m. The monthly mean temperature profile from July showed especially little variation with depth down to 90 m, whereas the other monthly mean temperature profiles showed increasing temperatures with depth from 70 m down to 150 m. There were no clear monthly mean profiles showing maximum and minimum temperatures, but the monthly mean temperature in autumn (orange lines) and spring (green lines) showed a greater increase with depth compared to the profiles in winter (blue lines) and summer (red lines). The monthly mean salinity at 50 m ranged between 34.26 and 34.34 in March and September, respectively (Figure 25b.3). The salinity stayed constant down to 70 m in April till July, whereas the salinity increased slightly for the other months, especially in January, February, and March (by 0.06). At the next depth level, 90 m, the salinity continued to increase for all months, with the greatest increase between 70 m and 90 m during spring (green lines). Below 90 m, the salinity increased gradually with depth and the monthly mean profiles showed a similar shape. However, the sharpest gradient in the monthly mean salinity profiles was seen in autumn (orange lines) and spring (green lines). Whereas the salinity profiles in winter (blue lines) and summer (red lines) were not as sharp.

The vertical structure of the monthly mean sound speed profiles from the C-N1 mooring was relatively stable throughout the year (Figure 25c.1), especially at 50 m and 91 m. The monthly mean sound speed at 50 m had a minimum of 1440.1 m s^{-1} in February and a maximum of 1440.7 m s^{-1} in December. The monthly mean sound speeds increased slightly down to 91 m. At 91 m the minimum and maximum monthly sound speeds were 1440.9 m s^{-1} and 1441.8 m s^{-1} in April and December, respectively, showing a small variation between the months. Below this, at 111 m the monthly mean sound speed differed somewhat more between the months. The minimum monthly mean sound speed at 111 m of 1442.0 m s^{-1} was in June, showing a relatively small increase between 50 m to 111 m. Whereas the maximum monthly mean sound speed of 1445.1 m s^{-1} at 111 m was in November. Below this, the monthly mean sound speed increased by about 6 m s^{-1} be-

tween each depth level.

The monthly mean temperature profile showed a stable temperature between 50 m and 91 m, especially in September, April, May, June, and July (Figure 25c.2). In December there is a slight increase of 0.1 ° C from 50 m to 91 m. At 111 m, the monthly mean temperature in June was − 1.72 °C, showing a relatively deep layer of low temperatures. Whereas the maximum monthly mean temperature of − 1.08 °C at 111 m was in November. Below this, the monthly mean temperature increased by about 1 °C between each depth level. The monthly mean salinity at 50 m showed a decrease in salinity in January, February, and March, while the salinity was above 34.32 and very similar for all other months (Figure 25c.3). At 87 m, the monthly mean salinity showed a small difference between the months. Whereas the monthly mean salinities differed between the months by about 0.1 at 111 m and below.

A comparison between the three moorings showed a large difference in the monthly mean sound speeds. The monthly mean sound speed profiles from the A-N2 mooring showed a generally higher speed than at the B-N3 and C-N1 moorings. The difference was especially large at 50 m. Additionally, the variation seen throughout the months was larger at the A-N2 mooring where the sound speed gradient was smaller in July and larger in March. Whereas the sound speed profiles from the C-N1 mooring were more stable throughout the year, especially in the layer between 50 m and 91 m.

The maximum and minimum daily mean temperature, salinity, and sound speed with the corresponding date of occurrence measured at each are displayed in Table 6. The table summarizes the main findings of the temperature, salinity, and sound speed variability in the upper 50 m to about 175 m.

Table 6: Maximum and minimum daily mean temperature (T), salinity (S), and calculated sound speed (C), with corresponding date of occurrence.

A-N2												
	Maximum daily mean						**Minimum**					
Depth	$T\ [°C]$	$Date$	S	$Date$	$C\ [ms^{-1}]$	$Date$	$T\ [°C]$	$Date$	S	$Date$	$C\ [ms^{-1}]$	$Date$
50 m	1.75	04.03.20	34.69	22.11.19	1457.3	04.03.20	−1.85	09.05.20	33.95	01.02.20	1440.2	24.05.20
67 m	3.12	24.06.20	34.89	24.06.20	1464.0	24.06.20	−1.80	26.05.20	34.14	29.05.20	1440.7	29.05.20
87 m	3.32	24.06.20	34.92	24.06.20	1465.2	24.06.20	−1.63	31.05.20	34.26	30.05.20	1442.0	30.05.20
107 m	3.63	24.06.20	34.97	24.06.20	1466.9	24.06.20	−0.28	31.05.20	34.45	03.06.20	1448.9	03.06.20
127 m	3.77	24.06.20	35.00	24.06.20	1467.9	24.06.20	0.39	30.05.20	34.59	30.05.20	1452.5	30.05.20
147 m	3.63	24.06.20	34.97	24.06.20	1467.6	24.06.20	0.92	08.07.20	34.57	29.05.20	1455.3	08.07.20
B-N3												
50 m	−1.62	14.10.19	34.35	15.09.19	1441.6	14.10.19	−1.88	30.03.20	34.19	23.01.20	1440.3	14.04.20
70 m	−1.25	18.03.20	34.38	18.03.20	1443.7	18.03.20	−1.87	29.05.20	34.26	09.04.20	1440.6	10.04.20
90 m	−0.17	21.03.20	34.52	21.03.20	1449.2	21.03.20	−1.86	21.07.20	34.32	27.05.20	1441.1	21.07.20
110 m	0.76	20.03.20	34.66	20.03.20	1454.0	20.03.20	−1.64	21.07.20	34.37	22.07.20	1442.5	21.07.20
130 m	1.75	18.03.20	34.82	18.03.20	1458.9	18.03.20	−0.44	18.01.20	34.53	17.01.20	1448.7	18.01.20
150 m	2.23	20.03.20	34.89	20.03.20	1461.4	20.03.20	0.53	17.01.20	34.66	18.01.20	1453.6	17.01.20
C-N1												
50 m	−1.77	11.12.19	34.35	05.05.20	1440.7	11.12.19	−1.88	05.04.20	34.06	23.01.20	1439.9	24.01.20
91 m	−1.44	11.12.19	34.41	11.12.19	1443.1	11.12.19	−1.88	09.04.20	34.30	05.04.20	1440.9	06.04.20
111 m	−0.69	12.09.19	34.49	12.09.19	1447.0	12.09.19	−1.86	02.06.20	34.34	02.06.20	1441.3	02.06.20
131 m	0.50	24.11.19	34.63	24.11.19	1453.0	24.11.19	−0.80	28.03.20	34.46	29.03.20	1446.8	28.03.20
151 m	1.70	24.11.19	34.82	24.11.19	1459.0	24.11.19	0.08	29.03.20	34.59	29.03.20	1451.3	29.03.20
171 m	2.01	24.11.19	34.88	24.11.19	1460.7	24.11.19	0.77	29.03.20	34.71	29.03.20	1455.0	29.03.20

Effect of salinity below 200 m

The effect of salinity on calculated sound speed has been investigated by computing three sound speed profiles from one temperature profile and using three different salinity profiles (Figure 26). The temperature and one of the salinity profiles are from an observation taken by ITP95 (shown as black lines in the figure) and one profile is based on the commonly used and assumed salinity value of 35 (red line) and is constant with depth. The profiles from ITP95 were chosen based on the close location to the northernmost mooring C-N1.

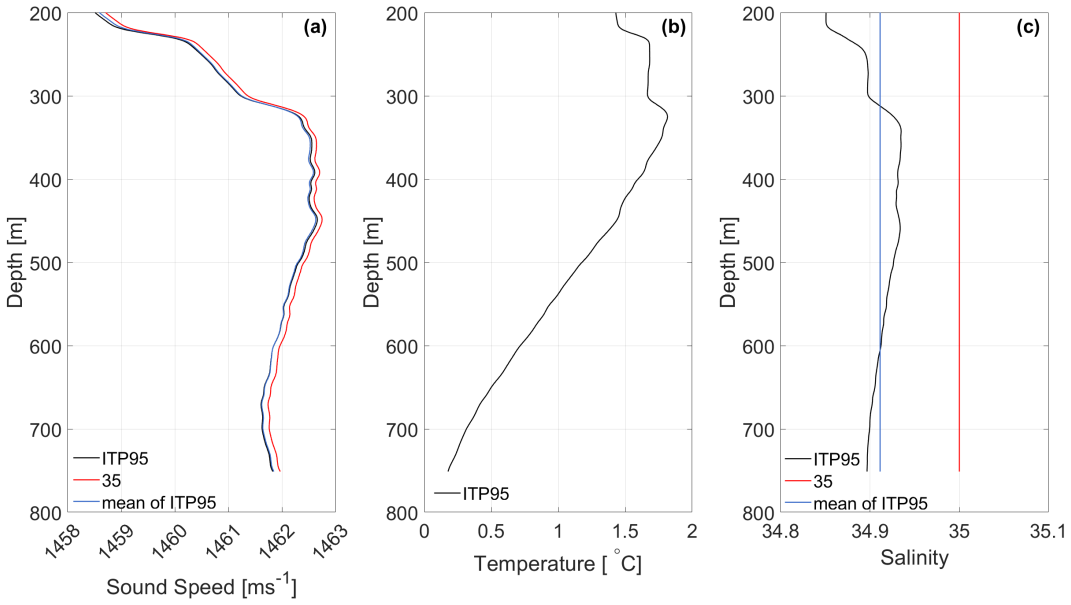

Figure 26: Left panel displays three sound speed profiles using the temperature profile in the middle panel and the three different salinity profiles in the right panel. One salinity profile taken by ITP95 (black line), one constant profile is the mean salinity of the salinity profile from ITP95 (blue), and one constant profile of 35 (red line). Right panel shows the corresponding sound speed profiles following the colors of the salinity profiles.

The difference between the sound speed profiles calculated from the mean salinity of the ITP95 salinity profile and the assumed value of 35 was about 0.12 m s^{-1} throughout the profile with the corresponding salinity difference of 0.09. The ITP95 salinity profile and the mean salinity of the ITP95 salinity profile (S=34.91) are equal at 312 m and 605 m, thus was the sound speed equal at these depths too. Whereas the largest overestimate and underestimate of 0.08 m s^{-1} and 0.03 m s^{-1} were found at about 208 m and 350 m, respectively, between the ITP95 profile and the mean salinity of the ITP95 profile.

The largest difference between the sound speed profile from ITP95 and the sound speed profile with the assumed salinity of 35 was in the upper 10 meters of the profile. The sound speed difference was 0.2 m s^{-1}, with the corresponding salinity difference of 0.15. In the upper 10 meters of the profiles, the difference between the two constant profiles (one being the mean salinity of the salinity profile from ITP95 (S = 34.91, blue line), and the other

being the assumed value of S = 35, red line). The minimum salinity difference between the measured salinity profile and the assumed profile (35) was 0.07 at 343 m, with the corresponding difference in sound speed of 0.09 m s^{-1}.

5 Discussion

This section will revisit the objectives stated in Section 1. How were the vertical structure and variability of the PSL and AWL at the three CAATEX moorings in the Nansen Basin between September 2019 and July 2020? What are the observed mean temperatures of the AWL from selected cruises between 1995 and 2021? What is the effect of salinity on sound speed in the central Eurasian Basin?

5.1 The hydrographic conditions at the CAATEX moorings in the Nansen Basin

Starting with the main findings at the upper part of the water column between 50 m and 175 m at the moorings in the Nansen Basin. Here, it was clear that the temperature and salinity, as well as the current data, displayed larger variability at the A-N2 mooring compared to the B-N3 and C-N1 moorings. The episodes occurring at the three mooring sites will first be addressed.

At the A-N2 mooring, the episodes showed AW was present high up in the water column (50 m) at the end of November, the beginning of March, and at the end of June at the A-N2 mooring (Figure 10). The increased pressure revealed that the A-N2 mooring was affected by downward movements during the episodes at the end of November and June (Figure 12). The downward movements seemed to be associated with increased current speed. But comparing the temperature further down (e.g. 87 m) before and after the pull-down, showed that there was still a temperature increase during these two episodes at the A-N2 mooring (Figure 10a). The correlation coefficient of 0.35 between the pressure and temperature was low, but the peaks at the end of November and at the end of June fitted well. Thus, the larger temperature variability at the A-N2 mooring measured by the SBE37-SMP deployed at 50 m was caused by increased current speed together with a downward movement of the mooring at the end of November and June. The episode occurring around the beginning of March was not caused by a vertical movement of the mooring, but the episode corresponded also well with the increasing current speed (Figure 12). The correlation coefficient (R = 0.50) between the temperature and current speed is somewhat higher than between the temperature and the pressure but is considered moderate. The correlation does not necessarily explain the reason for the change but may give an indication of the relationship between the variables. However, the maximum daily mean temperature of 1.75 °C was found at 50 m at the beginning of March.

The daily mean ice draft was looked into to see if any change could be seen in the ice cover above the A-N2 mooring (black arrows in Figure 19a). A limitation here is that the daily mean ice draft measurements are probably not resolved fine enough to display this. Moreover, the upper most temperature measurement at 50 m is quite far down in the water column and the lack of measurements above this makes it hard to draw any conclusion to

whether the sea ice could be affected. However, it displayed the presence of the ice cover above the moorings and its general trend over the year. The ice draft did not differ much from the typical seasonal cycle of the sea ice. The rapidly changing thickness of the ice draft was probably due to the moving sea ice over the mooring with variable thickness. The missing ice draft data was likely caused by the movement of the mooring at these times. Whereas the increased current speeds during autumn may indicate a stronger coupling between the atmosphere-ice-ocean when the ice draft was thinnest.

At the B-N3 mooring (Figure 13), a more stable temperature was found at 50 m compared to the temperature variability seen at 90 m and below. The pressure data (Figure 15) showed that the instrument deployed at 50 m lied closer to 60 m. This instrument depth will for consistency be referred to as 50 m. Apart from that, the mooring was steady with little vertical movement during the year (Figure 15). The correlation coefficient of 0.36 between the pressure and the temperature was low as excepted, as the small vertical movement was in a layer of small vertical temperature gradients. Additionally, the temperature over the year was relatively stable. The current data near the temperature measurement at 50 m showed generally weak currents throughout the year. The current speed and temperature at 50 m and above were lower and more stable during winter and spring. The correlation coefficient of 0.36 was low and the variabilities were independent. The higher current speeds (> 10 cm s^{-1}) between 10 m and 20 m, during autumn, were likely due to a thinner and more mobile ice cover (Figure 14). Whereas, the current speed was generally around 6 cm s^{-1} between 35 m and 50 m during autumn and at the end of June. This may be the cause of the slightly higher temperatures at 50 m during autumn with wind-induced mixing of heat down from the solar heating at the surface or by advection as the temperature below varied at the same time (Figure 13).

The episodes occurring at the B-N3 and C-N1 moorings (black arrows in Figure 13 and 16) showed larger variability further down in the water column. The current measurements were located higher up in the water column than the depths of the temperature variability, thus limiting the investigation of a possible dominant current direction or change during these episodes. However, the correlation between the temperature and pressure at 50 m at the C-N1 was 0.75 which is considered strong. The pressure data showed only a movement of about 1 m throughout the year, and it seems that the strong correlation coefficient was more due to the fitting trend (Figure 18).

The upper and lower boundary of the AWL varied throughout the year, but the discrete depths of the instruments mounted on the mooring give only an approximate depth of these boundaries and also the AW core. The depth of the upper boundary of the AWL was mainly found at 87 m and above, but the discrete depths of the instruments mounted on the mooring make this only an approximate depth. However, it shows that the upper boundary of the AWL was shallow between September 2019 and July 2020 at the south-

ernmost mooring, A-N2. Thus, the PSL was relatively thin, but the lack of measurements above 50 m limits the investigation of possible effects of the high temperatures near the surface, especially during the episodes. It is possible that the position of the A-N2 mooring is more influenced by the AW inflow through the Fram Strait. The position of the A-N2 mooring was located east/north-east of the Yermack Plateau. The knowledge about the complex AW circulation north of Svalbard are still limited and the location of where the Yermack Branch and the Svalbard Branch merge is still unknown (Renner et al., 2018; Athanase et al., 2021). A model study of the AW circulation north of Svalbard by Athanase et al. (2021) suggested an outer pathway of the Yermack Branch following the deeper topography around the Yermack Plateau. The current direction during the episodes at the A-N2 mooring when the temperature increased at 50 m. This is consistent with the southward current speeds at the northern end of the Yermack Plateau showing that the Yermack Branch curls around the plateau (Meyer et al. (2017)). Since the current direction at the A-N2 mooring was highly variable throughout the time series it indicates no prevailing current direction and that the increasing current speed and temperature are not due to variability of a specific current present at this location during the time series. However, the episodes could have been caused by a meandering/displacement of the Yermack Branch with increased current speed transporting higher AW temperatures or to advection of mesoscale features from the branch.

At the B-N3 mooring, the upper boundary of the AWL was between about 110 m and 130 m throughout the year (Figure 13). Hence, the PSL was thicker and relatively stable at the B-N3.

At the C-N1 mooring, the upper boundary of the AWL was at about 130 m throughout the year (Figure 16). This shows that the thickness of the PSL increased further north, and was most stable at the northernmost mooring, C-N1.

Moving down in the water column with the focus on the interleaving structures seen at the B-N3 and C-N1 moorings (Figure 20). The AWL exhibited different characteristics where the interleaving structures indicate AW with different mixing histories present at the B-N3 and C-N1 moorings. The lack of salinity measurements below 175 m as well as no current measurements limits further information about the source of the "warmer" and "colder" AW masses. However, the locations of the moorings are relatively near the inflow region from the Fram Strait. The alternation between higher and lower temperatures could be caused by "new" AW flowing north of Svalbard and "older" AW that have been circulating longer in the Nansen Basin. Previous studies have found similar structures around the Eurasian Basin (e.g. Carmack et al. 1997, 1995; Rudels et al. 2015; Anderson et al. 1994) where the formation area have been set to the northern part of the Kara Sea where the BSB and FSB meet and is advected with the current into the interior Nansen Basin, especially along the Nansen-Gakkel Ridge. The return flow along the Nansen-Gakkel Ridge was

proposed by Rudels et al. (1996), but due to the lack of an AW core this has been under discussion. From the Le Commandant Charcot 2021 cruise, a warmer AW core was seen at the Nansen-Gakkel Ridge on the Nansen Basin side and could indicate a return flow along the ridge. However, this was only one profile and should be supported by more observations.

Interleaving structures were not present at the A-N2 mooring location (Figure 20a). However, during the Le Commandant Charcot cruise one year later, interleavings with a vertical extent smaller than 10 m was found near the A-N2 location (Figure 24). The smaller vertical extent of the interleavings might be a reason why the inversions were not captured in the profiles from the A-N2 mooring. Also, it is possible that the location of the A-N2 mooring, is mostly dominated by possibly the Yermack Branch and not by AW with different mixing histories. The AW core temperatures at the A-N2 were higher than at the B-N3 and C-N1 moorings which are likely due to the closeness to the inflow through the Fram Strait.

Carmack et al. (1997) and Rudels et al. (2015) found the interleaving structures to be very similar in shape over time (similar over decades), indicating these to be persistent. The question is now will these layers of interleaving structures extending over 300 m affect the sound signal and how? From an oceanographer's point of view, the interleaving structures are more of an interest since it gives a clue about interior mixing processes. Whereas for acoustics, these are small-scale features and their effect on the sound speed signal depends on the frequencies of the sound signals. Higher frequencies are more sensitive to small gradients but travel over shorter distances. Whereas the lower frequencies are not as affected by the small gradients and can travel over longer distances. Whether the vertical extent of the interleaving layers has an effect on the sound signal and whether it will result in larger levels of travel time noise will have to be further investigated.

A more in-depth study of the AW core would benefit from salinity and current measurements at several depths. This could also give a better understanding of interleaving structures. Moreover, a CTD cast during deployment and recovery is important to be able to check for possible instrument drifts and also to evaluate the moorings' ability to resolve the structure of the water column. A further approach to investigate the sea ice can be through better time resolution of the ice draft and satellite images, as well as looking into atmospheric data (e.g. wind)

5.2 Comparison of the mean AWL temperature from observations and the Ocean Reanalysis Multi-Model-Mean

The mean temperatures of the AWL from selected cruises between 1995 and 2021 near the CAATEX section have been calculated in order to compare to Ocean Reanalyses Multi-

Model-Mean which is an ongoing work related to the CAATEX project (Langehaug et al. in progress). The two mean temperatures will be compared, and a short presentation of the timeline of these values will be compared to the Ocean Reanalyses Multi-Model-Mean.

The two most recent mean temperature measurements of the AWL were provided by the moorings in the Nansen Basin and from the transect conducted during the Le Commandant Charcot 2021 cruise (Table 4 and Table 5). The mean temperatures from the northernmost mooring, C-N1, in the Nansen Basin were higher compared to the mean temperatures from the Le Commandant Charcot 2021. Here, the difference between the point measurement provided by the mooring and the spatial "snapshot" provided by the cruise has to be taken into account. The spatial difference of higher temperatures in the Nansen Basin compared to in the Amundsen Basin was shown in Figure 23. This is consistent with knowledge about the temperature distribution between these two basins. The profiles from Polarstern 2015 cruise showed an increased difference in the vertical temperature structure between the Nansen Basin and Amundsen. A thicker layer of higher AW temperatures was present in the Nansen Basin compared to in Amundsen Basin in 2015 and it was found between 80 m and 90 m compared to about 150 m in 1995. This finding is only deduced from a few profiles, but it is consistent with observations of a shallower AWL in the Nansen Basin (Athanase et al. 2019). The question is then; can the changing temperature structure affect the comparison between the observed AWL defined by temperature above zero degrees and the AWL defined in the vertical layer between 300 m and 700 m?

The mean temperatures of the AWL defined by temperatures above 0 °C deviate from the mean temperatures of the AWL between 300 m and 700 m in all years except from the ODEN 2001 cruise. The mean temperatures calculated between 300 m and 700 m were generally slightly higher than the mean temperatures of the AWL defined by temperatures above 0 °C. The discrepancy between the two is likely to be caused by the cut-off of the lower temperatures near the upper and lower boundary of the AWL. The discrepancy between the two estimated mean AWL temperatures is also likely to be affected by the various depths of the AW core, as well as the depth of the upper and lower boundary of the AWL. This can be seen by the mean temperatures estimated from the moorings in the Nansen Basin. At the mooring locations, the greatest difference in the AWL temperature between the mooring measurements occurred above 300 m. The AW core was found above 300 m and the AW core temperature varied between the mooring locations. Moreover, the vertical extent of the AW core, that is how thick the layer of high temperatures around the AW core is, would affect the mean temperature value.

The selected cruise observations are mainly conducted during late summer and early autumn. Will this affect the yearly calculated mean temperature and are these mean temperatures be more representative as a seasonal mean temperature? A model and mooring observational study by Lique & Steele 2012 found that the amplitude of the AW temper-

ature seasonal cycle is only significant along the continental slope of the Nansen Basin, where the AW is primarily advected. This was also the main result of what was observed at the CAATEX moorings. The seasonal variability at the C-N1 mooring displayed a relatively small yearly variation (Figure 21c). Thus, the mean temperatures calculated from the selected cruises along CAATEX section starting from the C-N1 mooring in the central Eurasian Basin is a good representation of a yearly mean temperature.

Collecting observations of mean temperatures of the Arctic Ocean Layers along the CAATEX section from the Nansen Basin to the Beaufort Sea is an ongoing work. The goal is to establish a timeline of the mean temperatures of the PML, HL, and AWL. However, the timeline can be improved by collecting more data and utilizing different observational platforms. The seasonal cycle is likely to be more prominent in the PML and HL, and this would have to be accounted for when gathering data to calculate the mean temperature of these layers. Collecting data from various seasons from platforms like e.g. ITPs and ice camps and comparing seasonal mean temperatures can be a way of doing this.

The mean AWL temperatures from the cruise observations between 1995 and 2021 and the mean AWL (300 m - 700 m) from the Ocean Reanalysis Multi-Model-Mean are presented in Figure 27. It is found that Ocean Reanalysis Multi-Model-Mean represents well the observed mean temperature of the AWL along the CAATEX secton in the Eurasian Basin. The discrepancy between the two methods for the mean temperatures was relatively small and the temperature tendency seems to be captured by both methods. However, whether future changes in the AWL temperature will occur at specific depths (e.g. above 300 m or thicker layers of high temperatures) can alter the discrepancy between the two methods (e.g. as seen in 2021). Figure 27 and a further discussion will be a part of the publication in progress by Langehaug et al.

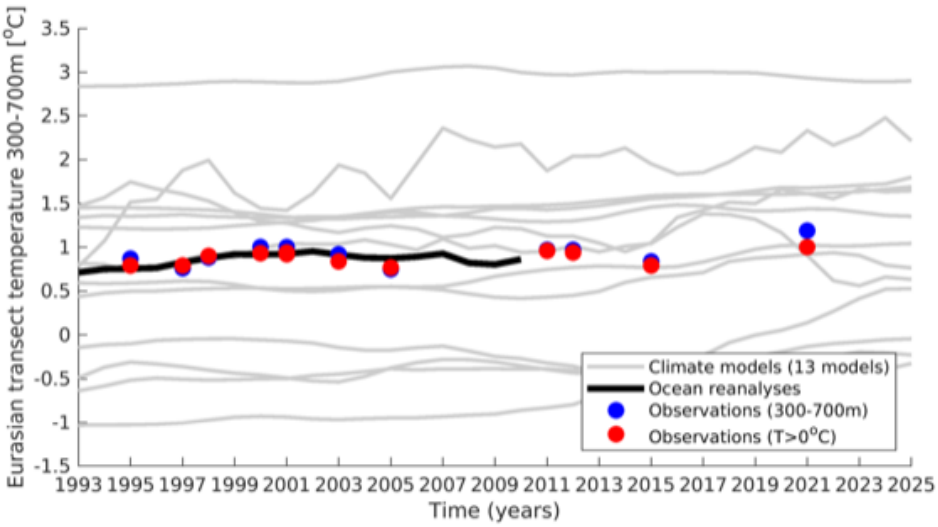

Figure 27: The ocean reanalyses (black curve) is compared with observations (red and blue circles) in the Eurasian part of the CAATEX section. Climate models (13 different models) are included (grey curves).

5.3 Sound speed

The monthly mean sound speed profiles from the three moorings A-N2, B-N3, and C-N1 in the Nansen Basin were presented in Figure 25. The vertical structure of the sound speed profiles gave an indication of the variability of the sound speed channel near the surface at the mooring locations. The monthly mean sound speed at the A-N2 mooring increased between the two uppermost instruments at 50 m and 67 m throughout the year. Thus, the sound speed gradient was located relatively high up in the water column and would cause a relatively shallow sound speed channel. However, since the uppermost measurement was at 50 m, it is not possible to determine the depth of the sound speed minimum since the temperature minimum would be located higher than 50 m. In July however, the monthly mean temperature at 50 m was -1.78 ° C with the corresponding sound speed of 1440.8 m s^{-1} and was near a sound speed minimum. The monthly mean temperature of 0.06 degrees C in March at 50 m at the A-N2 mooring with a corresponding monthly mean sound speed of 1449 m s^{-1}. Thus, the monthly mean sound speed in the AW ranged from 1449 m s^{-1} to 1464.5 m s^{-1} between 50 m and 147 m.

The larger sound channels at the B-N3 were during winter and summer (Figure 25b.1). However, the salinity near the surface is expected to decrease with summer ice melt. And despite the low temperatures during winter and summer, a sound speed minimum is therefore likely to be located under the ice during summer, causing a changing sound channel between winter and summer.

At the C-N1 mooring, the sound speed channel was very stable throughout the year between 50 m and 91 m, with a sound speed of about 1440 m s^{-1} and 1441 m s^{-1}, respectively. The slight increase between the depth levels are also affected by the pressure increase. The sound channel was especially deep in July, but again a possible salinity decrease near the surface could decrease the sound speed here. This seems to depend on the magnitude of the salinity decrease since the salinity decrease at 50 m seen in January, February, and March did not seem to affect the sound speed. The sound speed profiles followed the temperature profiles closely.

This novel approach gives an indication of the depth of the sound speed channel and presents mainly the spatial and temporal differences between the moorings, as well as insight into how temperature and salinity determine the sound speed. A more sophisticated analysis of how the hydrographic conditions altered the sound speed channel and the sound propagation should be conducted using an acoustic propagation model. The possibility of pressure variability (i.e. mooring movement), as seen at the A-N2 mooring (Figure 12), should be taken into account since this alters the depth of the acoustic sound source and receiver.

The effect of salinity on sound speed

The effect of salinity showed a small effect in the profiles ranging between 200 and about 800 m (Figure 26). The differences between the salinity profile and the profiles of constant salinity were small, as the sound speed profiles followed the temperature profile closely. To give the effect of salinity in numbers more intuitive, a salinity difference of 1 psu would imply a sound speed difference of 1.3 m s^{-1}. Based on observations of salinity in the depth range between 200 and 1000 m, in the deep basins away from the Arctic Circumpolar Boundary Current, it is generally shown a salinity range between 34.85 and 34.95 (Rudels et al. 2015). Thus, a salinity difference of 0.1 implies a small sound speed difference of 0.13 m s^{-1}. However, using the assumed value of 35 would cause an overestimation of the sound speed in the AWL in this area since the salinity of the presented data show lower values. This would lead to an accumulation of the sound signal (e.g. in an acoustic propagation model).

The acoustic propagation models are used to interpret the experimental observations of the sound transmitted between the source and receiver. Hence good input data are essential in the acoustic propagation models to be able to interpret the observations of the transmitted sound. Moreover, the different salinity ranges differ between regions, and choosing one value could again cause under- and overestimation over certain areas. Whereas the salinity range in the AWL is narrow, the effect of salinity would play a greater role where the salinity range would be larger (e.g. closer to the surface). It is therefore especially important to measure salinity higher up in the water column (i.e. PSW). The issue here is that the moorings did not cover much of the PML closer to the surface, hence data from other observational platforms are essential. Most cruises presented here were conducted in late summer and early autumn, missing the seasonal variability of the salinity in the PML. Data from e.g. Ice-Tethered Profilers or ice camps would be a better choice to study the water column closer to the surface and the sea ice over all seasons and over different regions, especially during winter and spring. Collecting available data during these seasons should therefore be the next step.

Moreover, a comment on the sound speed calculation of the Del Grosso equation range is better at low temperatures than the Chen and Millero. Since the Del Grosso is the best of the two for temperatures between 0 °C to 15 °C, it is however not known how good the Del Grosso equation is at negative temperatures. Another possible equation for sound speed would have been the Mackenzie equation which can be used for temperatures down to $-$ 2 °C (Mackenzie 1981). However, the Del Grosso and the Mackenzie equations have been found to agree well, and the simplified Mackenzie equation was used in the Fram Strait for simplicity (Dushaw et al. 2016). Thus, the application of both of these equations should be a suitable choice in the central Eurasian Basin.

Following the outcome of the salinity effect, the sound speed using a lower salinity con-

stant of 34.9 have been used to compute the sound speed profiles from the source mooring, C-N1 (Figure 28). It summarizes the sound speed profiles throughout the measurement period between September 2019 and July 2020, and will further be used in the acoustic propagation model. This will additionally provide a more detailed evaluation of the sound speed channel and its depth near the surface than the visual analysis presented above.

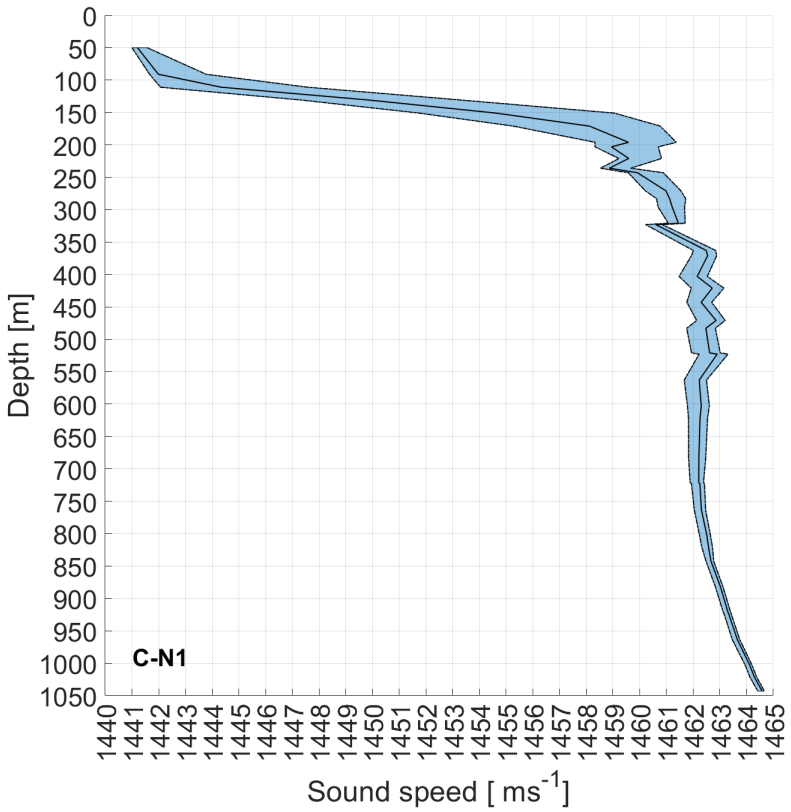

Figure 28: Vertical profiles of temperature (left panels), salinity (middle panels), and sound speed (right panels) at mooring A-N2 (a), B-N3 (b), and C-N1 (c).

6 Conclusion

- The temperature and salinity measured at the northernmost mooring, C-N1, were very stable between September 2019 and July 2020. Especially between 50 m and 91 m showed close to no variation during the year.
- The mean temperatures of the AWL from observations are well represented in the Ocean-Reanalysis Multi-Model-Mean along the CAATEX section in the Eurasian Basin.
- The effect of salinity on the sound speed was found to be small. The difference between a salinity profile and a salinity constant was very small. But in the layer between 200 m and 800 m, salinity profiles from cruise and ITP observations, are mainly below 35 in the central Eurasian Basin. Thus, should the assumed salinity value for sound speed calculation be lowered by 0.1, to 34.9. However, this does not apply near the surface where the salinity range is larger.

7 Further work

- Improve the mean temperature timeline of the AWL by collecting more data from cruises and other platforms along the CAATEX section. Follow the same procedure for the PML and HL with special attention to the seasonality of the observations.
- Extend the mean temperature timeline of CAATEX section covering the transect from the Nansen Basin to the SIO moorings in the Canadian Basin.
- Use the calculated sound speed profiles from the C-N1 mooring in an acoustic propagation model.
- Conduct a time series analysis on the mooring data.

References

Aagaard, K. & Carmack, E. C. (1989), 'The role of sea ice and other fresh water in the arctic circulation', *Journal of Geophysical Research: Oceans* **94**(C10), 14485–14498.
URL: *https://agupubs.onlinelibrary.wiley.com/doi/abs/10.1029/JC094iC10p14485*

Aagaard, K., Coachman, L. & Carmack, E. (1981), 'On the halocline of the arctic ocean', *Deep Sea Research Part A. Oceanographic Research Papers* **28**(6), 529–545.
URL: *https://www.sciencedirect.com/science/article/pii/0198014981901151*

Aksenov, Y., Ivanov, V. V., Nurser, A. J. G., Bacon, S., Polyakov, I. V., Coward, A. C., Naveira-Garabato, A. C. & Beszczynska-Moeller, A. (2011), 'The arctic circumpolar boundary current', *Journal of Geophysical Research: Oceans* **116**(C9).
URL: *https://agupubs.onlinelibrary.wiley.com/doi/abs/10.1029/2010JC006637*

Alkire, M. B., Polyakov, I., Rember, R., Pnyushkov, A., Ivanov, V. & Ashik, I. (2017), 'Combining physical and geochemical methods to investigate lower halocline water formation and modification along the Siberian continental slope', *Ocean Science* **13**(6), 983–995.
URL: *https://os.copernicus.org/articles/13/983/2017/*

AMAP (1998), 'Transport pathways and hydrographic conditions in the arctic seas', *In: AMAP Assessment Report: Arctic Pollution Issues, Arctic Monitoring and assessment Program, Oslo, chapter 3* p. 69.
URL: *https://www.amap.no/documents/download/89/inline*

AMAP (2017), 'Snow, water, ice and permafrost in the arctic (swipa)', *In: Arctic Monitoring and assessment Program (AMAP) , Oslo, chapter 2* .
URL: *https://www.amap.no/documents/download/2987/inline*

Anderson, L. G., Björk, G., Holby, O., Jones, E. P., Kattner, G., Koltermann, K. P., Liljeblad, B., Lindegren, R., Rudels, B. & Swift, J. (1994), 'Water masses and circulation in the eurasian basin: Results from the oden 91 expedition', *Journal of Geophysical Research: Oceans* **99**(C2), 3273–3283.
URL: *https://agupubs.onlinelibrary.wiley.com/doi/abs/10.1029/93JC02977*

Asbjørnsen, H., Årthun, M., Skagseth, & Eldevik, T. (2020), 'Mechanisms underlying recent arctic atlantification', *Geophysical Research Letters* **47**(15), e2020GL088036. e2020GL088036 10.1029/2020GL088036.
URL: *https://agupubs.onlinelibrary.wiley.com/doi/abs/10.1029/2020GL088036*

Athanase, M., Sennéchael, N., Garric, G., Koenig, Z., Boles, E. & Provost, C. (2019), 'New hydrographic measurements of the upper arctic western eurasian basin in 2017 reveal fresher mixed layer and shallower warm layer than 2005–2012 climatology', *Journal of*

Geophysical Research: Oceans **124**(2), 1091–1114.
URL: https://agupubs.onlinelibrary.wiley.com/doi/abs/10.1029/2018JC014701

Baumann, T. M., Polyakov, I. V., Pnyushkov, A. V., Rember, R., Ivanov, V. V., Alkire, M. B., Goszczko, I. & Carmack, E. C. (2018), 'On the seasonal cycles observed at the continental slope of the Eastern Eurasian basin of the Arctic Ocean', *Journal of Physical Oceanography* **48**(7), 1451–1470.
URL: https://doi.org/10.1175/JPO-D-17-0163.1

Bebieva, Y. & Timmermans, M.-L. (2016), 'An examination of double-diffusive processes in a mesoscale eddy in the arctic ocean', *Journal of Geophysical Research: Oceans* **121**(1), 457–475.
URL: https://agupubs.onlinelibrary.wiley.com/doi/abs/10.1002/2015JC011105

Bertosio, C., Provost, C., Sennechael, N., Artana, C., Athanase, M., Boles, E., Lellouche, J. & Garric, G. (2020), 'The western eurasian basin halocline in 2017: Insights from autonomous no measurements and the mercator physical system', *Journal of Geophysical Research: Oceans* **125**.
URL: https://doi.org/10.1029/2020JC016204

Beszczynska-Möller, A., Fahrbach, E., Schauer, U. & Hansen, E. (2012), 'Variability in Atlantic water temperature and transport at the entrance to the Arctic Ocean, 1997–2010', *ICES Journal of Marine Science* **69**(5), 852–863.
URL: https://doi.org/10.1093/icesjms/fss056

Bintanja, R., Graversen, R. & Hazeleger, W. (2011), 'Arctic winter warming amplified by the thermal inversion and consequent low infrared cooling to space', *Nature Geoscience* **4**, 758–761.
URL: https://doi.org/10.1038/ngeo1285

Bourgain, P. & Gascard, J. (2011), 'The arctic ocean halocline and its interannual variability from 1997 to 2008', *Deep-sea Research Part I-oceanographic Research Papers - DEEP-SEA RES PT I-OCEANOG RES* **58**, 745–756.
URL: https://doi.org/10.1016/j.dsr.2011.05.001

Carmack, E. C., Aagaard, K., Swift, J. H., Macdonald, R. W., McLaughlin, F. A., Jones, E. P., Perkin, R. G., Smith, J. N., Ellis, K. M. & Killiush, L. R. (1997), 'Changes in temperature and tracer distributions within the Arctic Ocean: Results from the 1994 Arctic Ocean section', *Deep-Sea Research Part II: Topical Studies in Oceanography* **44**(8), 1487–1493.
URL: https://doi.org/10.1016/S0967-0645(97)00056-8

Carmack, E. C., Macdonald, R. W., Perkin, R. G., McLaughlin, F. A. & Pearson, R. J. (1995), 'Evidence for warming of atlantic water in the southern canadian basin of the arctic ocean: Results from the larsen-93 expedition', *Geophysical Research Letters* **22**(9), 1061–1064.

URL: https://agupubs.onlinelibrary.wiley.com/doi/abs/10.1029/95GL00808

Carmack, E., Polyakov, I., Padman, L., Fer, I., Hunke, E., Hutchings, J., Jackson, J., Kelley, D., Kwok, R., Layton, C., Melling, H., Perovich, D., Persson, O., Ruddick, B., Timmermans, M.-L., Toole, J., Ross, T., Vavrus, S. & Winsor, P. (2015), 'Toward quantifying the increasing role of oceanic heat in sea ice loss in the new arctic', *Bulletin of the American Meteorological Society* **96**(12), 2079 – 2105.
URL: https://journals.ametsoc.org/view/journals/bams/96/12/bams-d-13-00177.1.xml

Coachman, L. K. & Barnes, C. A. (1962), 'Surface water in the eurasian basin of the arctic ocean', *Arctic* **15**(4), 251–278.
URL: http://www.jstor.org/stable/40507022

Darelius, E., Nilsen, F., Smedsrud, L. H. & Årthun, M. (2021), 'Formation and convection - a one dimensional model', *Geophysical Institute, University of Bergen, Scientific Report* .

Dmitrenko, I., Polyakov, I., Kirillov, S., Timokhov, L., Frolov, I., Sokolov, V., Simmons, H., Ivanov, V., Walsh, D. & Polyakov, I. (2008), 'Toward a warmer arctic ocean: Spreading of the early 21st century atlantic water warm anomaly along the eurasian basin margins', *Journal of Geophysical Research* **113**.
URL: https://doi.org/10.1029/2007JC004158

Dushaw, B. D., Sagen, H. & Beszczynska-Möller, A. (2016), 'Sound speed as a proxy variable to temperature in Fram Strait', *The Journal of the Acoustical Society of America* **140**(1), 622–630.
URL: http://dx.doi.org/10.1121/1.4959000

Falck, E., Kattner, G. & Budéus, G. (2005), 'Disappearance of pacific water in the northwestern fram strait', *Geophysical Research Letters* **32**(14).
URL: https://agupubs.onlinelibrary.wiley.com/doi/abs/10.1029/2005GL023400

Gavrilov, A. & Mikhalevsky, P. (2017), *Applications of Underwater Acoustics in Polar Environments*, pp. 917–922.
URL: https://www.researchgate.net/publication/316935662_Applications_of_Underwater_Acoustics_in_Polar_Environments

Hordoir, R., Skagseth, , Ingvaldsen, R. B., Sandø, A. B., Löptien, U., Dietze, H., Gierisch, A. M. U., Assmann, K. M., Lundesgaard, & Lind, S. (2022), 'Changes in arctic stratification and mixed layer depth cycle: A modeling analysis', *Journal of Geophysical Research: Oceans* **127**(1), e2021JC017270. e2021JC017270 2021JC017270.
URL: https://agupubs.onlinelibrary.wiley.com/doi/abs/10.1029/2021JC017270

Hu, X. & Myers, P. G. (2014), 'Changes to the canadian arctic archipelago sea ice and freshwater fluxes in the twenty-first century under the intergovernmental panel on climate

change a1b climate scenario', *Atmosphere-Ocean* **52**(4), 331–350.
URL: https://doi.org/10.1080/07055900.2014.942592

Ingvaldsen, R., Assmann, K., Primicerio, R., Fossheim, M., Polyakov, I. & Dolgov, A. (2021), 'Physical manifestations and ecological implications of arctic atlantification', *Nature Reviews Earth Environment* **2**.
URL: https://doi.org/10.1038/s43017-021-00228-x

Karcher, M. J., Gerdes, R., Kauker, F. & Köberle, C. (2003), 'Arctic warming: Evolution and spreading of the 1990s warm event in the nordic seas and the arctic ocean', *Journal of Geophysical Research: Oceans* **108**(C2).
URL: https://agupubs.onlinelibrary.wiley.com/doi/abs/10.1029/2001JC001265

Langehaug, H. & Falck, E. (2012), 'Changes in the properties and distribution of the intermediate and deep waters in the fram strait', *Progress in Oceanography* **96**(1), 57–76.
URL: https://doi.org/10.1016/j.pocean.2011.10.002

Lique, C. & Steele, M. (2012), 'Where can we find a seasonal cycle of the Atlantic water temperature within the Arctic Basin?', *Journal of Geophysical Research: Oceans* **117**(3).

Mackenzie, K. V. (1981), 'Nine-term equation for sound speed in the oceans', *The Journal of the Acoustical Society of America* **70**(3), 807–812.
URL: https://doi.org/10.1121/1.386920

Meyer, A., Sundfjord, A., Fer, I., Provost, C., Villacieros Robineau, N., Koenig, Z., Onarheim, I. H., Smedsrud, L. H., Duarte, P., Dodd, P. A., Graham, R. M., Schmidtko, S. & Kauko, H. M. (2017), 'Winter to summer oceanographic observations in the Arctic Ocean north of Svalbard', *Journal of Geophysical Research: Oceans* **122**(8), 6218–6237.

Morison, J., Steele, M. & Andersen, R. (1998), 'Hydrography of the upper arctic ocean measured from the nuclear submarine u.s.s. pargo', *Deep Sea Research Part I: Oceanographic Research Papers* **45**(1), 15–38.
URL: https://www.sciencedirect.com/science/article/pii/S0967063797000253

Munk, W., Worcester, P. & Wunsch, C. (1995), *Ocean Acoustic Tomography*, Cambridge Monographs on Mechanics, Cambridge University Press.
URL: https://doi.org/10.1017/CBO9780511666926

Nilsen, F., Ersdal, E. A. & Skogseth, R. (2021), 'Wind-driven variability in the spitsbergen polar current and the svalbard branch across the yermak plateau', *Journal of Geophysical Research: Oceans* **126**(9), e2020JC016734. e2020JC016734 2020JC016734.
URL: https://agupubs.onlinelibrary.wiley.com/doi/abs/10.1029/2020JC016734

Peralta-Ferriz, C. & Woodgate, R. A. (2015), 'Seasonal and interannual variability of pan-arctic surface mixed layer properties from 1979 to 2012 from hydrographic data,

and the dominance of stratification for multiyear mixed layer depth shoaling', *Progress in Oceanography* **134**, 19–53.
URL: https://www.sciencedirect.com/science/article/pii/S0079661114002158

Perovich, D., Smith, M., Light, B. & Webster, M. (2021), 'Meltwater sources and sinks for multiyear arctic sea ice in summer', *The Cryosphere* **15**(9), 4517–4525.
URL: https://tc.copernicus.org/articles/15/4517/2021/

Piechura, J. & Walczowski, W. (2009), 'Warming of the west spitsbergen current and sea ice north of svalbard', *Oceanologia* **51**.
URL: https://www.researchgate.net/publication/26626835_Warming_of_the_West_Spitsbergen_Current_and_sea_ice_north_of_Svalbard

Polyakov, I. V., Alekseev, G. V., Timokhov, L. A., Bhatt, U. S., Colony, R. L., Simmons, H. L., Walsh, D., Walsh, J. E. & Zakharov, V. F. (2004), 'Variability of the intermediate Atlantic water of the Arctic Ocean over the last 100 years', *Journal of Climate* **17**(23), 4485–4497.
URL: https://doi.org/10.1175/JCLI-3224.1

Polyakov, I. V., Alkire, M. B., Bluhm, B. A., Brown, K. A., Carmack, E. C., Chierici, M., Danielson, S. L., Ellingsen, I., Ershova, E. A., Gårdfeldt, K., Ingvaldsen, R. B., Pnyushkov, A. V., Slagstad, D. & Wassmann, P. (2020), 'Borealization of the Arctic Ocean in Response to Anomalous Advection From Sub-Arctic Seas', *Frontiers in Marine Science* **7**(July).
URL: https://doi.org/10.3389/fmars.2020.00491

Polyakov, I. V., Beszczynska, A., Carmack, E. C., Dmitrenko, I. A., Fahrbach, E., Frolov, I. E., Gerdes, R., Hansen, E., Holfort, J., Ivanov, V. V., Johnson, M. A., Karcher, M., Kauker, F., Morison, J., Orvik, K. A., Schauer, U., Simmons, H. L., Skagseth, , Sokolov, V. T., Steele, M., Timokhov, L. A., Walsh, D. & Walsh, J. E. (2005), 'One more step toward a warmer Arctic', *Geophysical Research Letters* **32**(17), 1–4.
URL: https://doi.org/10.1029/2005GL023740

Polyakov, I. V., Bhatt, U. S., Walsh, J. E., Abrahamsen, E. P., Pnyushkov, A. V. & Wassmann, P. F. (2013), 'Recent oceanic changes in the Arctic in the context of long-term observations', *Ecological Applications* **23**(8), 1745–1764.
URL: https://doi.org/10.1890/11-0902.1

Polyakov, I. V., Pnyushkov, A. V., Alkire, M. B., Ashik, I. M., Baumann, T. M., Carmack, E. C., Goszczko, I., Guthrie, J., Ivanov, V. V., Kanzow, T., Krishfield, R., Kwok, R., Sundfjord, A., Morison, J., Rember, R. & Yulin, A. (2017), 'Greater role for atlantic inflows on sea-ice loss in the eurasian basin of the arctic ocean', *Science* **356**(6335), 285–291.
URL: https://www.science.org/doi/abs/10.1126/science.aai8204

Polyakov, I. V., Pnyushkov, A. V. & Carmack, E. C. (2018), 'Stability of the arctic halocline: a new indicator of arctic climate change', *Environmental Research Letters* **13**, 125008.
URL: https://iopscience.iop.org/article/10.1088/1748-9326/aaec1e

Polyakov, I. V., Pnyushkov, A. V. & Timokhov, L. A. (2012), 'Warming of the intermediate

atlantic water of the arctic ocean in the 2000s', *Journal of Climate* **25**(23), 8362 – 8370.
URL: https://journals.ametsoc.org/view/journals/clim/25/23/jcli-d-12-00266.1.xml

Polyakov, I. V., Timokhov, L. A., Alexeev, V. A., Bacon, S., Dmitrenko, I. A., Fortier, L., Frolov, I. E., Gascard, J.-C., Hansen, E., Ivanov, V. V., Laxon, S., Mauritzen, C., Perovich, D., Shimada, K., Simmons, H. L., Sokolov, V. T., Steele, M. & Toole, J. (2010), 'Arctic ocean warming contributes to reduced polar ice cap', *Journal of Physical Oceanography* **40**(12), 2743 – 2756.
URL: https://journals.ametsoc.org/view/journals/phoc/40/12/2010jpo4339.1.xml

Rudels, B. (2019), Arctic ocean circulation, *in* J. K. Cochran, H. J. Bokuniewicz & P. L. Yager, eds, 'Encyclopedia of Ocean Sciences (Third Edition)', third edition edn, Academic Press, Oxford, pp. 262–277.
URL: https://www.sciencedirect.com/science/article/pii/B9780124095489112096

Rudels, B., Anderson, L. G. & Jones, E. P. (1996), 'Formation and evolution of the surface mixed layer and halocline of the Arctic Ocean', *Journal of Geophysical Research C: Oceans* **101**(C4), 8807–8821.
URL: http://dx.doi.org/10.1029/96JC00143,

Rudels, B. & Carmack, E. (2022), 'Arctic ocean water mass structure and circulation', *Oceanography* .
URL: https://doi.org/10.5670/oceanog.2022.116

Rudels, B., Jones, E. P., Schauer, U. & Eriksson, P. (2004), 'Atlantic sources of the arctic ocean surface and halocline waters', *Polar Research* **23(2)**, 181–208.
URL: https://doi.org/10.3402/polar.v23i2.6278

Rudels, B., Korhonen, M., Schauer, U., Pisarev, S., Rabe, B. & Wisotzki, A. (2015), 'Circulation and transformation of atlantic water in the eurasian basin and the contribution of the fram strait inflow branch to the arctic ocean heat budget', *Progress in Oceanography* **132**, 128–152.
URL: https://www.sciencedirect.com/science/article/pii/S0079661114000494

Rudels, B., Kuzmina, N., Schauer, U., Stipa, T. & Zhurbas, V. (2009), 'Double-diffusive convection and interleaving in the arctic ocean - distribution and importance', *Geophysica* **45**.
URL: https://www.researchgate.net/publication/242594607

Rudels, B., Schauer, U., Björk, G., Korhonen, M., Pisarev, S., Rabe, B. & Wisotzki, A. (2013), 'Observations of water masses and circulation with focus on the eurasian basin of the arctic ocean from the 1990s to the late 2000s', *Ocean Science* **9**(1), 147–169.
URL: https://os.copernicus.org/articles/9/147/2013/

Screen, J. A., Deser, C. & Simmonds, I. (2012), 'Local and remote controls on observed arctic warming', *Geophysical Research Letters* **39**(10).
URL: https://agupubs.onlinelibrary.wiley.com/doi/abs/10.1029/2012GL051598

Shu, Q., Wang, Q., Song, Z. & Qiao, F.-L. (2021), 'The poleward enhanced arctic ocean cooling machine in a warming climate', *Nature Communications* **12**.
URL: https://doi.org/10.1038/s41467-021-23321-7

Skagseth, Ø. (2008), 'Recirculation of atlantic water in the western barents sea', *Geophysical Research Letters* **35**(11).
URL: https://agupubs.onlinelibrary.wiley.com/doi/abs/10.1029/2008GL033785

Smedsrud, L. H., Esau, I., Ingvaldsen, R. B., Eldevik, T., Haugan, P. M., Li, C., Lien, V. S., Olsen, A., Omar, A. M., Otterå, O. H., Risebrobakken, B., Sandø, A. B., Semenov, V. A. & Sorokina, S. A. (2013), 'The role of the barents sea in the arctic climate system', *Reviews of Geophysics* **51**(3), 415–449.
URL: https://agupubs.onlinelibrary.wiley.com/doi/abs/10.1002/rog.20017

Smedsrud, L. H., Ingvaldsen, R., Nilsen, J. E. Ø. & Skagseth, Ø. (2010), 'Heat in the barents sea: transport, storage, and surface fluxes', *Ocean Science* **6**(1), 219–234.
URL: https://os.copernicus.org/articles/6/219/2010/

Steele, M. & Boyd, T. (1998), 'Retreat of the cold halocline layer in the arctic ocean', *Journal of Geophysical Research: Oceans* **103**(C5), 10419–10435.
URL: https://agupubs.onlinelibrary.wiley.com/doi/abs/10.1029/98JC00580

Stroeve, J. & Notz, D. (2018), 'Changing state of arctic sea ice across all seasons', *Environmental Research Letters* **13**.
URL: https://iopscience.iop.org/article/10.1088/1748-9326/aade56

Stroeve, J., Serreze, M., Drobot, S., Gearheard, S., Holland, M., Maslanik, J., Meier, W. & Scambos, T. (2008), 'Arctic sea ice extent plummets in 2007', *Eos, Transactions American Geophysical Union* **89**(2), 13–14.
URL: https://agupubs.onlinelibrary.wiley.com/doi/abs/10.1029/2008EO020001

Talley, L. (2011), *Descriptive Physical Oceanography: An Introduction*, Elsevier Science.
URL: https://books.google.no/books?id=Chb14jomm08C

Timmermans, M.-L. & Marshall, J. (2020), 'Understanding arctic ocean circulation: A review of ocean dynamics in a changing climate', *Journal of Geophysical Research: Oceans* **125**(4), e2018JC014378. e2018JC014378 10.1029/2018JC014378.
URL: https://agupubs.onlinelibrary.wiley.com/doi/abs/10.1029/2018JC014378

Uotila, P., Goosse, H., Haines, K., Chevallier, M., Barthélemy, A., Bricaud, C., Carton, J., Fučkar, N., Garric, G., Iovino, D., Kauker, F., Korhonen, M., Lien, V. S., Marnela, M., Massonnet, F., Mignac, D., Peterson, K. A., Sadikni, R., Shi, L., Tietsche, S., Toyoda, T., Xie, J. & Zhang, Z. (2019), 'An assessment of ten ocean reanalyses in the polar regions', **52**(3-4), 1613–1650.
URL: *https://link.springer.com/article/10.1007/s00382-018-4242-z*

Wang, Q., Wekerle, C., Danilov, S., Wang, X. & Jung, T. (2018), 'A 4.5 km resolution arctic ocean simulation with the global multi-resolution model fesom 1.4', *Geoscientific Model Development* **11**, 1229–1255.
URL: *https://gmd.copernicus.org/articles/11/1229/2018/*

Wang, Q., Wekerle, C., Wang, X., Danilov, S., Koldunov, N., Sein, D., Sidorenko, D., von Appen, W.-J. & Jung, T. (2020), 'Intensification of the atlantic water supply to the arctic ocean through fram strait induced by arctic sea ice decline', *Geophysical Research Letters* **47**(3), e2019GL086682. e2019GL086682 10.1029/2019GL086682.
URL: *https://agupubs.onlinelibrary.wiley.com/doi/abs/10.1029/2019GL086682*

Wang, X., Liu, Y., Key, J. R. & Dworak, R. (2022), 'A new perspective on four decades of changes in arctic sea ice from satellite observations', *Remote Sensing* **14**(8).
URL: *https://www.mdpi.com/2072-4292/14/8/1846*

Woodgate, R. A. & Peralta-Ferriz, C. (2021), 'Warming and Freshening of the Pacific Inflow to the Arctic From 1990-2019 Implying Dramatic Shoaling in Pacific Winter Water Ventilation of the Arctic Water Column', *Geophysical Research Letters* **48**(9), 1–11.
URL: *https://doi.org/10.1029/2021GL092528*

Worcester, P., Dzieciuch, M. A. & Sagen, H. (2020), 'Ocean Acoustics in the Rapidly Changing Arctic', *Acoustics Today Journal of the Acoustical Society of America 2020* **16**, 55–64.
URL: *https://acousticstoday.org/wp-content/uploads/2020/02/Ocean-Acoustics-in-the-Rapidly-Changing-Arctic-Peter-F.-Worcester.pdf*

Zhang, J., Lindsay, R., Steele, M. & Schweiger, A. (2008), 'What drove the dramatic retreat of arctic sea ice during summer 2007?', *Geophysical Research Letters* **35**(11).
URL: *https://agupubs.onlinelibrary.wiley.com/doi/abs/10.1029/2008GL034005*